Žan Gojčič, BSc

Synchronization routine for real-time synchronization of modern total stations

MASTER'S THESIS

to achieve the university degree of

Diplom-Ingenieur

Master's degree programme: Geomatics Science

submitted to

Graz University of Technology

Supervisor

Univ.-Prof. Dipl.-Ing. Dr.techn. Werner Lienhart

Institute of Engineering Geodesy and Measurement Systems

Graz, October 2016

AFFIDAVIT

I declare that I have authored this thesis independently, that I have not used other than the declared sources/resources, and that I have explicitly indicated all material which has been quoted either literally or by content from the sources used. The text document uploaded to TUGRAZonline is identical to the present master‘s thesis.

Date

Signature

Acknowledgment

I would like to take this chance to express my gratitude to all the people who supported me during the writing process.

First and foremost, I would like to thank my parents Danica and Dusan and my sister Tina for their continuous support during my studies, both in mental and financial aspect. They have always encouraged me to follow my own path and for that I am eternally grateful to them.

Special thanks goes to my girlfriend Barbara for her personal support and great patience in stressful times. Although occupied with her own thesis, she always found the time and the right words to motivate me.

I would also like to express my sincere gratitude towards my supervisor Univ.-Prof. Dr.techn. Werner Lienhart, whose expertise, understanding, generous guidance and optimism in difficult times made it possible for me to complete this thesis. It was a great honor to work under his supervision.

Furthermore I would like to thank the entire IGMS team, especially Ing. Rudolf Lummerstorfer, Dipl.-Ing. Stefan Lackner and Dipl.-Ing. Matthias Ehrhart.

Last but not least, I would like to thank my dear colleagues Christina and Slaven for their professional insights, help with the experiments and countless coffees in our office. In the past couple of months, we have really become a great team.

Thank You!!

Abstract

Kinematic measurement using modern total stations, has established itself in many fields of engineering geodesy. As a consequence, the time synchronization of modern total stations has become of great importance. In this Master's Thesis, a synchronization routine for real-time synchronization of modern total stations is proposed. The proposed synchronization routine is based on a cross-correlation based time delay estimation in combination with the calibration function, to compensate for the temperature effect on the internal time of the total station. The calibration function is obtained during the calibration procedure for temperature calibration of the total station's internal time, also proposed in this thesis. As part of the routine development, an in-depth investigation of the total station's internal time characteristics was performed. The proposed routine is independent of ambient conditions and requires no additional hardware. Using the proposed synchronization routine, total stations are synchronized within 50 ms to each other, after eight hours.

Zusammenfassung

In vielen Bereichen der Ingenieurgeodäsie werden moderne Totalstationen für kinematische Messungen eingesetzt. Die Zeitsynchronisation von Totalstationen spielt daher eine zunehmend wichtiger werdende Rolle. In dieser Arbeit wird eine Methode zur Echtzeit-Synchronisation von Totalstationen vorgestellt. Diese basiert auf der Bestimmung von Zeitverschiebungen mithilfe von Kreuzkorrelation sowie einer Kalibrierfunktion zur Kompensation von temperaturbedingten Einflüssen auf die interne Uhrzeit einer Totalstation. Im Rahmen dieser Arbeit wurde eine Kalibrierfunktion entwickelt, welche aus einem Verfahren zur Temperatur-Kalibrierung der internen Uhrzeit einer Totalstation resultiert. Im Zuge dessen wurden Eigenschaften und Verhalten der internen Uhrzeit tiefgründig untersucht. Wie gezeigt wird, ist die vorgeschlagene Methode unabhängig von äußeren Einflüssen und benötigt keine zusätzliche Hardware. Mit Anwendung des entwickelten Synchronisationsverfahrens können Totalstationen auf 50 ms nach 8 Stunden Betriebszeit zueinander synchronisiert werden.

Abbreviations

ATR Automatic Target Recognition

CCF Cross-Correlation Function

CD Carrier Detect

CPA Christian's Probabilistic Algorithm

CPU Central Processing Unit

DCE Data Circuit-terminating Equipment

DTE Data Terminal Equipment

EDM Electronic Distance Measurement

GNSS Global Navigation Satellite System

GPS Global Positioning System

GUI Graphical User Interface

IGMS Institute of Engineering Geodesy and Measurement Systems

LSA Least Squares Adjustment

MEO Medium Earth Orbit

MS Multi Station

NMEA National Marine Electronics Association

PPS Pulse Per Second

RTS Robotic Total Station

SHM Structural Health Monitoring

TCXO Temperature Compensated Crystal Oscillator

TDE Time Delay Estimation

TDOA Time Difference of Arrival

TS Total Station

USB Universal Serial Bus

UTC Universal Time Coordinated

Contents

1 Introduction

Instruments used in surveying are undergoing constant development. In 1983, AGA advertised the first motorized electronic tacheometer, named Geodimeter 140. A special version, Geodimeter 140T introduced in 1985, was the first instrument, which was able to track a moving target, and can therefore be described as the first Robotic Total Station (RTS) (Rüeger, 2006). Since the introduction of the Geodimeter 140T, the quality and performance of the RTS has grown significantly (Stempfhuber, 2009). Nowadays RTS enable precise, real-time determination of the 3D trajectories of moving targets.

In the last years, kinematic measurement has established itself in many fields of engineering geodesy, especially in monitoring and machine control/automation. As a consequence, time as a fourth dimension, has become of great importance (Stempfhuber, 2001). Modern RTS are multi-sensor systems, consisting of different subsystems, whose data is combined for the output of the 3D position. While the synchronization of the individual subsystems is not of importance in the static mode, an insufficient synchronization leads to systematic errors in kinematic mode (Stempfhuber, 2004). The relative synchronization of the subsystems, especially synchronization of the distance and angle measurements, presented a large problem in the past. Numerous publications on the topic, with proposed solutions, have been published, e.g. Stempfhuber (2001), Stempfhuber (2004), Kirschner and Stempfhuber (2008) and Stempfhuber (2009). Further development has enabled the internal synchronization of the RTS's subsystems, within 1 ms of each other (Stempfhuber and Wunderlich, 2004; Stempfhuber, 2009).

Due to the complexity, several monitoring and machine control tasks require multi-sensor system configurations. When using a combination of different sensors to determine the position of a moving target, a common time basis must be established (Stempfhuber, 2001). Usually, the time basis is accomplished using a Global Navigation Satellite System (GNSS) receiver, which can be used to relate the internal time of the individual sensors with the Global Positioning System (GPS) time. Nevertheless, not only is a GNSS receiver not always part of the measurement configuration in monitoring and/or machine control projects, but it can also not be utilized in all projects, e.g. indoor or underground projects.

The problem of synchronizing individual sensors in the measurement configuration, without the use of a GNSS receiver, has come to special attention during the "Deformation monitoring of flood prevention dams" project, carried out by the Institute of Engineering Geodesy and Measurements System (IGMS) of Graz University of Technology. In the experiment, slope failures were forced, by applying vertical load on the dam crest of the experimental dam (Lienhart et al., 2013a). A sudden failure of the dam, under load, was expected. Therefore, continuous 3D measurements, with a high sampling rate and precision were performed (Lienhart et al., 2013a). Two points on the

slope of the dam, were continuously monitored using two total stations, as depicted in Figure 1-1.

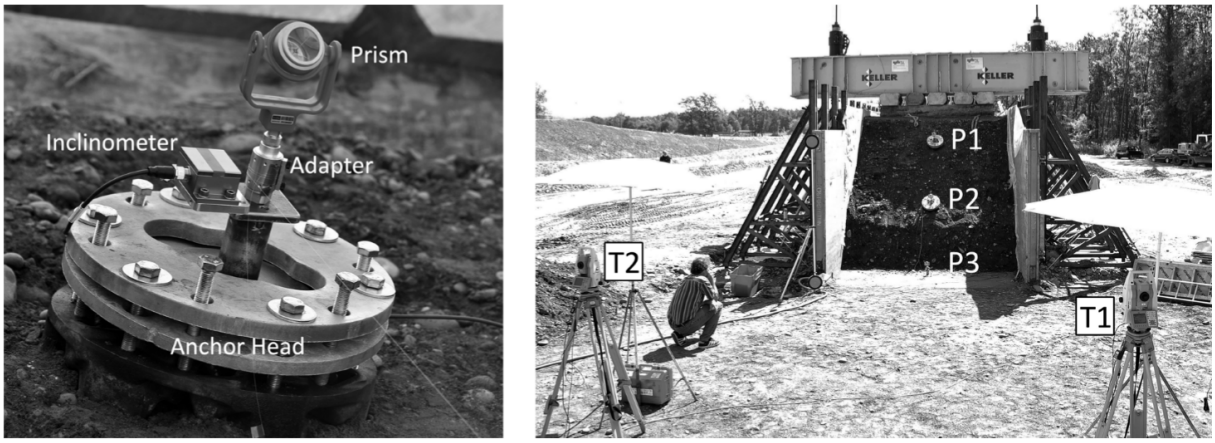

Figure 1-1: Measurement configuration of the experiment: point stabilized on the slope (left), overview with total stations (right) (Lienhart et al., 2013a, p. 3)

Apart from total stations, inclinometers and fiber optic sensors were used in the experiment. The load applied to the dam crest was gradually increased, therefore the time of the recorded deformations was essential (Lienhart et al., 2013a). As a GNSS receiver was not a part of the measurement setup, the synchronization of the sensors was done based on the time stamps of the measurements. Due to its shortcomings (see Section 2.1) this method proved not to be an efficient way of synchronizing the sensors. The presented project served as the motivation for this thesis and the goals of the thesis were formed accordingly. More information about the project is available in Lienhart (2013), Lienhart et al. (2013a), Lienhart et al. (2013b) and Lienhart (2015).

1.1 Goals of the thesis

Goals of this thesis were formed based on the findings from the above-described project. The main goal was the development of a real-time synchronization routine for time synchronization of two total stations. The developed routine should be independent from the ambient conditions, and should not require any additional hardware (sensors). The aspired accuracy of the synchronization was determined based on the usual measurement duration of a one-day project (eight hours) and the maximal sampling rate of modern RTS (app. 20 Hz). Therefore the proposed routine should enable the relative synchronization of the total stations within one sampling interval (app. 50 ms) after eight hours, which corresponds the synchronization error of approximately 1.75 ppm. In order to develop the routine, a detailed investigation of the kinematic behaviour of total stations had to be carried out (see Section 3).

2 State of the art in the multi-sensor time synchronization

"Synchronization" is a word often used in the scientific and engineering vocabulary. It originates from Greek language and in direct translation means "sharing the common time" or "occurring in the same space" (Pikovsky et al., 2001, p. xvii). According to Pikovsky et al. (2001, p. 8) synchronization can be understood as an "adjustment of rhythms of oscillating objects due to their weak interaction". In distributed systems, the term "external synchronization" means maintaining the processor clock within some given deviation to the external reference time. On the other hand, the term "internal synchronization" means maintaining the processor clocks within some given deviation relative to each other (Cristian, 1989). The three commonly used methods for internal and/or external time synchronization of spatially separated sensors are:

1. Time synchronization using time stamps of the events
2. Time synchronization using a GNSS receiver and PPS events
3. Time delay estimation using cross-correlation

2.1 Time synchronization based on time stamps of the events

According to ISA (2003, p. 186), an event is defined as "an instantaneous occurrence that is significant for scheduling the execution of an algorithm". Please note that in the course of this thesis, the term "event" denotes the messages used for communication between the master and the nodes. In the past many protocols for traditional network time synchronization, synchronization of physical clocks in a network using time stamps, have been developed. Most of them are based on a simple exchange of time stamps between nodes (sensors) and one or more time servers (computer, to which the sensors are connected) (Elson, 2003, pp. 82-88). A typical network configuration is presented in Figure 2-1.

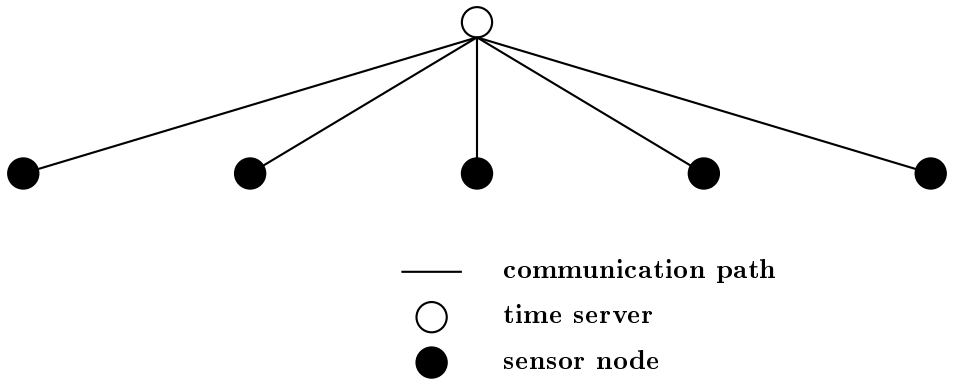

Figure 2-1: Network configuration in the traditional network time synchronization

In the traditional network time synchronization it is assumed that each entity of the network has access to the hardware clock of its Central Processing Unit (CPU), and that these clocks have a much higher time resolution than the time delays which need to be measured (Cristian, 1989). Cristian (1989) proposed the first probabilistic clock synchronization algorithm, Cristian's Probabilistic Algorithm (CPA). Note that the word "probabilistic" denotes the uncertainty in the guarantee (a priori precision of a remote clock reading) by the algorithm. CPA is a master-slave algorithm, meaning that one node of the configuration is the designated master (time server) and other nodes are designated slaves (sensors). The time offset between the master (M) and the individual slaves (S) can, according to Arvind (1994), be estimated as

$$\Delta T^{S}_{M,est} = T_M(i) - T_S(i) - \bar{d}_s\,, \tag{2-1}$$

where $T_S(i)$ denotes the time-stamp recorded by S on the transmitted time of the message i, $T_M(i)$ denotes the time-stamp recorded by M upon receiving the message i and $\bar{d}_s$ denotes the estimate of the expected value of the message delay. The problem in estimating the time offset between M and S is the arbitrary, random message delay $d_s(i)$ (also called latency) that is, according to Kopetz and Ochsenreiter (1987), dependent on:

Send Time - variable time spent at the source to construct the message, after the clock has been recorded

Access Time - variable delay due to waiting for access on the transmit channel

Propagation Time - variable propagation delay of the message, dependent on distance and channel

Receive Time - variable time to receive the message and record the time of arrival.

In the past, various methods of estimating the time delay d_s were proposed. Since an in-depth explanation of the estimation problem is not a goal of this thesis, please refer to Kopetz and Ochsenreiter (1987), Cristian (1989) and Arvind (1994) for more information.

2.1.1 Adaptation on the defined multi-sensor system configuration

Adaptation of the synchronization method using time stamps of the events, on the sensor system configuration defined in Section 1.1 is presented in Figure 2-2.

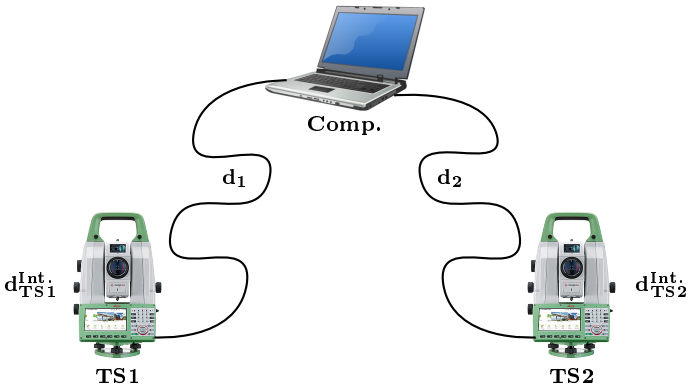

Figure 2-2: Adaptation of the time stamp synchronization method on the defined sensor system configuration (schematic representation)

Two total stations (TSj, $j = 1, 2$) represent the slaves, and the laptop (Comp.) represents the master in the network configuration. The communication between the individual total stations and the laptop is realized using GeoCom commands (see Section 3.3). The measurement performed by the total station is sent to the laptop together with the time stamp of the measurement $T_{TSj}^{Meas.}(i)$. Upon receiving the message, the laptop records the time stamp of the received event ($T_{Comp.}^{TSj}(i)$). Due to the internal synchronization of the measurements (see Section 3.4) in the total stations, an additional parameter of the delay has to be passed to Equation 2-1. The time offset between the laptop and the total station, can therefore be estimated as

$$\Delta T_{Comp.,est}^{TSj}(i) = T_{Comp.}^{TSj}(i) - T_{TSj}^{Meas.}(i) - d_{TSj}(i) - d_{TSj}^{Int.}(i)\,, \tag{2-2}$$

where $d_{TSj}^{Int.}(i)$ denotes the arbitrary delay due to the internal synchronization of the measurements in the total station (see Section 3.4). Consequently the time offset between the total stations can be estimated as

$$\Delta T_{TS1,est}^{TS2}(i) = \Delta T_{M,est}^{TS1}(i) - \Delta T_{M,est}^{TS2}(i)\,. \tag{2-3}$$

2.2 Time synchronization using a GNSS receiver and PPS events

2.2.1 Global Positioning System

Ever since the introduction, GPS, has revolutionized clock comparison and offered a new method for precise time synchronization (Mumford, 2003). Even though GPS is primarily a navigation system, it grants a precise atomic clock service to anyone in possession of a GPS receiver and a clear view of the sky (Mumford, 2003). GPS consists of a constellation of at least 24 satellites distributed into six Medium Earth Orbit (MEO) planes at about 22.200 km altitude. This geometry ensures that at least six satellites are visible from every point on the Earth 24 hours per day (El-Rabbany, 2002, p. 2). All GPS satellites are equipped with cesium and/or rubidium atomic clocks (Table 2-1).

Table 2-1: GPS constellation status for 30.05.2016 (R - rubidium, C - cesium) (U.S.C.G., 2016)

PRN	1	2	3	5	6	7	8	9	10	11	12	13	14	15	16	17
Clock	R	R	R	R	R	R	C	R	R	R	R	R	R	R	R	R
PRN	18	19	20	21	22	23	24	25	26	27	28	29	30	31	32	
Clock	R	R	R	R	R	R	R	R	C	R	R	R	R	R	R	

GPS Time is a continuous time scale (not corrected by leap seconds), measured from the start epoch at 6th of January 1980 at midnight Universal Time Coordinated (UTC). It is defined by the Master control station of the GPS control segment (network of global monitor stations) and is referenced to UTC as maintained by the U.S. Naval Observatory (USNO) (ICD, 2012, p. 39). GPS Time is synchronized with UTC at a one microsecond level (modulo one second), not considering leap seconds (Lewandowski and Thomas, 1991; ICD, 2012, p. 39). The stability of the GPS atomic clocks is thoroughly monitored by the GPS control segment and the clock parameters of aging, drift and bias are uploaded to individual satellites every day (ICD, 2012, p. 51). These parameters are then broadcasted by the satellites, along with other data, as a part of a navigation message.

Table 2-2: Clock correction parameters contained in the GPS navigation message (ICD, 2012, p. 160)

	Parameter	**No. of Bits**	**Unit**
t_{oc}	Clock Data Reference Time of Week	11	s
a_{f2-n}	SV Clock Drift Rate Correction Coefficient	10	s/s^2
a_{f1-n}	SV Clock Drift Correction Coefficient	20	s/s
a_{f0-n}	SV Clock Bias Correction Coefficient	26	s

According to Hofmann-Wellenhof et al. (1997, pp. 89-130) and Witchayangkoon (2000, pp. 14-15), the pseudorange observation equation is defined as

$$P_R^S = \rho_R^S + c(\delta t^S - \delta t_R) + \Delta_{ion} + \Delta_{trop} + \Delta_{rel} + \Delta_R + \Delta_{mp} + \Delta_S + \epsilon\,. \tag{2-4}$$

By rearranging Equation 2-4, the offset of the receiver clock to the GPS system time (δt_R) is defined as

$$\delta t_R = \delta t^S + \frac{\rho_R^S - P_R^S + \Delta_{ion} + \Delta_{trop} + \Delta_{rel} + \Delta_{mp} + \Delta_R + \Delta_S + \epsilon}{c}\,, \tag{2-5}$$

where the measured pseudorange P_R^S is determined by measuring the difference of two identical codes, one generated by the receiver R and the other propagated by the satellite S. ρ_R^S denotes the actual geometrical distance between the satellite and the receiver, calculated from the coordinates. Correction parameters Δ_{ion}, Δ_{trop}, Δ_{rel}, Δ_{mp}, Δ_R and Δ_S denote propagation delay due to the ionosphere, propagation delay due to the troposphere, correction due to the relativistic effect, correction due to the multipath, a receiver hardware delay, and a satellite hardware delay respectively and ϵ denotes the measurement noise. Referring to Hofmann-Wellenhof et al. (1997, p. 181) and (ICD, 2012, p. 178) the offset of the satellite clock to the GPS System time δt^S can be estimated using the satellite clock correction parameter (see Table 2-2) and the relativistic term $\Delta \mathrm{t_r}$ as

$$\delta t^S = \mathrm{a_{f0}} + \mathrm{a_{f1}}(\mathrm{t} - \mathrm{t_{oc}}) + \mathrm{a_{f2}}(\mathrm{t} - \mathrm{t_{oc}})^2 + \Delta \mathrm{t_r}\,. \tag{2-6}$$

The GPS navigation message also provides the parameters needed for correlating the GPS time with UTC(USNO). The high accuracy of broadcasted parameters enables the relation of the GPS time to UTC with an accuracy of 90 nanoseconds (1σ) (Lewandowski and Thomas, 1991; ICD, 2012). For an in-depth explanation on how to relate GPS time with UTC time please refer to (ICD, 2012). Furthermore, refer to (ICD, 2012) for additional information about the satellite clock correction parameter.

2.2.2 PPS event based synchronization

Utilization of the accurate GPS time or UTC for synchronization purposes is enabled by the Pulse Per Second (PPS) time pulses, transmitted by the dedicated, timing GPS receivers and some high-end positioning GPS receivers. Most timing receivers enable special "timing mode" where the coordinates of the antenna are fixed in solution, leaving only the receiver clock offset to be estimated. While in timing mode, the receiver can provide an accurate time solution, by tracking only one satellite (u-blox, 2014). On the other hand, if the antenna coordinates are not fixed in solution, at least four satellites are needed, for an accurate time offset estimation. Based on its synchronization with the GPS and/or UTC time, the receiver sends a digital time pulse to the dedicated pin. By default, this pulse is sent each second, hence the name PPS, but the modern timing receivers also enable

higher frequencies of up to 10 MHz (u-blox, 2014). The timing receiver u-blox LEA-6T used for the sensor investigation (see Section 3) provides two time pulses (Figure 2-3) with configurable frequency (1/60 Hz to 1 kHz), pulse length, pulse polarity (rising or falling edge) and reference time (GPS, UTC or local time) (u-blox, 2014).

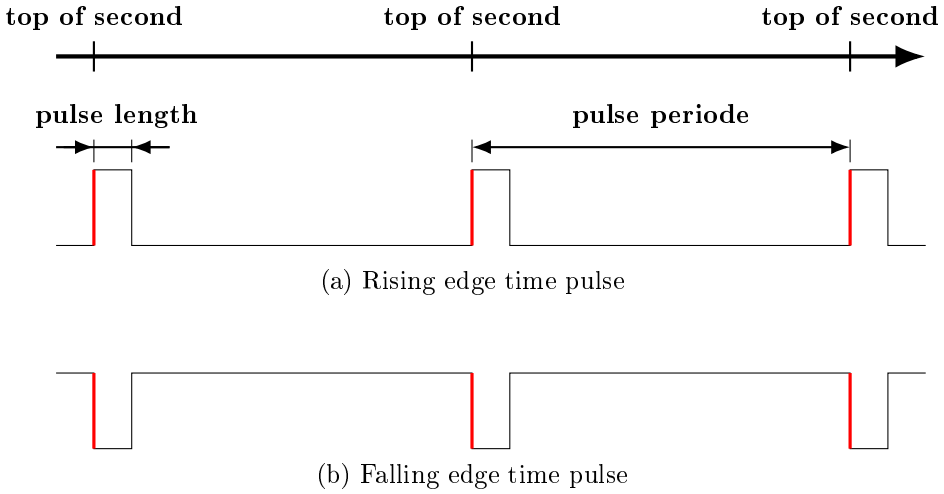

(a) Rising edge time pulse

(b) Falling edge time pulse

Figure 2-3: Time pulse of the u-blox LEA-6T timing GPS receiver (after u-blox, 2014)

Even though modern timing receivers enable higher frequency time pulses, a low time pulse frequency e.g. 1 Hz is best for exact timing measurements according to u-blox (2011). The accuracy of time pulses is measured as a difference to a reference time, usually generated by an atomic clock. Modern receivers transmit time pulses with accuracy in nanoseconds range, which makes them more than applicable for the purposes presented in Sections 1 and 1.1. In addition to the time pulses, receivers also enable National Marine Electronics Association (NMEA) standardized sentences that enable relation of individual time pulses with the UTC or GPS time. As for which NMEA sentences are to be transmitted can be configured on the receiver. The GGA sentence (used in Section 3), commonly used for the GPS positioning, can also be utilized for time synchronization, since it provides the data needed for relating individual pulses to the UTC time (Figure 2-4). More information about NMEA sentences can be acquired from *www.nmea.org*.

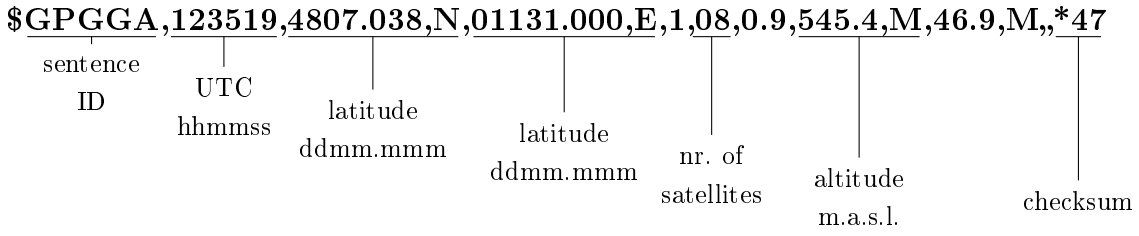

Figure 2-4: Structure of the standardized GGA NMEA sentence (NMEA, 2016)

2.2.3 Adaptation on the defined multi-sensor system configuration

Adaptation of the GPS based synchronization method on the sensor system configuration defined in Section 1.1 is presented in Figure 2-5.

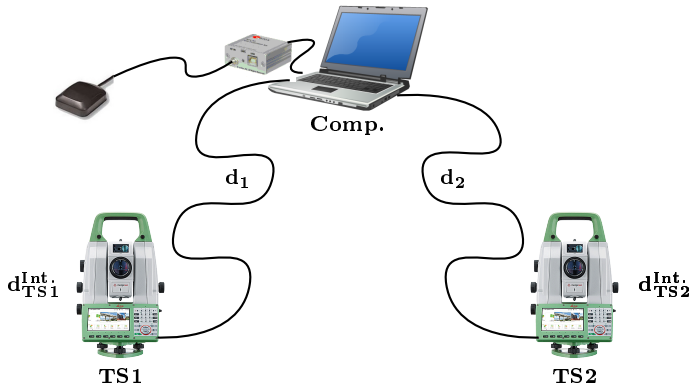

Figure 2-5: Adaptation of the GPS time based synchronization method on the defined sensor system configuration (schematic representation)

The system configuration presented in Figure 2-5 is similar to the one described in Section 2.1.1, since the used instruments do not enable a direct utilization of the PPS events. The GPS receiver is connected to the serial port of the computer, on which the registration software (see Section 3.2), responsible for the registration and the time stamping of the individual PPS events, is running. Two instruments can be synchronized using PPS events in two ways. Either the PSS events are used as a trigger, on which the GeoCOM commands are sent to the instruments, or the PPS events are used for correcting the time drift of the computer, and the rest follows the method presented in Section 2.1.1.

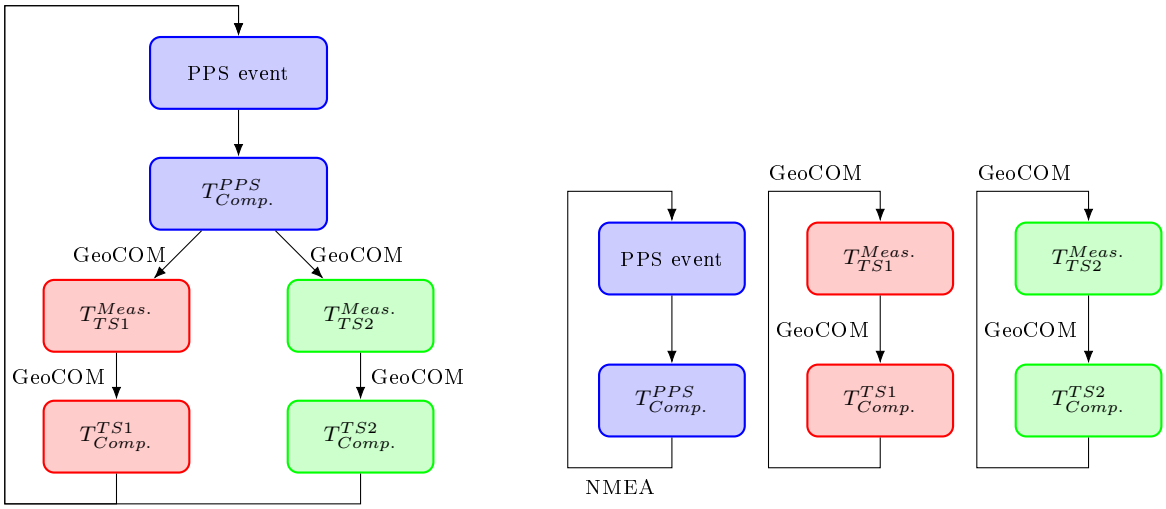

(a) First method (b) Second method

Figure 2-6: Flowchart of the GPS based time synchronization methods, adapted to the defined sensor system configuration, each color (blue, red and green) represents an individual software thread

In the first method (Figure 2-6a), the individual PPS events are used as triggers for the measurements. The computer records the CPU time stamp of the received PPS event ($T^{PPS}_{Comp.}$) and sends GeoCOM commands to the instruments. GeoCOM commands can be sent simultaneously, as a separate thread is assigned to an individual total station. The instruments preform the measurements and save their time stamps ($T^{Meas.}_{TSj}$, $j = 1, 2$). The GeoCOM messages, including time stamps of the measurements are then sent back to the computer where they are time stamped with the CPU time of the computer ($T^{TSj}_{Comp.}$). The GPS time time stamp of the instrument's measurements can be obtained as

$$T^{TSj}_{GPS}(i) = T^{PPS}_{GPS}(i) + (T^{TSj}_{Comp.}(i) - T^{PPS}_{Comp.}(i)) - d_{TSj}(i) - d^{TSj}_{Int.}(i)\,, \tag{2-7}$$

where $T^{PPS}_{GPS}(i)$ denotes the GPS time of the i-th PPS event. Consequently, the offset of the total station's internal time to the GPS time can be calculated as

$$\Delta T^{TSj}_{GPS}(i) = (T^{Meas.}_{TSj}(i) - T^{PPS}_{GPS}(i)) - (T^{TSj}_{Comp}(i) - T^{PPS}_{Comp}(i)) - d_{TSj}(i) - d^{TSj}_{Int.}(i)\,. \tag{2-8}$$

Additionally the drift rate of the computer time in relation to the GPS time ($\Delta T^{GPS}_{Comp.}$), can be determined as

$$\Delta T^{GPS}_{Comp.} = 1000\,\text{ms} - (T^{PPS}_{Comp.}(i) - T^{PPS}_{Comp.}(i-1))\,. \qquad [ms/s] \tag{2-9}$$

This method enables the absolute synchronization of two instruments, but shares the shortcomings of the time stamps based method (estimating the latency and the time delay due to the internal synchronization). Moreover, it limits the sampling rate of the measurements with the frequency of the PPS events, which is often lower as the sampling rate of the instruments. In order to use the highest possible sampling rate of the instruments, the second method (Figure 2-6b), can be utilized. In the second method, the process runs in three separate threads, registration of the PPS events in one and measurements of the individual instruments in the other two (presented with different colours in Figure 2-6b). The time stamping of the events and the calculation of the time drift and the time stamps in GPS time follow the same procedure as in the first method. The individual total station measurements are combined with the last recorded PPS event based on the CPU time stamps of the PPS events and measurements.

2.3 Time delay estimation using cross-correlation

2.3.1 Cross-correlation

Time delay estimation (TDE) presents a big challenge in all areas that deal with signal processing. Time delay can represent a time difference between a broadcast signal and the reception of its echo (radar), or the relative time difference of arrival (TDOA) between two spatially separated sensors (Benesty and Chen, 2004). The most commonly used method for TDE is the generalized correlation method proposed by Knapp and Carter (1976). Using this method, the time delay estimate is obtained as the time lag at the maximal cross-correlation coefficient between two received signals.

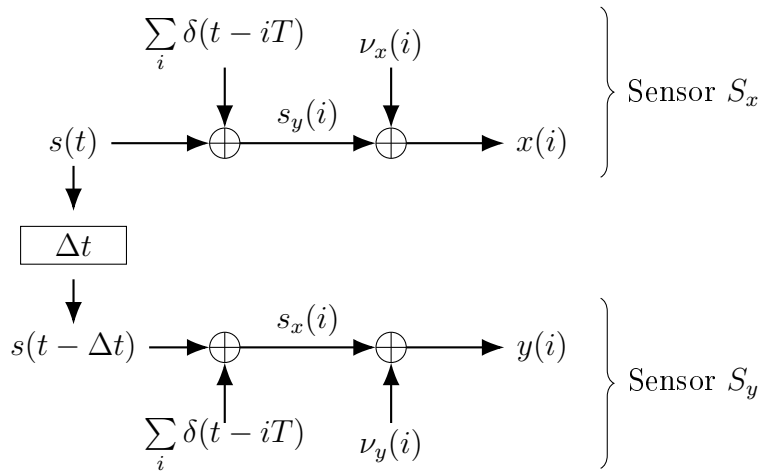

Figure 2-7: Sampling process of two spatially separated sensors (after Zhang and Wu, 2006)

Figure 2-7 depicts the sampling process of the signal $s(t)$, which is observed by two spatially separated sensors (S_x and S_y) with the relative time delay Δt. The signal is sampled by the Dirac sequence with a period T. Considering measurement noise ν, the discrete observations can be expressed as (Zhang and Wu, 2006)

$$x(i) = s_x(i) + \nu_x(i) \qquad \text{and} \qquad y(i) = s_y(i) + \nu_y(i)\,. \tag{2-10}$$

For two stochastic processes $X(t)$ and $Y(t)$ that are stationary (their statistic does not change when shifted in time), a cross-covariance function is defined as (Wei, 2006, p. 326)

$$\gamma_{X,Y}(\tau) = E[(X(t) - \mu_X)(Y(t+\tau) - \mu_Y)]\,, \tag{2-11}$$

where E denotes the expected value and $\mu_X = E(X(t))$ and $\mu_Y = E(Y(t))$.

The corresponding cross-correlation function (CCF) can be obtained upon standardization as (following equations are taken from Montgomery et al. (2008, p. 308))

$$\rho_{X,Y}(\tau) = \frac{\gamma_{X,Y}(\tau)}{\sqrt{\gamma_X(0)\gamma_Y(0)}}\,. \tag{2-12}$$

Given two discrete, evenly sampled time series $x(i)$ and $y(i)$ with $i = 0, 1, 2, ...N-1$ samples (see Figure 2-7), the cross-covariance function can be estimated as

$$\hat{\gamma}_{x,y}(\tau) = \frac{1}{N}\sum_{i=0}^{N-1-\tau}\left[(x(i)-\bar{x})(y(i+\tau)-\bar{y})\right], \tag{2-13}$$

and analogically to Equation 2-12, the CCF can be estimated as

$$r_{x,y}(\tau) = \frac{\hat{\gamma}_{x,y}(\tau)}{\sqrt{\hat{\gamma}_x(0)\hat{\gamma}_y(0)}} \qquad \text{for} \qquad \tau = 0, 1, ...N-1\,, \tag{2-14}$$

where

$$\hat{\gamma}_x(0) = \frac{1}{N}\sum_{i=0}^{N-1}(x(i)-\bar{x})^2 \qquad \text{and} \qquad \hat{\gamma}_y(0) = \frac{1}{N}\sum_{i=0}^{N-1}(y(i)-\bar{y})^2\,. \tag{2-15}$$

Determination of the continuous case TDE requires computation of the Equation 2-12 for the infinite number of values τ. In discrete case, the computation range is limited with the number of samples N, and the delay estimate is defined as an argument τ that maximizes the statistic $r_{x,y}(\tau)$ (Knapp and Carter, 1976). Equation 2-14 also indicates the limitation of the discrete case CCF. The highest resolution of the TDE that can be obtained, equals the sampling period of the signal, e.g. for a signal sampled with 20 Hz, the highest resolution equals 50 ms. Since the time delay is usually not an integer multiple of the sampling rate, a subsample resolution needs to be obtained. This can be achieved either by up-sampling the signal before the cross-correlation or by interpolating the CCF. Using two spatially separated sensors, signals are often irregularly sampled or sampled with different sampling rates. To satisfy the conditions of the discrete cross-correlation, signals have to be interpolated to the time points that ensure evenly spaced data and at the same time, the signals can be up-sampled. This increases the resolution of the cross-correlation on the one hand, but on the other hand it also increases the computational load. Therefore the interpolation of the CCF, in order to increase the resolution of the TDE is preferred, especially when dealing with large data sets.

2.3.2 Subsample interpolation of the CCF

Wiens and Bradley (2008) discuss various methods of CCF interpolation. The current standard is the parabola-based model, even though in some applications a Gaussian approximation model yields more accurate and robuster results (Zhang and Wu, 2006). The parabola-based method can also be described as a three points interpolation method, since a parabola function is fitted to three points $r_{x,y}(\tau-1)$, $r_{x,y}(\tau)$ and $r_{x,y}(\tau+1)$, where $r_{x,y}(\tau)$ denotes the maximum of CCF (see Equation 2-14). Considering the standard parabola equation $y = ax^2 + bx + c$, the parameters a, b and c can be, according to Zhang and Wu (2006), determined as

$$\begin{bmatrix} a \\ b \\ c \end{bmatrix} = \begin{bmatrix} (\tau-1)^2 & (\tau-1) & 1 \\ \tau^2 & \tau & 1 \\ (\tau+1)^2 & \tau+1 & 1 \end{bmatrix}^{-1} \begin{bmatrix} r_{x,y}(\tau-1) \\ r_{x,y}(\tau) \\ r_{x,y}(\tau+1) \end{bmatrix}. \tag{2-16}$$

Using the parabola-based method, the best TDE is denoted as the time delay at the maximum of the parabola function (Figure 2-8).

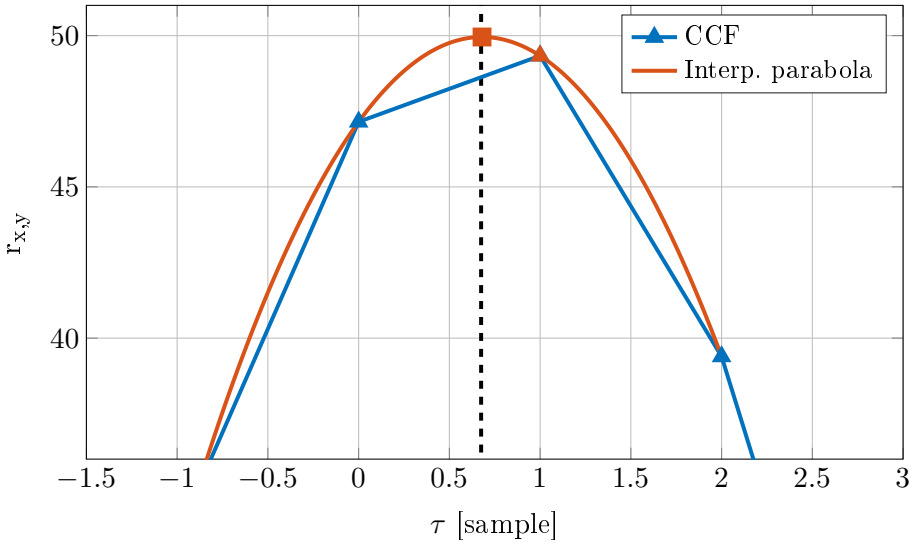

Figure 2-8: CCF of two spatially separated time series, with 0.67 sample time shift (black dashed line). The three triangles represent maximum (orange triangle at $\tau = 1$) and its immediate neighbour (blue triangles) cross-correlation coefficients used for parabola based subsample interpolation (orange square represents maximum of parabola function at $\tau = 0.67$).

2.3.3 Correlation properties of different signals

Given two infinite periodic signals with a common period N, the CCF of the signals is also periodic with the same period N. This leads to an infinite number of maxima in the CCF and consequently an infinite number of time lag estimates. In practice, the signals are of finite length. If two finite periodic signals have equal length, the CCF only has one maximum, which denotes the time lag of the signals. The CCF still oscillates at the same frequency as the signals, but its amplitude decays as the difference between the time delay and the lag value increases. On the other hand, if one of the signals is shorter than the other, a CCF can have multiple maxima, and the time lag estimation becomes ambiguous. Such signals have bad correlation properties. One example of a periodic signal, which often appears in the Structural Health Monitoring (SHM) is the sine wave (vibration of the structures). Apart from the previously described characteristics, the CCF of two time-shifted sine waves has a flat maximum peak, which hinders the peak detection. If the signals are additionally distorted by noise, this can lead to a maximum on a lag location not corresponding the true delay of the time series.

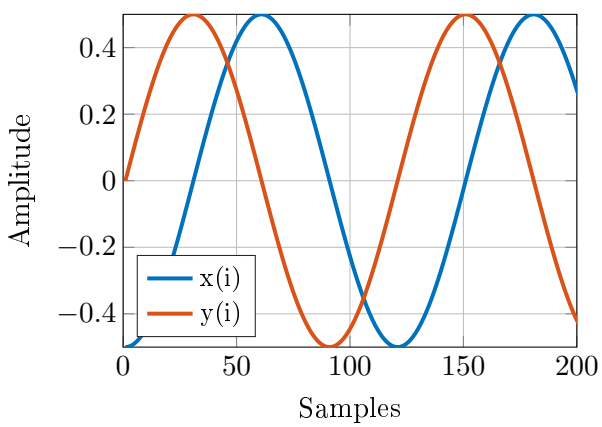

(a) Sine wave (bad correlation properties)

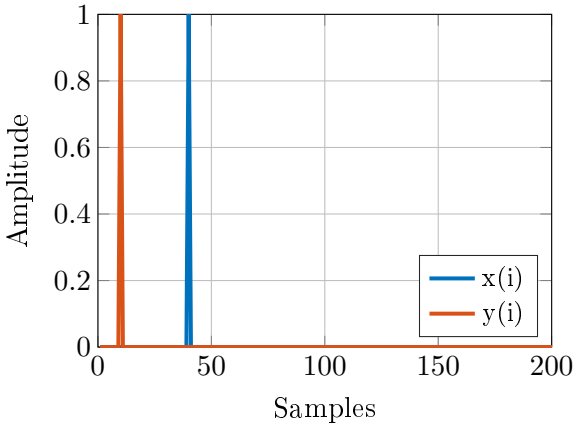

(b) Dirac impulse (good correlation properties)

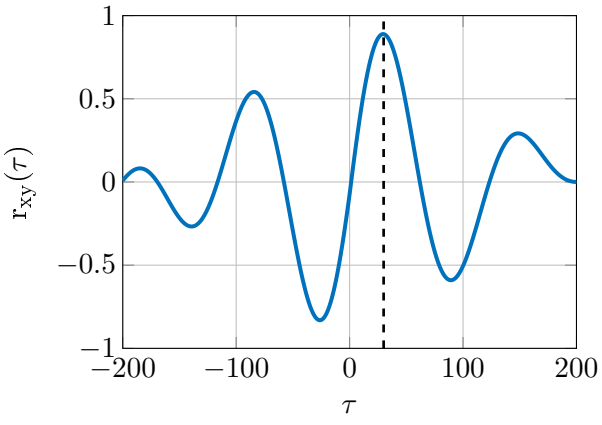

(c) CCF of time shifted sine waves

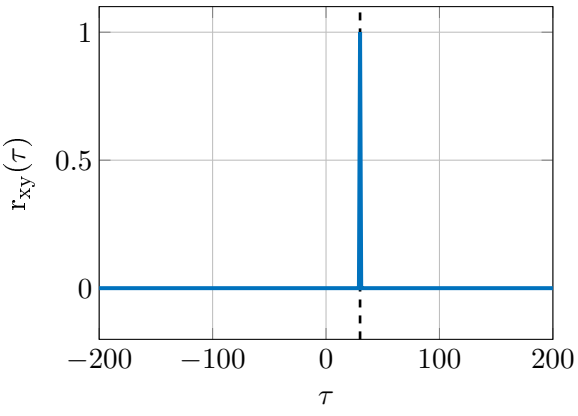

(d) CCF of time shifted Dirac impulses

Figure 2-9: CCF comparison of two signals with bad and good correlation properties. The true time delay between the individual time series (measurements of the signal) equals 30 samples. Black dashed line depicts the maximum of the CCF

Figure 2-9 depicts a comparison between a signal with good and an a signal with bad correlation properties. CCF of a signal with good correlation properties has a sharp peak at the lag that equals the delay of the time series (Figure 2-9d), whereas the CCF peak is flat by the signal with bad correlation properties (Figure 2-9c).

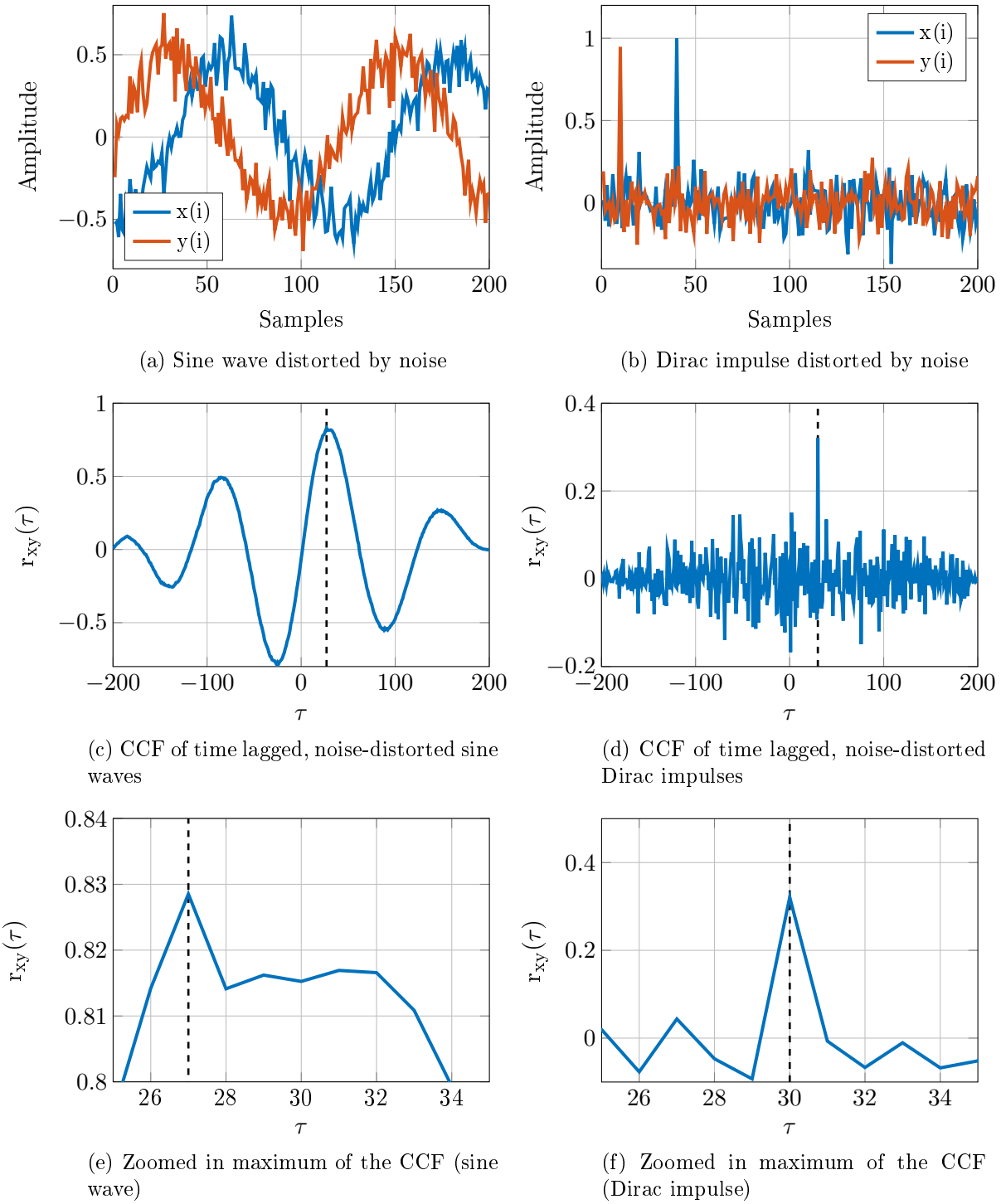

(a) Sine wave distorted by noise

(b) Dirac impulse distorted by noise

(c) CCF of time lagged, noise-distorted sine waves

(d) CCF of time lagged, noise-distorted Dirac impulses

(e) Zoomed in maximum of the CCF (sine wave)

(f) Zoomed in maximum of the CCF (Dirac impulse)

Figure 2-10: CCF comparison of two noise-distorted signals with bad and good correlation properties. The true time delay between individual time series (measurements of the signal) equals 30 samples. Black dashed line depicts the maximum of the CCF

Measured time series are always influenced by the noise, to some degree. To investigate the influence of the noise on the peak detection of the CCF, a Gaussian noise ($\mu = 0, \sigma = 10\,\%$ of the signal's amplitude) was added to the time series (Figures 2-10a and 2-10b). The results of the cross-correlation analysis of noise-distorted time series are presented in Figure 2-10. Analysing the CCF of the noise-distorted time series of a signal with good correlation properties, the maximum of the CCF is still located at the lag, corresponding the true time delay of the time series. Moreover the peak is sharp and easily detectable (Figure 2-10f). The added noise results in the oscillation of the CCF. Combined with the flat peak of the CCF of a signal with bad correlation properties, this can cause that the maximum of the CCF is no longer located at the lag, corresponding the true time delay of the time series (30 samples). This results in a false time delay estimation as presented in Figure 2-10e.

The correlation properties of a signal can be improved by generating a signal with good correlation properties in the existing signal. This procedure not only improves the correlation properties of signals with bad correlation properties, but it also enables the time delay estimation of uncorrelated time series, e.g. measurement noise when locked onto a stable prism. In surveying, usually an approximation of the Dirac impulse is used, as it can easily be simulated with an abrupt movement of the prism. Such improvement of correlation properties of a noise-corrupted sine wave, is presented in Figure 2-11.

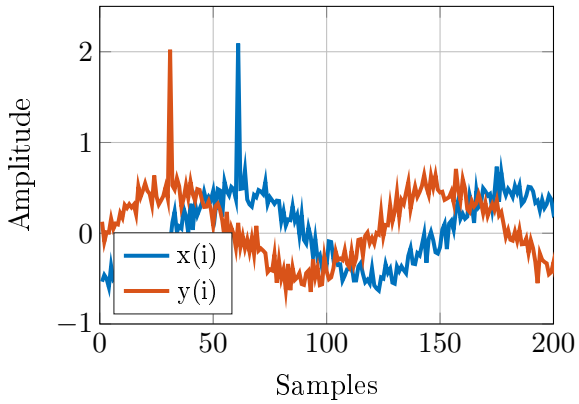

(a) Dirac impulse generated in the noise-corrupted sine wave

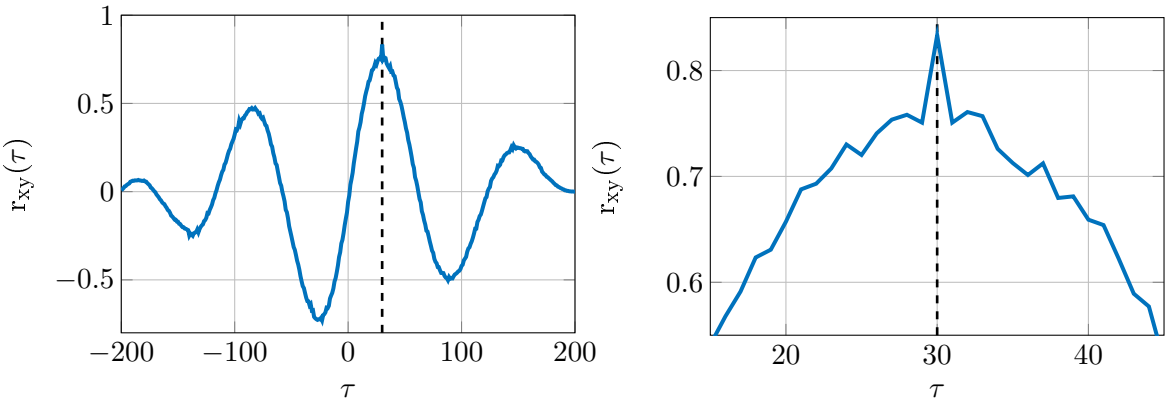

(b) CCF

(c) Zoomed in CCF

Figure 2-11: CCF of noise-distorted sine waves, with improved correlation properties, by generating the Dirac impulse in the existing signal. The true time delay between individual time series (measurements of the signal) equals 30 samples. Black dashed line depicts the maximum of the CCF

2.3.4 Effect of the sensor time drift on the cross-correlation based time synchronization

The time drift of the sensors influences the time synchronization based on the cross-correlation. Even though the sensors are synchronized (e.g. approximation of the Dirac impulse generated at the start of the measurement), they drift apart with time if their time drift magnitude and sign are not equal. This shortcoming can be partially overcome by generating two or more abrupt changes in the data (Figure 2-12). This enables the calculation of the time delay, twice (once per each peak), and a linear time drift of one sensor with respect to the other can be expressed from their difference. This yields adequate results only under the assumption that the time drift of the sensors is linear in time.

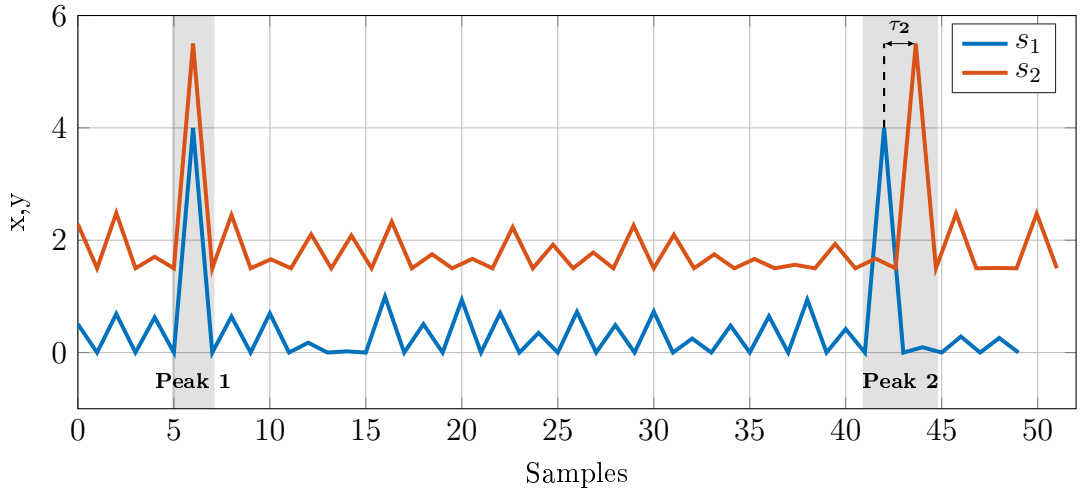

Figure 2-12: Two time series (measurements), synchronized using cross-correlation (Peak 1), drift apart due to the different time drift of the sensors (τ_2 represents TDE at Peak 2)

For further information on cross-correlation and TDE, please refer to Knapp and Carter (1976), Benesty and Chen (2004) and Montgomery et al. (2008). For further methods of CCF interpolation, refer to Zhang and Wu (2006) and Wiens and Bradley (2008).

2.3.5 Adaptation on the defined multi-sensor system configuration

Time synchronization based on the time delay estimation using cross-correlation does not require any special adaptation on the defined system. If done in post processing, the measurement data can even be saved on the individual instruments, and later analysed on the computer. Total station measurements in SHM usually have bad correlation properties, e.g. measurement noise when the prism is stable, or a sine wave form of the structure's vibrations. To improve the correlation properties of the measurements, an approximation of the Dirac impulse can be generated by abruptly moving the dedicated prism, e.g. up and down. The dedicated prism does not have to be located on the object. It should only be visible by both total stations, and must enable the movement for the peak generation in the measurements. It is advised - if possible - that when generating the movement, both instruments track the same prism as this eliminates the need of synchronizing the movement. Please note that the potential reflections from the front surface of the prism, which could cause the tracking systems to interfere, need to be considered. One of the possible measurement configurations is presented in Figure 2-13

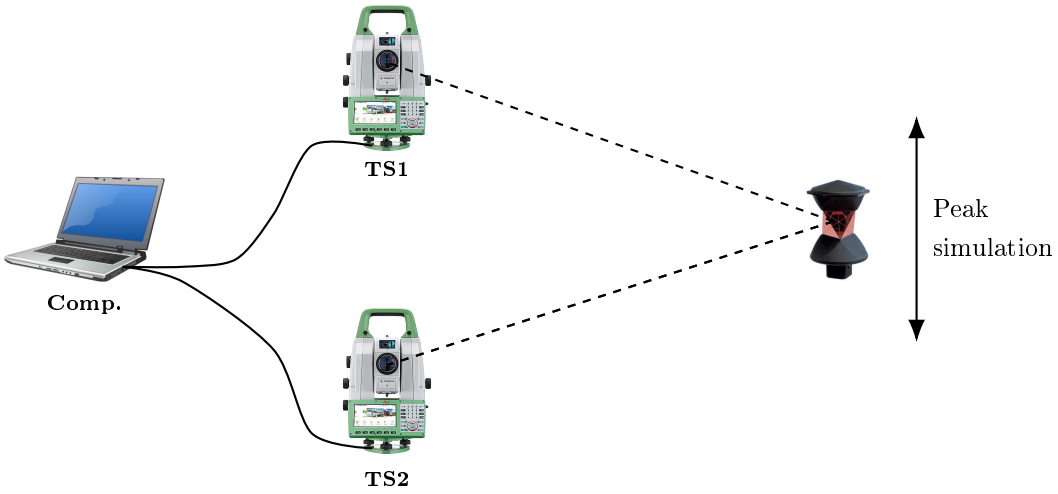

Figure 2-13: Adaptation of the cross-correlation based synchronization method on the defined sensor system configuration (schematic representation)

Figure 2-13 depicts a configuration where both instruments are connected to one laptop, which is used for remote control of the instruments. Such configuration enables the time synchronization in real-time, as the measurement data is constantly streamed to the computer. During the peak simulation, both instruments are locked onto one prism. This eliminates the need for synchronization of the movement. The time delay between the instruments is calculated using Equations 2-13 and 2-14, where the measurements, time stamped with the internal time of the instrument, represent the input data. The proposed configuration is independent of the laptop's time drift and message delay variations. A detailed explanation of the proposed measurement configuration is presented in Section 5.

2.4 Conclusion

The state of the art methods, used in multi-sensor time synchronization are very diverse. Despite that, none of the methods fulfils the requirements of the real-time synchronization routine aspired in Section 1.1. Table 2-3 shows the comparison of the currently used methods and serves as a base for determining the method that could be further developed in such a routine.

Table 2-3: Comparison of state of the art methods used in time synchronization of spatially distributed sensors

Method	Advantages	Disadvantages
Time stamps	• No additional sensors, • Applicable indoors	• Random message delay estimation, • Time drift of the time server and sensors, • Resolution and precision of the time stamps, • All sensors have to be connected to one time server
GNSS based	• Long term stability, • Relation to UTC or GPS time, • Accuracy not dependent on the duration time	• Random message delay estimation, • Not applicable indoors, • PPS event not sent if not enough satellites tracked, • Resolution and precision of the time stamps, • Additional sensor needed
Cross-correlation	• No additional sensors, • Applicable indoors, • Direct synchronization of the measurements, • Independent of the message delay	• Time drift of the sensors, • Done in post-processing, • Potentially bad correlation properties of the signal

Some of the shortcomings of the individual methods presented in Table 2-3 cannot be overcome, e.g. GNSS based synchronization requires clear view of the sky. Despite the positive aspects, such methods are not applicable for a real-time synchronization routine as aspired in Section 1.1 and can therefore not be considered further. Based on the desired performance of the system and the characteristics of the individual methods, the cross-correlation was selected as the primary method for further development. In order to satisfy the specifications of the system, three shortcomings; the instrument's internal time drift, bad correlation properties of total station measurements in SHM and post-processing have to be overcome. To develop a strategy on how to overcome these disadvantages, the experiments presented in the Section 3 were performed.

3 Total station's internal time investigation

The total station time investigation was carried out in order to determine the basis for the time synchronization routine and to evaluate the accuracy of the synchronization that can be achieved. A strategy, on how to overcome the shortcomings of the cross-correlation based synchronization (listed in the Section 2.4) can only be developed if the characteristics of the total stations that influence the time synchronization are known. The whole section is based on Leica instruments, specifically Leica TS15 (S/N: 1613987) and Leica MS60 (S/N: 882001). All the instruments used in the course of this thesis were provided by IGMS of Graz University of Technology. Statements made in the following sections are valid solely for the two total stations listed above, and cannot be generalised.

3.1 Used instrumentation

3.1.1 Total stations

In the course of this thesis, two instruments - Leica's total station TS15 I 1 R1000 (Figure 3-1a) and Leica's multi station MS60 I R2000 (Figure 3-1b) were used as two spatially separated sensors that had to be synchronized. In the following, used instruments are briefly denoted as Leica TS15 and Leica MS60.

(a) Leica TS15 and Leica GEV187 (b) Leica MS60 and Leica GEV 261

Figure 3-1: Instruments used as spatially separated sensors

During the investigation, the total stations were remote-controlled using Leica proprietary communication interface GeoCom, which enables a client-server based communication of the computer with the instrument. Total stations were connected to the computer using Leica GEV261 (Leica MS60) and Leica GEV187 (Leica TS15) cables. Table 3-1 provides basic information about both instruments.

Table 3-1: Basic specifications of Leica TS15 and Leica MS60

	Leica TS15	**Leica MS60**
Serial number	1613987	882001
Firmware	SmartWorx Viva 5.60	Captivate 2.0
Accuracy - Angle measurement	0.3 mgon[1]	0.3 mgon[2]
Accuracy - Distance measurement	1 mm + 1.5 ppm[1]	1 mm + 1.5 ppm[2]
Measurement time (typical)[3]	0.15 s[1]	0.05 s[2]
Working temperature range	−20°C to +50°C[1]	−20°C to +50°C[2]

[1](Leica, 2011, pp. 149-153)
[2](Leica, 2015, pp. 64-65)
[3]Continuous+/Continuously mode

3.1.2 GPS timing receiver and antenna

To determine the drift rate of the total station's internal time, the internal time was compared to the reference time (GPS time). The relation of the total station's internal time to the GPS time was achieved using a GPS timing receiver u-blox LEA-6T 0-0001 (S/N:000000307), depicted in Figure 3-2a, connected to the GPS antenna u-blox ANN-MS-0-005 (S/N:303805), depicted in Figure 3-2b.

(a) GPS receiver u-blox LEA-6T

(b) Antenna u-blox ANN-MS-0-005

Figure 3-2: GPS receiver and antenna used for total station internal time investigation

The accuracy of the PPS events sent by the GPS receiver is dependent on the time delay of the antenna cable and the receiver, generation and quantisation of the time pulse and on the position uncertainty caused by multipath or ionospheric delay (u-blox, 2011). The used GPS timing receiver u-blox LEA-6T enables PPS events with an accuracy of 3 ns (1σ), with compensation for previously mentioned error sources (u-blox, 2011).

3.2 Registration software

To achieve the relation of the total station's internal time to the GPS time, a registration software, which registers the PPS events of the GPS timing receiver, had to be developed (Figure 3-4). The GPS timing receiver presented in Section 3.1.2 was connected to the computer via a RS232 serial connector. Since the used computer does not come equipped with RS232 ports, a RS232 to USB adapter had to be used. The RS-232 serial communication is a communication between the Data Circuit-terminating Equipment (DCE), in our case the GPS receiver, and the Data Terminal Equipment (DTE) in our case the computer. For the RS232 communication to work, the parameters of baud rate, data bits, parity bits and stop bits have to be identical, both on the sensor and on the registration software. Additionally a Graphical User Interface (GUI) was developed to ease the changes of the program settings and communication parameter (Figure 3-3). In the following, the CPU time stamp denotes the time stamp of the computer's CPU.

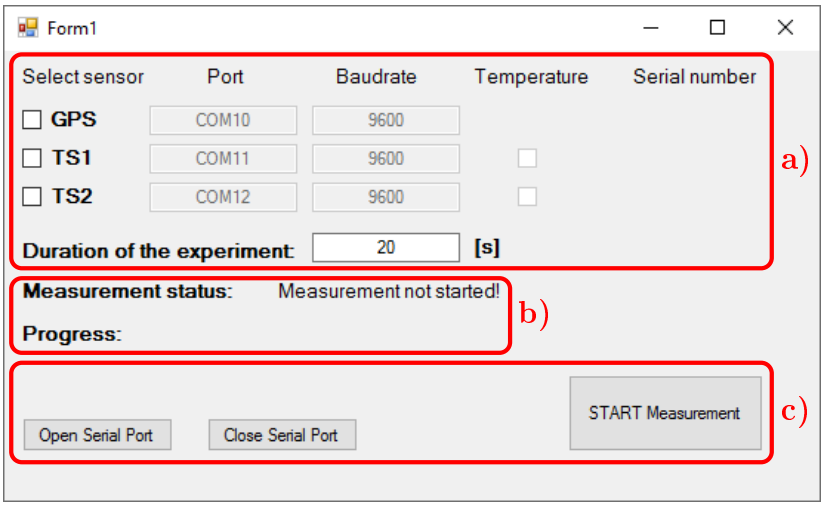

Figure 3-3: Graphical user interface of the registration software, divided into three main parts (a), b) and c))

The GUI is divided into three main parts:

a) **Communication part:** Sensors, communication parameters and type of measurements for the experiment are to be selected.

b) **Information part:** Information about the status and progress of the experiment.

c) **Control part:** Buttons used to control the software.

The step-by-step work flow of the registration software is presented in Figure 3-4.

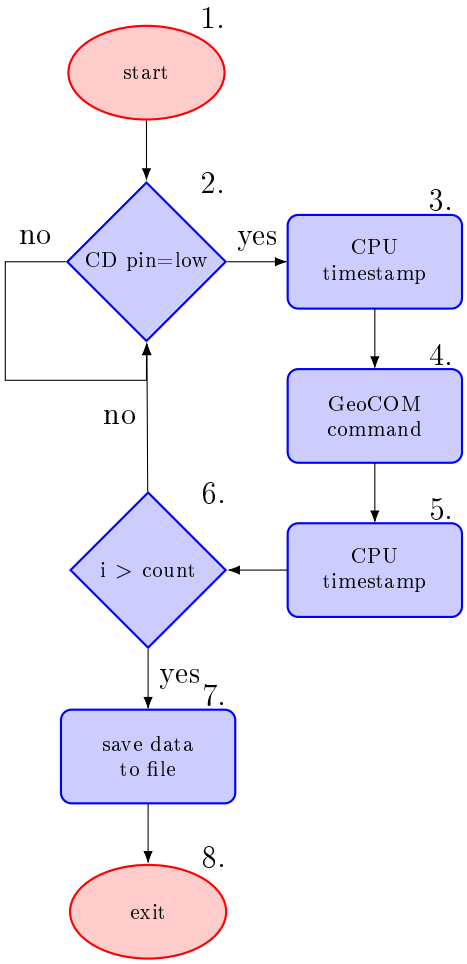

Figure 3-4: Flowchart of the registration software

1. After selecting the connection parameters and opening the serial ports (Figure 3-3), the registration process is started with the button "START Measurement".

2. A PPS event is sent to the serial port in form of a simple high/low status change on the Carrier Detect (CD) pin of a 9-pin serial port (pin 1). In step two, the CD pin is queried in a loop, until the pin status changes.

3. Immediately after the pin status change, the CPU time stamp of the pin status change and consequently the PPS event is recorded.

4. At the same time the GeoCOM command is sent to the connected total stations (see Section 3.3).

5. The input buffer of the serial ports, to which the total stations are connected, is queried and the computer's CPU time stamp is saved, when the first byte is available. Subsequently the whole GeoCOM message is read in and saved in a list.

6. If the number of iterations (PPS events) is lower or equal to the predefined boarder value, the process is repeated from step 2. Otherwise the registration process is completed,

7. and the data is saved to a text file for later evaluation.

8. Upon saving the text file, the program informs the user that the process is completed and closes the GUI.

A crucial part in developing a registration software is ensuring a high resolution and accuracy of the CPU time stamps. The CPU time stamp accuracy of the status change, is dependent on the resolution and the accuracy of the individual CPU time stamps and on the delay between the status change and the following query of the port. Due to its advantages (speed and GUI development) and easy communication with the sensors, the C# programming language was selected for the development of the registration software. Time stamps of the status changes were recorded using the stopwatch class, which is based on a *QueryPerformanceCounter* C++ function. According to MSDN (2016), the QueryPerformanceCounter function provides high-resolution time stamps, with a resolution $< 1\,\mu$s. In addition to the resolution of the QueryPerformanceCounter function, the number of the port queries per second directly influences the joint resolution of the CPU time stamps (Figure 3-5).

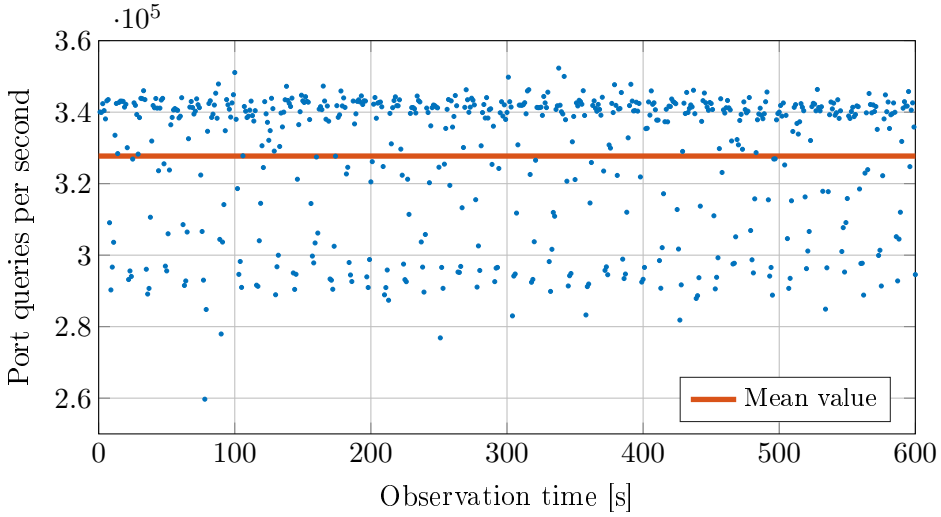

Figure 3-5: Registration software serial port queries per second

A short experiment (10 minutes) was carried out in order to test the performance of the registration software. As seen in Figure 3-5, the serial port is queried approximately 325000 times per second. This corresponds, to roughly one query every $3\,\mu$s. The minimal value of the queries per second obtained during this experiment (260000) corresponds to approximately $4\,\mu$s. This is still much better than the aspired accuracy of the synchronization routine and can therefore be neglected.

The high accuracy (ns range) of PPS events also enables the accuracy investigation of the CPU time stamps, as the standard deviation of the time difference of the CPU time stamps between two consecutive PPS events (Figure 3-6).

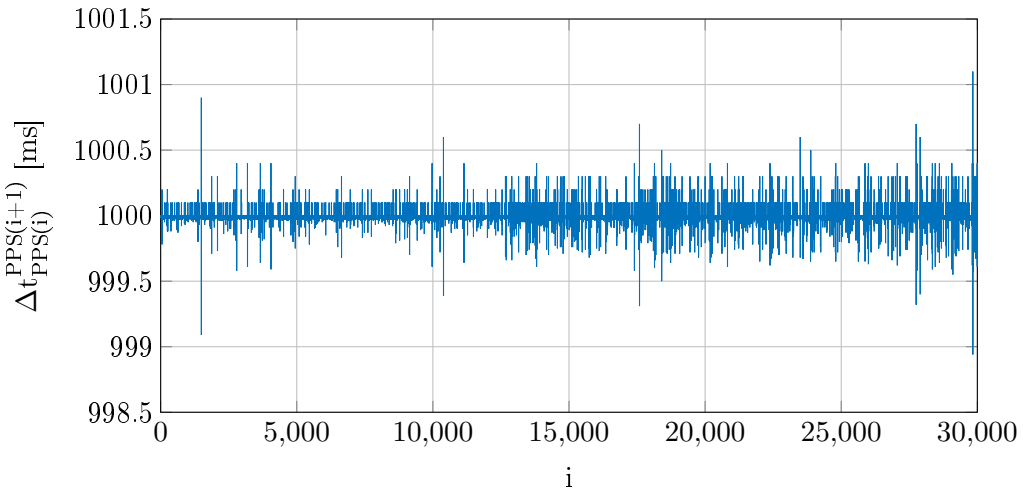

Figure 3-6: CPU time stamp time difference between two consecutive PPS events

An analysis was carried out for 30000 consecutive PPS events. The results are presented in Figure 3-6. The mean value of the time difference equals 1000.0 ms, which corresponds the 1 Hz frequency of the PPS events. The standard deviation (1σ) equals 45.7 μs and the maximal deviation from the mean value lies just above 1 ms. This is again much better than the aspired accuracy of the synchronization routine (Section 1.1) and can therefore be neglected.

3.3 Internal time of the instrument

Real time clocks are responsible for keeping track of the current time in almost all electronic devices, including the instruments used in the course of this thesis. Real time clocks are usually a part of the CPU and use crystal oscillator ticks as an arbitrary unit for measuring the internal time. Knowing the frequency of the ticks, the ticks can be converted to a more standard unit of time, e.g. milliseconds.

3.3.1 Internal time information using GeoCOM interface

During the investigation of the total station's internal time and later experiments, the instruments were remote controlled by a computer. The remote control of Leica instruments is enabled using a GeoCOM communication interface. GeoCOM interface enables a point-to-point communication between the client (computer) and the server (Leica instrument). A basic GeoCOM communication unit consists of a request and a corresponding reply (Leica, 2010, p. 7). Current GeoCOM implementation supports two ways of usage, a rudimentary ASCII protocol and a high-level function call interface (Leica, 2010, p. 7). In the course of this thesis, the more rudimentary ASCII protocol was used.

There are five GeoCOM commands implemented in Leica (2010) that return the information about the internal time of the instrument. Basic information about the individual commands is presented in Table 3-2.

Table 3-2: GeoCOM commands returning the information about the internal time of the instrument

GeoCOM command	Response (Internal time info.)	Resolution
CSV_GetDateTime	current time of the instrument	seconds
CSV_GetDateTimeCentiSec	current time of the instrument	centisecond
TMC_GetCoordinate	time stamp of distance measurement	millisecond
TMC_GetFullMeas	time stamp of distance measurement	millisecond
TMC_GetAngle1	time stamp of angle measurement	millisecond

The resolution of the time stamps directly influences the resolution of the time offset determination between the instrument's internal time and the GPS time. Last three GeoCOM commands presented in Table 3-2 return time stamps with millisecond resolution along with the measurement data, which can be used for the cross-correlation. GeoCOM commands TMC_GetCoordinate and TMC_GetFullMeas return the time stamps of the distance measurement, meaning, that the message contains the arbitrary time delay due

to the internal synchronization of the measurements (see Section 3.4). The GeoCOM command TMC_GetAngle1 returns the time stamp of the angle measurement, which is independent of internal synchronization. As the investigation of the instrument's internal time is based on a comparison with the GPS time, the latter was used in order to improve the accuracy of the time offset estimation (see Equation 2-8). For more information about GeoCOM communication interface and individual GeoCOM commands please refer to (Leica, 2010).

3.4 Internal synchronization of the subsystems

Modern robotic total stations combine measurements from various subsystems (sensors) for output of the coordinates (Kirschner and Stempfhuber, 2008). Electronic Distance Measurement (EDM) sensor, angle encoders, Automatic Target Recognition (ATR), PowerSearch, servo motor, two-axis tilt sensor and temperature sensor present main subsystems of the Leica robotic total stations. Each measurement of the individual subsystems is combined with the precise time stamp of the internal time. The following notations are adopted from Stempfhuber (2004, p. 75). The distance measurement is time stamped with the time stamp $t_{D,i}$, zenith distance measurement with the time stamp $t_{\zeta,i}$ and the horizontal direction measurement with the time stamp $t_{r,i}$. The output of the measurements occurs at the time $t_{out,i}$ and already includes the time needed for processing the data $\Delta t_{proc.,i}$. While the synchronization of the individual subsystems is not essential for static measurements, the insufficient synchronization in kinematic mode, results in a systematic error of position (see Figure 3-7 and Figure 3-8) (Stempfhuber, 2004).

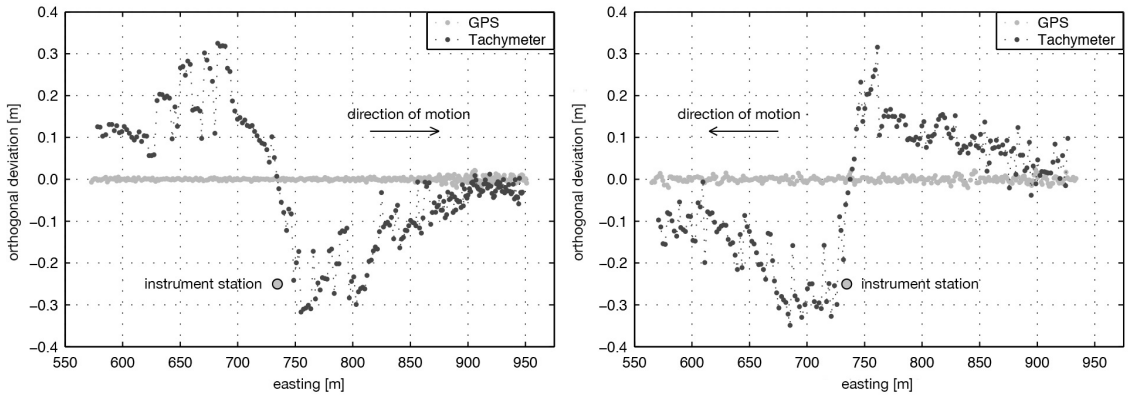

Figure 3-7: Systematic errors in kinematic observations, due to the insufficient synchronization of the subsystems (after Stempfhuber, 2004, p. 75)

In the early kinematic total stations, the systematic error was mainly caused due to the insufficient synchronization of the distance and angle measurements, which resulted in the latency time, defined as (Stempfhuber, 2009)

$$\Delta t_{D,r,i} = t_{D,i} - t_{r,i}\,. \tag{3-1}$$

The latency time was arbitrary, as the distance measurement was simply combined with the last available angle measurement. The resulting systematic error is presented in Figure 3-8.

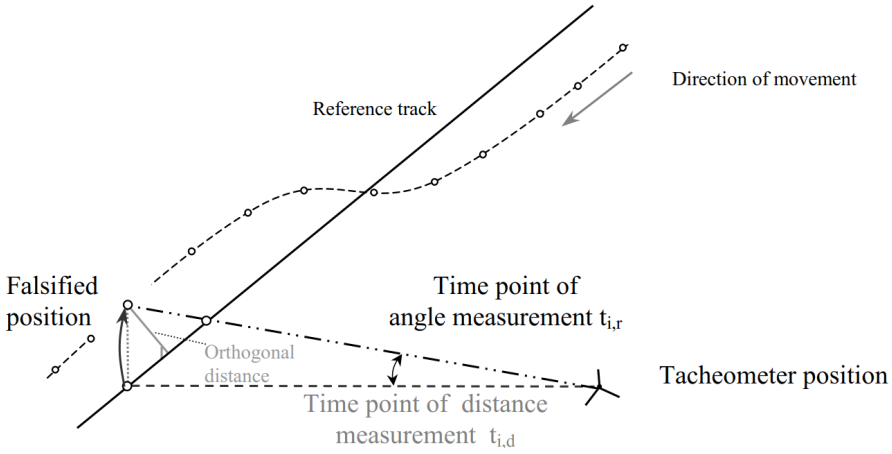

Figure 3-8: Position error due to the insufficient synchronization of distance and angle measurements (Stempfhuber, 2001, p. 373)

Apart from the latency time, the systematic position error due to the inssuficient synchronization is also dependent on the measurement configuration and velocity and the direction of the movement (Stempfhuber, 2004, p. 77). For more information about the impact of the individual parameter of the internal synchronization on the position accuracy, please refer to Stempfhuber (2004).

In the modern Leica robotic total stations (instruments from Leica TPS1200+ onward), the synchronization of the distance and angle measurements is performed internally, if the right distance measurement mode is selected. While in the distance mode SynchroTrack (Leica TPS1200+), Continuous+ (SmartWorx Viva) or Continuously (Leica Captivate) the linear interpolation between the previous and the following angle measurement, based on the time stamp of the EDM measurement, will be performed (Figure 3-9). This results in the synchronization of the angle and distance measurements, with $\Delta t_{D,r,i} < 1\,\text{ms}$ (Stempfhuber and Wunderlich, 2004; Stempfhuber, 2009).

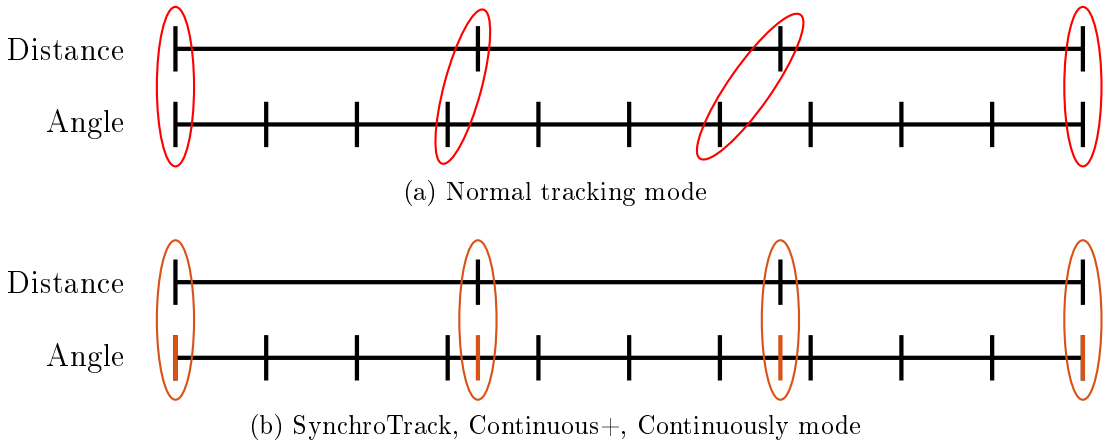

(a) Normal tracking mode

(b) SynchroTrack, Continuous+, Continuously mode

Figure 3-9: Combination of the angle and distance measurements, while in normal tracking mode or in SynchroTrack, Continuous+, Continuously mode

Interpolation of the angle measurements ensures the synchronization of the angle and distance measurements on the one hand, but on the other hand it increases the time offset between $t_{D,i}$ and $t_{out,i}$. Consequently it also makes the time offset arbitrary, as the time difference between $t_{D,i}$ and $t_{r,i+1}$ is arbitrary. Therefore the additional arbitrary parameter of the delay ($d_{Int.}$) has to be estimated in Equations 2-2, 2-7 and 2-8.

3.5 Measurement duration and dead time of the angle measurement

The angle measurement is a combination of measurements from different subsystems of the total station. The readings of the horizontal angle (Hz) and vertical angle (V) encoder are corrected with the measurements of the tilt sensor, to compensate for the vertical axis skew. If the angle measurement is performed using a Leica robotic total station, the ATR deviations from the line of sight, are mathematically applied to the Hz and V readings. For more information about the angle measurement principle in modern total stations, please refer to Joeckel et al. (2008, pp. 255-294).

In Leica instruments, the horizontal and vertical angle measurements are not carried out query-based, but are automatically updated internally, with the frequency of approximately 20 Hz. The first measurement following the query is assigned to the query and is returned in the response. This routine results in the arbitrary dead time $\Delta t^{res.}_{qry.}$ of the measurement, which denotes the time difference between the query and the following angle measurement. The dead time of the angle measurements is schematically represented in Figure 3-10.

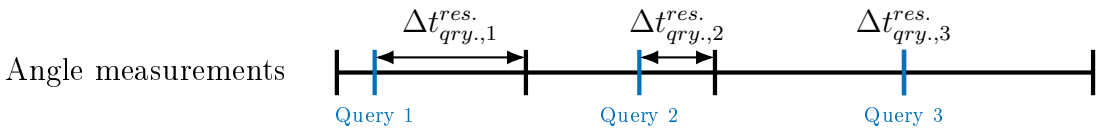

Figure 3-10: Schematic representation of the dead time of the angle measurements

The dead time of the angle measurement is arbitrary, but has a value between 0 and the sampling interval (approximately 50 ms) of the angle measurements. If the query and the measurement happen simultaneously, as presented in Figure 3-10 with Query 3, the $\Delta t^{res.}_{qry.}$ equals 0. An estimation of the dead time for individual measurements is not a straightforward task, but can be done in combination with the duration of the measurement. Performing measurements using GeoCOM commands, the duration time of the measurement is defined as

$$\Delta t^{duration}_{GeoCOM} = t^{received}_{GeoCOM} - t^{sent}_{GeoCOM}\,, \tag{3-2}$$

where t^{sent}_{GeoCOM} denotes the CPU time stamp of the sent GeoCOM command and $t^{received}_{GeoCOM}$ the CPU time stamp of the received GeoCOM response. As the duration of the measurement is not dependent only on the dead time of the measurement, the whole measurement routine needs to be analysed in order to bring them into relation. The measurement routine that composes the measurement duration is presented in Figure 3-11.

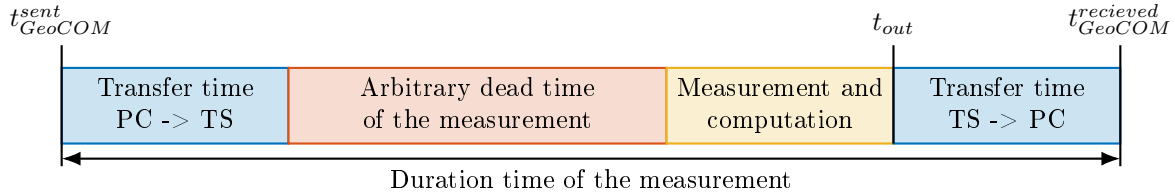

Figure 3-11: Time analysis of the angle measurement routine using GeoCOM interface

To obtain an estimation of the dead time of measurements, all other components of the duration time have to be known (estimated). The serial communication protocol 115200/8N1, used for the serial communication, denotes the communication parameters of 115200 bps (bits per second) baud rate, 8 data bits, no parity and one stop bit. Within this protocol, each character occupies 10 bits, one start bit, eight data bits and one stop bit. Knowing the length of the GeoCOM request and response strings, the transfer time can be calculated as

$$t_{trans.} = \frac{m_{char.} \cdot n^{char.}_{bits}}{baudrate}\,, \tag{3-3}$$

where $m_{char.}$ denotes the number of the characters in the string, and $n^{char.}_{bits}$ the number of bits per individual character. GeoCOM request TMC_GetAngle1 has a constant length of eleven characters, whereas the length of the response varies due to the variable number of the decimal places of the measurements, but it occupies approximately 133 characters. Considering all the parameters, the transfer time from the computer to the

total station equals approximately 0.95 ms and the transfer time in the opposite direction approximately 11.54 ms. Comparing the duration time of individual measurements, the transfer times can be assumed to be constant, due to only small variations (single digits) of the response string length (one character variation equals the time difference of 0.087 ms).

Both, performing the measurement and processing the data (applying tilt meter and ATR corrections to the encoder readings) are carried out internally, and as there are no significant changes in the CPU load, the time needed for this process can also be assumed to be constant. This leaves the dead time of the measurement as the only arbitrary part of the duration time of the measurements. Measuring the duration time of the measurement, the relative changes in the dead time can be extracted from the variations of the duration time. The duration and the dead time of measurements were more thoroughly investigated in the course of a one-hour experiment. For the purposes of this experiment, the PPS events were used as a trigger of the GeoCOM command TMC_GetAngle1, and the request and response of the GeoCOM command, were time stamped with the CPU time. The duration time was calculated using the Equation 3-2. Additionally, the time offset of the total station's internal time in regard to the GPS time was observed. The results of the test are presented in Figures 3-12, 3-13 and Tables 3-3, 3-4.

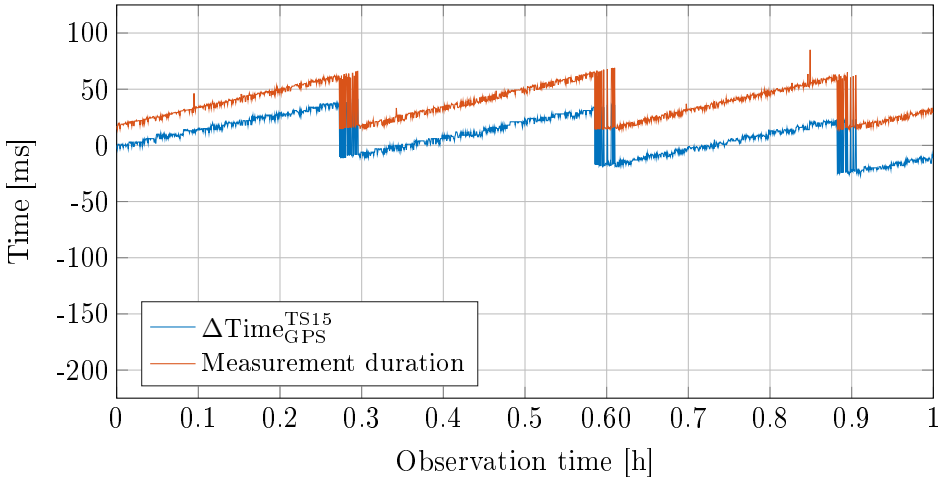

Figure 3-12: Duration of the measurement and offset of the internal time to GPS time using GeoCOM command TMC_GetAngle1 with Leica TS15

Table 3-3: Duration of the measurement using GeoCOM command TMC_GetAngle1 with Leica TS15

	Min.	**Max.**	$\boldsymbol{\Delta}_{\textbf{Min.}}^{\textbf{Max.}}$
Duration time	13.93 ms	69.02 ms	55.09 ms

In Table 3-3 it can be seen that the difference between the minimal and the maximal measurement duration time for the Leica TS15 instrument, corresponds to the reported sampling rate of 20 Hz. Considering the minimal duration time of the measurement and the values of the transfer times (0.95 and 11.54 ms), the time needed for the actual measurement and to process it, can be calculated. It is assumed to be constant and equals approximately 1.5 ms and can therefore be neglected. In Figure 3-12 it can also be observed that the duration of the measurement has to be taken into consideration when determining the offset of the internal time to the GPS time. The serrated shape of the offset plot is a direct consequence of the serrated shape of the measurement duration plot. Measurement duration plot has a serrated shape due to the characteristic, that the modulo of the sampling interval (app. 50 ms) and the PPS sampling interval (1000 ms) does not equal zero. As a result the remainder of the time rolls over to the next measurement, until the sum of the remainders is higher than the sampling interval of the measurement, and the "previous" measurement is combined with the request. This results in the sudden jump from the highest duration time of the measurement to the lowest.

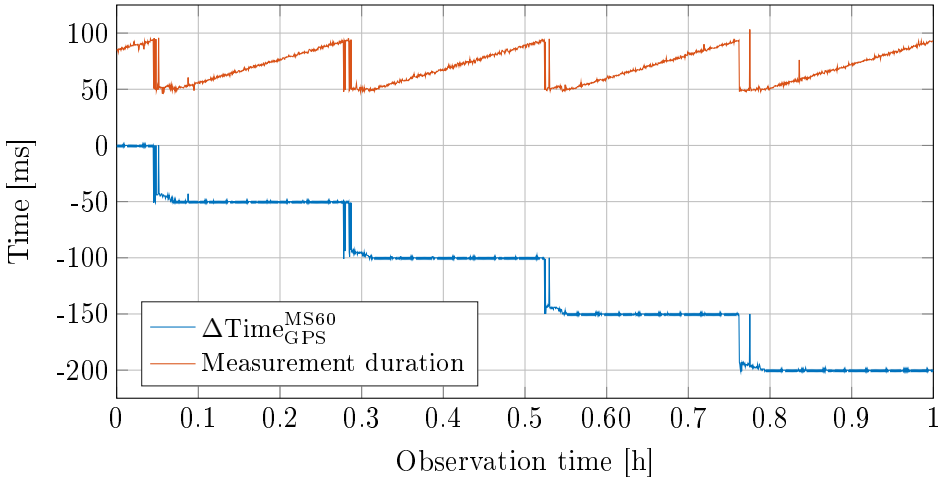

Figure 3-13: Duration of the measurement and offset of the internal time to GPS time using GeoCOM command TMC_GetAngle1 with Leica MS60

Table 3-4: Duration of the measurement using GeoCOM command TMC_GetAngle1 with Leica MS60

	Min.	**Max.**	$\boldsymbol{\Delta}_{\textbf{Min.}}^{\textbf{Max.}}$
Duration time	46.34 ms	95.76 ms	49.42 ms

The same experiment, performed with the Leica MS60, offers similar results to the one performed with the Leica TS15. In Figure 3-13, the serrated shape of the plot can be observed in the measurement duration plot, but not in the time offset plot. The time offset plot has a stepped shape, as a result of the characteristic that the modulo of the angle

measurement sampling interval and the PPS sampling interval equals zero when the angle measurement sampling interval is expressed in the internal time. On the other hand, it does not equal zero when both are expressed in the GPS time. The time difference between the highest and the lowest measurement duration again corresponds approximately to the 20 Hz angle measurement update rate. The lowest measurement duration of 46.34 ms shows that the actual measurement and processing of it take a lot more time with the used Leica MS60 compared to the used Leica TS15. As a consequence, it is assumed that the sampling rate of the angle measurements performed with GeoCOM command TMC_GetAngle1, is lower when using the Leica MS60 instrument than the Leica TS15. To confirm this assumption, a short experiment was carried out in order to determine the sampling rate of both instruments. The results are presented in Figure 3-14.

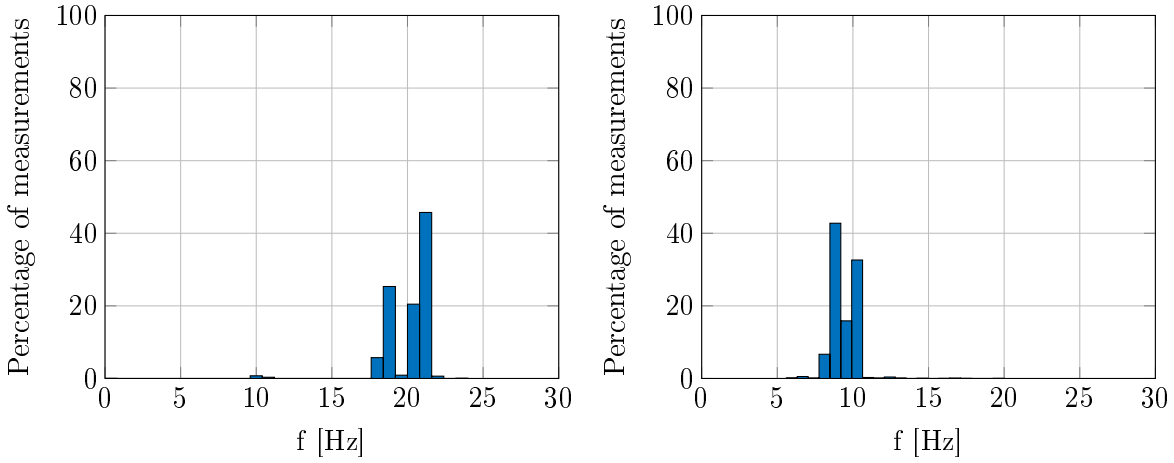

(a) Leica TS15

(b) Leica MS60

Figure 3-14: Distribution of the measurement frequency of 3000 angle measurements, performed using the Leica TS15 and Leica MS60 instruments, with GeoCOM command TMC_GetAngle1

The frequency of the measurement is expressed in the internal time. The results are in accordance with the findings of Lienhart et al. (2016), and confirm the assumption made about the lower measurement frequency of the used Leica MS60 instrument with the firmware Captivate 2.0. Even though, the USB-to-RS232 adapter was used with the Leica TS15 instrument (necessary, since the used laptop does not posses a serial connection port), a drop in the measurement frequency is not observed. According to Lienhart et al. (2016), the higher measurement frequency of Leica MS60 can be obtained by using GeoCOM command TMC_GetFullMeas.

3.6 Drift rate of the internal time

Drift rate denotes the offset of the clock from some ideal reference clock, per unit of time. If the drift rate is small enough, no compensation is necessary. To determine the drift rate of the instrument's internal time, an experiment was carried out where the offset of the

internal time to the reference time (GPS time) was determined periodically over a longer period of time. The experiment was carried out in an office, at IGMS of Graz University of Technology. The meteorological conditions in the office are fairly stable (temperature around 22°C) and no big temperature changes were expected. Due to the comparison with the GPS time, the experiment could not be carried out in the climatically controlled IGMS laboratory, as the laboratory is located underground. The measurement configuration of the experiment is presented in Figure 3-15.

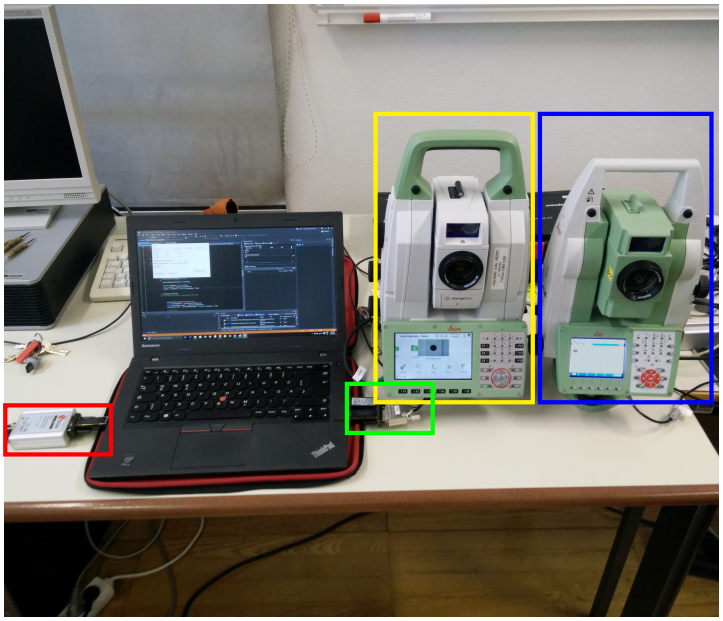

(a) Total stations connected to the laptop (red - GPS receiver, yellow - Leica MS60, blue - Leica TS15, green - total station connection to the laptop)

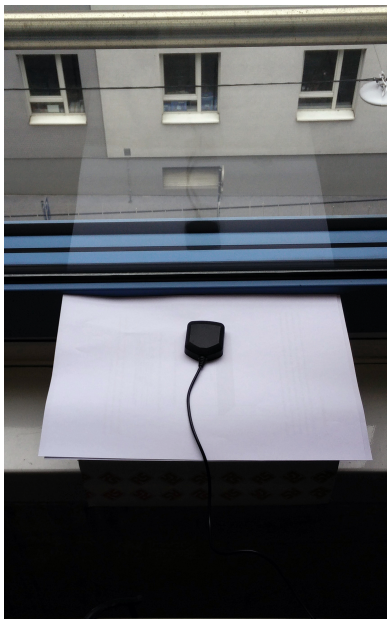

(b) GPS antenna on the window of the office

Figure 3-15: Instruments used for the drift rate experiment

The instruments were connected to the computer as presented in Section 2.2.3 and the registration software presented in Section 3.2 was used to control the instruments and to time stamp the events. The duration time of the experiment was selected based on the normal measurement duration of a one-day project (see Section 1.1), i.e. eight hours. The offset of the internal time to the GPS time was calculated using simplified Equation 2-8 (message delay can be assumed to be constant and the last term can be neglected due to the usage of angle measurements). Assuming the linear relation of the time offset to the duration time at the constant temperature, the linear regression line

$$y = a + bx + \epsilon\,, \tag{3-4}$$

can be estimated with Least Squares Adjustment (LSA). The offset at the start of the experiment (intercept a), was set to zero and was later considered as fixed in the solution, whereas the slope of the line (b), corresponds the drift rate of the instrument's internal time. The results of the experiment are presented in Table 3-5 and Figure 3-16. Please note the different scaling of the y-axis of Figure 3-16a and Figure 3-16c.

Table 3-5: Drift rate of the Leica TS15 and Leica MS60 instruments and the residuals of the linear regression model

Instrument	**Duration [h]**	**a [ms]**	**b [ppm]**	**max(ΔT) [ms]**	σ_r [ms]
Leica TS15	8	0	-7.1	-206.38	1.4
Leica MS60	8	0	-57.9	-1665.1	1.3

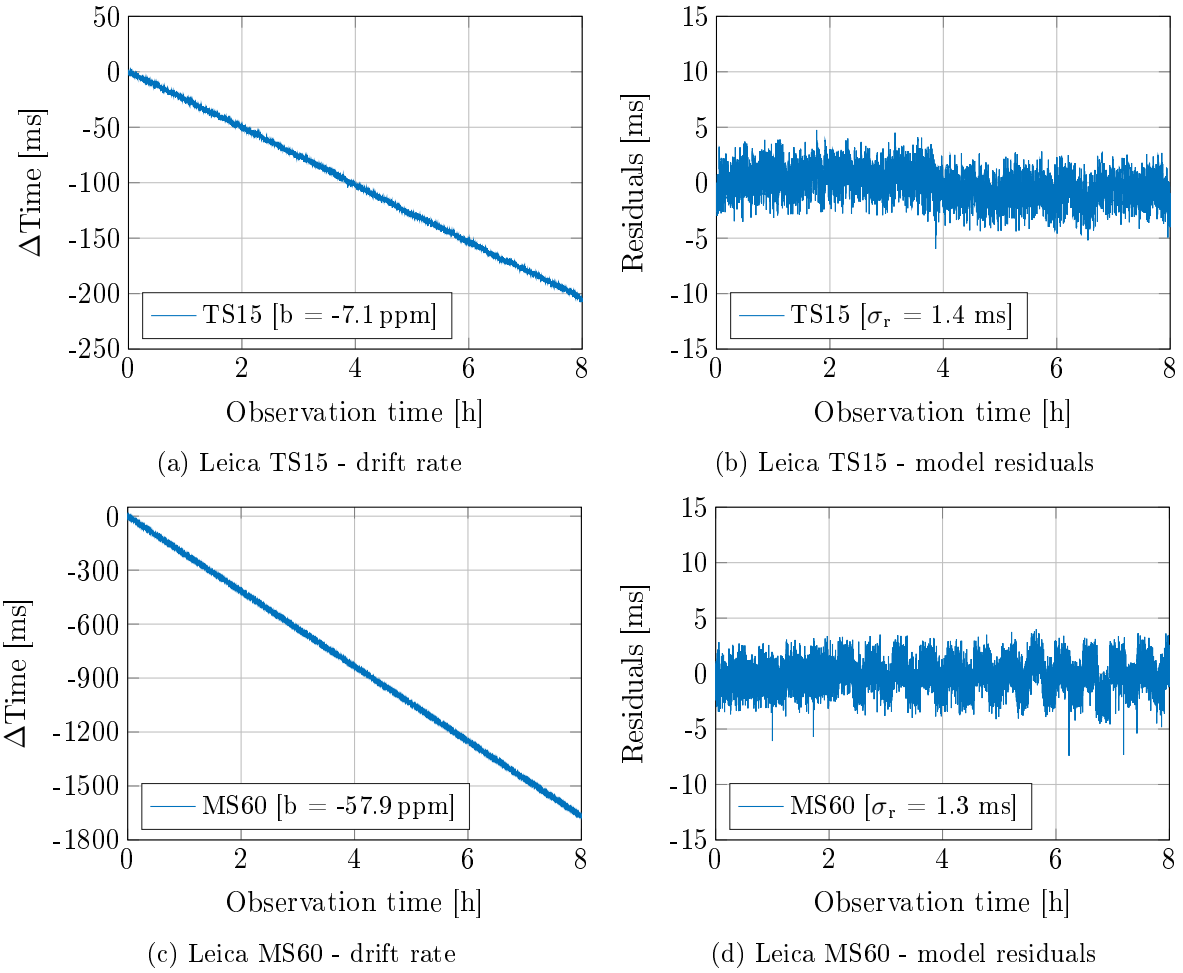

(a) Leica TS15 - drift rate

(b) Leica TS15 - model residuals

(c) Leica MS60 - drift rate

(d) Leica MS60 - model residuals

Figure 3-16: Drift rate of the Leica TS15 and Leica MS60 internal time and the residuals of the linear regression model

The experiment confirmed the assumption, about a constant drift rate at a constant temperature (at least for short measurement durations, e.g. a couple of hours). The drift rate of the used Leica MS60 is around 8.2 times higher than the drift rate of the used Leica TS15. It equals 57.9 ppm at approximately 22°C, which corresponds to 1.66 second per eight hours. Considering the measurement rate of 10 Hz, in this time frame 16 measurements are performed. The time offset of both instruments after eight hours is well above the aspired accuracy of the synchronization routine and well above the current internal synchronization accuracy (Section 3.4) of the instruments. Thus the time drift of the internal time of both instruments has to be compensated.

3.7 Temperature dependency of the instrument's internal time

3.7.1 Temperature dependency of crystal oscillators

Crystal oscillators are electrical circuits, used for the generation of the sinusoidal waveform. The frequency of the waveform is controlled by a piezo-electric crystal, which is usually a quartz crystal (Amos and Amos, 2002, p. 76). Crystal oscillators offer great stability and are often used as frequency standards in signal generators (Amos and Amos, 2002, p. 76). The frequency of crystal oscillators is commonly used to keep track of the time in electronic devices. To keep an accurate track of the time, the frequency of crystal oscillators has to be as constant as possible. The term used to describe the constancy of the oscillator's frequency under specific conditions, is frequency stability (Amos and Amos, 2002, p. 140). Frequency stability is in the short term mostly affected by environmental changes, especially temperature changes. In the long term the frequency stability is also affected by aging of the quartz crystal resonator (Frerking, 1978, p. 14). Quartz crystal, used as a resonator is obtained by cutting the crystal at specific angles to the defined axis of the crystal. The physical and electrical parameters of the resonator are dependent on the angles of the cuts (Hewlett-Packard, 1997).

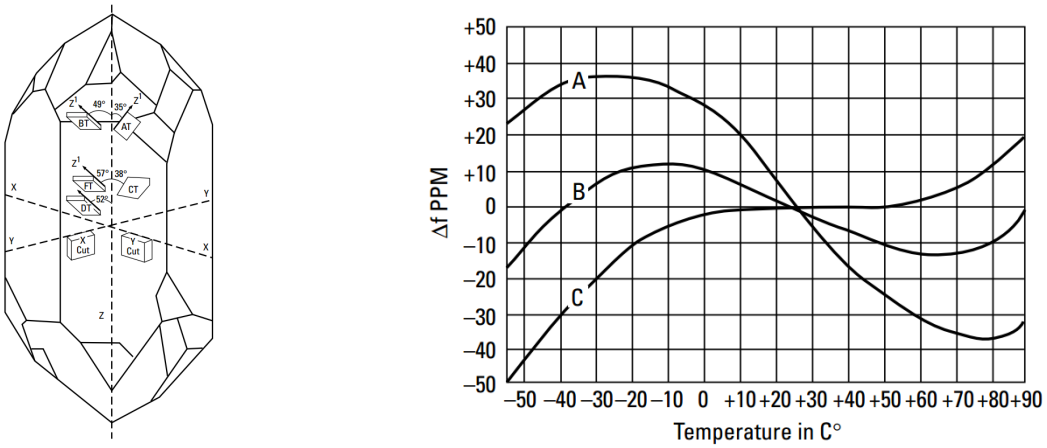

(a) Typical quartz crystal cuts (Hewlett-Packard, 1997, p. 6)

(b) Frequency change versus temperature characteristic for three AT-cut quartz crystals, with a slight changes in the angle of the cut (Hewlett-Packard, 1997, p. 11)

Figure 3-17: Temperature characteristic of the quartz crystal based on the type of the cut

The AT-cut type resonators presented in Figure 3-17 are widely used in electronic devices, as they offer high frequency stability over a wide temperature range. The AT-cut quartz crystals have a cubic dependence of the frequency on the temperature, which is in contrast with most other cuts that have a parabolic dependence (Frerking, 1978, p. 130). The cubic function of temperature can be controlled with small changes in the angle of the cut, as presented in Figure 3-17b, but nevertheless the temperature dependency of the frequency cannot be eliminated. Due to need of a higher frequency stability, the

Temperature Compensated Crystal Oscillators (TCXO) were developed. With the temperature compensation of crystal oscillators, a frequency stability in the range of ±10 to ±0.5 ppm can be achieved (Frerking, 1978, p. 16). Higher frequency stability is only obtainable under special conditions. TCXO contain an additional circuit, which compensates the temperature effect on the crystal oscillator (Frerking, 1978, p. 16). The result of the AT-cut crystal oscillator's temperature compensation is presented in Figure 3-18.

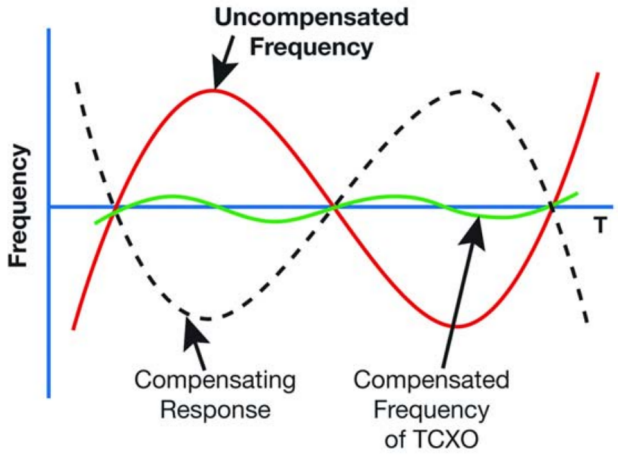

Figure 3-18: Temperature compensation of the AT-cut crystal oscillator (Cerda, 2005, p. 42)

Most of the electronic devices are equipped with AT-cut crystal oscillators, therefore a cubic dependence of the frequency on the temperature is assumed for the used instruments. For more information about crystal oscillators and their temperature dependency, please refer to Frerking (1978).

3.7.2 Internal temperature information using GeoCOM interface

The crystal oscillator is a part of the instrument's CPU and has as such a similar temperature as the CPU. The internal temperature of the instrument is usually higher than the ambient temperatures, as the power consumption of the CPU ends up converted into heat energy. Instruments used in the course of this thesis come equipped with an internal thermometer, located on the motherboard. Internal thermometer offers the best estimation of the crystal oscillator's temperature and being a part of the instrument, no additional temperature sensors are needed. Using GeoCOM interface, the internal temperature of the instrument can be obtained with the CSV_GetIntTemp command (Leica, 2010, p. 126). The response of the command contains the internal temperature of the instrument, reported in degrees Celsius.

3.7.3 Experiment at variable temperature

The dependency of the drift rate on temperature can be investigated with a drift rate experiment at a variable temperature. Such experiment was carried out at the test bay on the roof of the TU Graz geodesy building (Steyrergasse 30). The measurement configuration (Figure 3-19) and procedure were identical to the drift rate experiment presented in Section 3.6. Additionally, an internal temperature measurement was carried out after each angle measurement, using GeoCOM command CSV_GetIntTemp. Furthermore, a weather station Thommen HM30 (SN:0038748) was used for the reference temperature measurements.

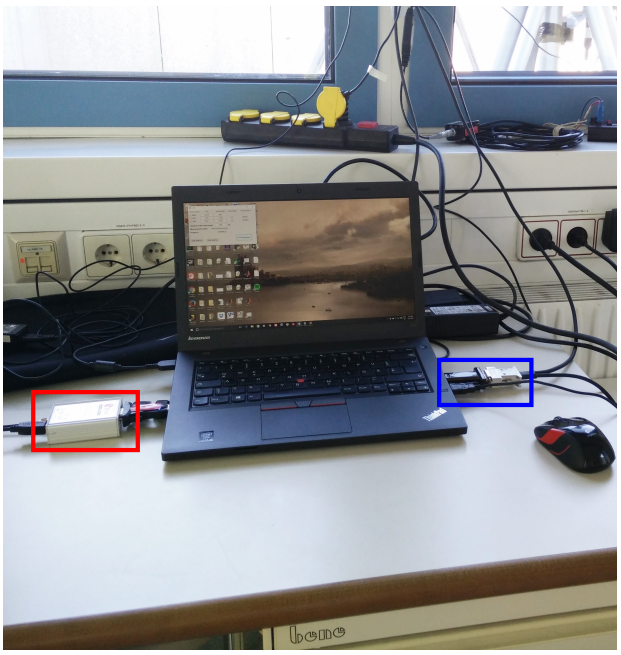

(a) Inside the building (red - GPS receiver, blue - connection of the instruments to the laptop)

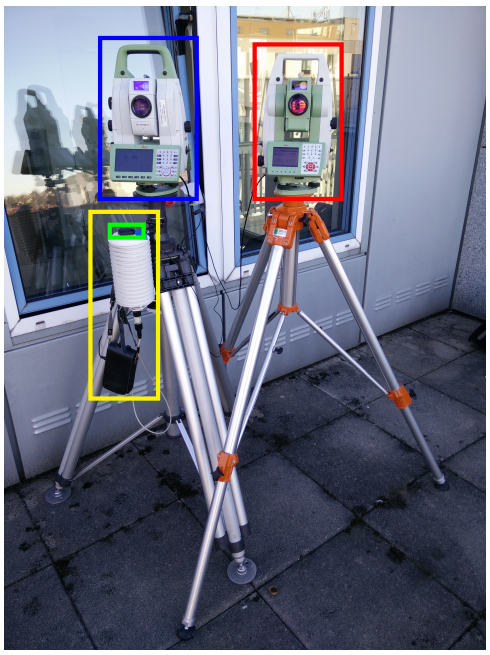

(b) Outside the building (green - GPS antenna, blue - Leica MS60, red - Leica TS15, yellow - weather station)

Figure 3-19: Measurement configuration of the drift rate experiment at variable temperature

The experiment was started on 22.2.2016 at 15.51 o'clock and lasted for 24 hours, so that the whole day cycle was included. The offset of the instrument's internal time to the GPS time was again calculated using simplified Equation 2-8. Figure 3-20 depicts the results of the temperature measurements and the drift rate of the instruments during the experiment.

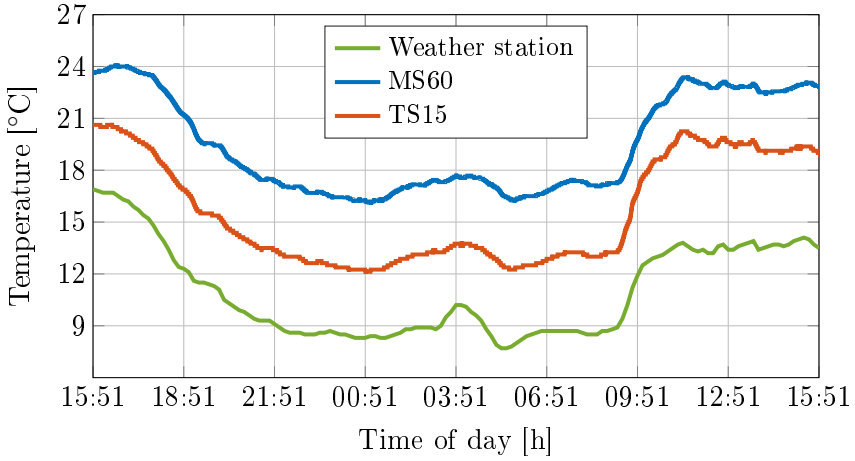

(a) Temperature measurements

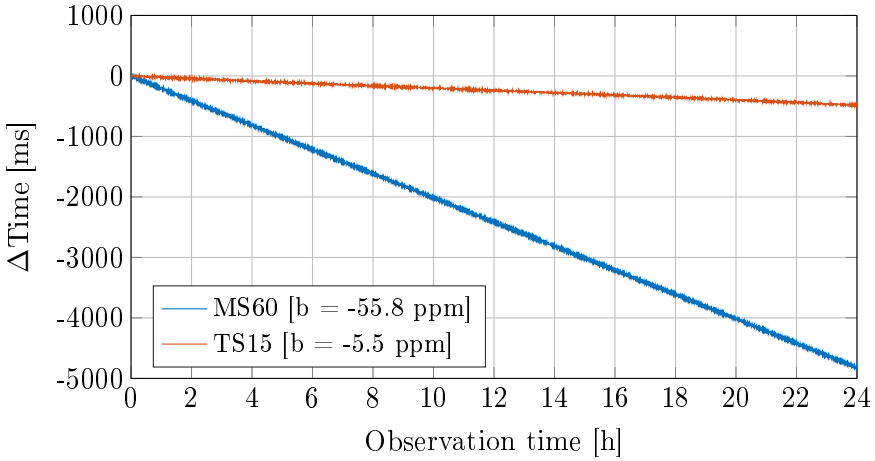

(b) Time offset of the instrument's internal time to GPS time

Figure 3-20: Results of the drift rate experiment at variable temperature

Figure 3-20a shows that the internal temperature of the instruments follows the changes of the ambient temperature. The experiment also confirmed that the internal temperature of the instrument is higher than the ambient temperature, as already assumed in Section 3.7.2. The drift rates of the instruments differ from the drift rates obtained with the experiment at a constant temperature. Nevertheless, a conclusion about the temperature dependency of the instrument's internal time cannot be drawn, without further analysis. To single out the temperature effect on the internal time, the constant, mean drift rate (estimated with LSA) was subtracted from the time offset, Figure 3-21.

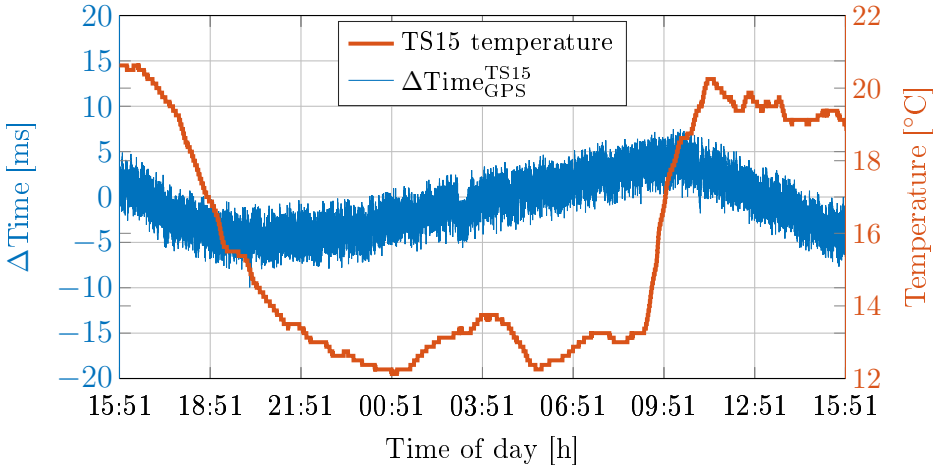

(a) Leica TS15

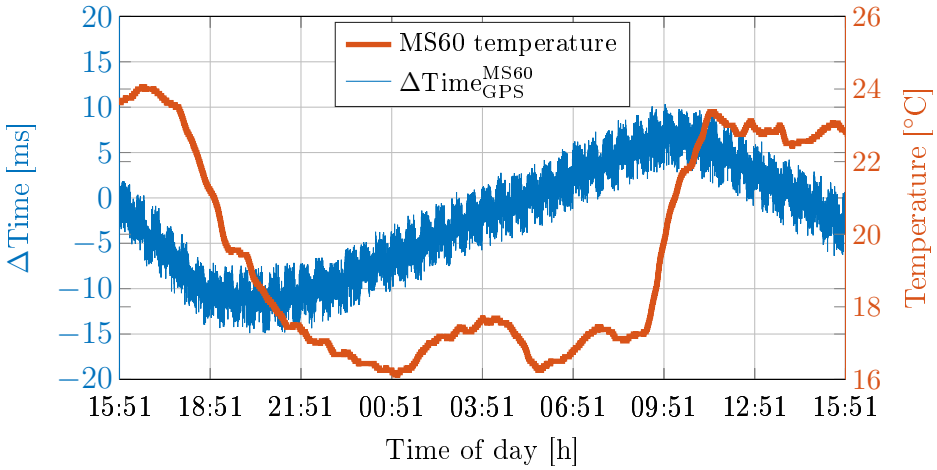

(b) Leica MS60

Figure 3-21: Results of the drift rate experiment at variable temperatures, after subtraction of the constant drift rate estimate

Results of the experiment, presented in Figure 3-21 show that after a subtraction of the constant drift rate, a distinct systematic remains in the time offset plot of both instruments. The systematic is correlated with the temperature change, as can be seen from the internal temperature plot. Subtraction of the constant drift rate estimate already greatly reduces the drift rate of the crystal oscillator. The remaining systematic is caused by the temperature changes. Determining and applying the temperature-dependent correction function should therefore yield even better results.

4 Calibration of the instrument's internal time

According to ISA (2003, p. 66), the calibration is defined as "The determination of the experimental relationship between the quantity being measured and the output of the device that measures it. The quantity measured is obtained through a recognized standard of measurement." Experiments in Section 3 show a clear dependence of the internal time on temperature. In order to achieve the aspired accuracy of the time synchronization, the temperature effect has to be compensated. The experiment, described in Section 3.6, confirmed the assumption of the constant drift rate at a constant temperature. Based on the theory of crystal oscillators, presented in Section 3.7.1, a cubical relation of the drift rate to temperature is expected. Evaluating the internal time drift rate at constant temperatures, the cubic calibration function can be empirically determined as the best model fit, to the drift rates obtained at individual temperatures. The calibration procedure in the course of which, the calibration function was determined, can be divided into four steps:

1. Drift rate experiments in climate chamber, using equally distributed temperature steps across the whole temperature operating range of the total station
2. LSA of the linear regression of the time offset as a function of the duration time
3. LSA model fit to the linear regression coefficients from the second step
4. Evaluation of the model, by comparison of the result with an independent, reference measurement at variable temperature

The so defined calibration procedure was used for calibration of the total station's internal time. Together with the cross-correlation, the calibration function forms a base of the real-time synchronization routine. Above listed steps of the calibration procedure are explained in detail in Sections 4.3 to 4.5.

4.1 Used instrumentation

Alongside the hardware, listed in the Section 3.1.2, a climate chamber Memmert ICP400 (Figure 4-1) was used to assure an optional, constant temperature of the instruments. The Memmert ICP400 climate chamber offers a setpoint temperature range from 0°C to 60°C, with a setting accuracy of 0.1°C. It also enables "programme operation" mode, with up to 40 programmable temperature-time ramps (Memmert, 2011, p. 17). This mode was especially beneficial for the independent experiment at a variable temperature, presented in Section 4.5. The climate chamber also comes equipped with a cable hole in the left side of the chamber. The hole around the cable is sealed with a rubber seal to prevent the airflow.

(a) Memmert ICP400

(b) Leica TS15 in climate chamber Memmert ICP400 (red - cable hole)

Figure 4-1: Climate chamber Memmert ICP400, used for calibration of the instrument's internal time

Even though the opening of the climate chamber is rather small, the Leica TS15 fits perfectly into it, as can be seen in Figure 4-1. The Leica MS60 is higher, and does not fit in the climate chamber unless the carrying handle is taken off, as presented in Figure 4-2. The carrying handle naturally has no effect on the instrument's internal time; therefore the experiments were carried out without it.

Figure 4-2: Leica MS60, without the carrying handle, in the climate chamber Memmert ICP400

4.2 Registration and evaluation software

Calibration of the instrument's internal time is based on the comparison of the internal time with the GPS time. For the registration of both, the registration software presented in Section 3.2 was used. Due to the limited space in the climate chamber, only one total station was used at a time. A recorded text file, containing the time stamps of the measurements (output of the registration software), was later analysed using the evaluation software.

The evaluation software comprises two blocks, one responsible for the second step of the calibration procedure and the other for the third step of the calibration procedure (see Section 4). The data representation is a major part of both blocks; therefore MATLAB R2016a was selected as the platform for the development. Please note that the first block is carried out for each individual measurement at a constant temperature. On the other hand, the second block is carried out only once per instrument, when all the measurements at the constant temperatures are completed and the linear regression coefficients are estimated. Figure 4-3 depicts the flowchart of the evaluation software blocks.

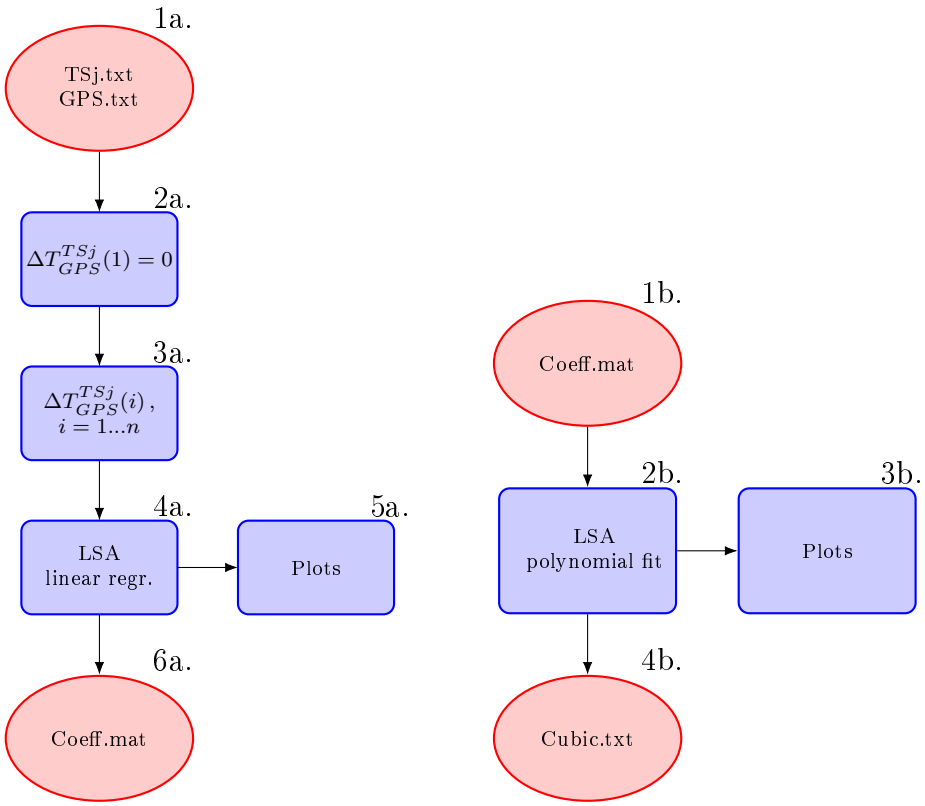

(a) first block (b) second block

Figure 4-3: Flowchart of the evaluation software

First block:

1a. Output text files (GPS.txt and TSj.txt) of the registration software are read in, and PPS events are combined with the total station measurements, based on the CPU time stamps.

2a. Offset of the total station's internal time to GPS time at epoch 1 is calculated and set to zero. Following time stamps of the total stations's internal time are corrected accordingly.

3a. The time offset is calculated using the simplified Equation 2-8. The arbitrary message delay $d_1(i)$ can be assumed to be constant if the dead time of the measurements is considered. Furthermore, the message delay due to the internal synchronization $d_{Int.}^{TS1}$, can be omitted, as the GeoCOM command TMC_GetAngle1 is used.

4a. A linear regression of the time offset as a function of duration time is estimated using the LSA.

5a. Model residuals are calculated and plotted. Additionally, a histogram plot and a Q-Q plot are plotted in order to test if residuals follow the normal distribution.

6a. The slope of the regression line (b) and its standard deviation from LSA are saved in a MATLAB proprietary, binary file format ".mat", alongside with the mean internal temperature, for the later evaluation in the second block of the software.

Second block:

1b. Individual output files of the first block are read in.

2b. Using LSA, a cubical function dependent on temperature is fitted to the linear regression coefficients, obtained in the fourth step of the first block.

3b. The so obtained calibration function is plotted together with the linear regression coefficients.

4b. Polynomial coefficients of the calibration function are saved in the text file, together with their standard deviations.

4.3 Climate chamber experiment

Constant temperature conditions were ensured with the help of the climate chamber presented in Section 4.1, which was provided by IGMS. Note that the temperature range of the climate chamber is smaller than the temperature range of the instruments. Therefore only temperatures above 0°C were investigated. For the experiments, a six-hour duration time, in equally distributed steps of 10°C up to the maximal working temperature of the instruments was selected. Measurement plan for individual climate chamber experiments is presented in Table 4-1.

Table 4-1: Climate chamber experiment - measurement plan

Instrument	**Duration [h]**	**Temperature [°C]**
Leica TS15 or MS60	6	0
Leica TS15 or MS60	6	10
Leica TS15 or MS60	6	20
Leica TS15 or MS60	6	30
Leica TS15 or MS60	6	40
Leica TS15 or MS60	6	50

Pleas note that the temperatures in Table 4-1 denote ambient temperatures provided by the climatic chamber. Actual internal temperatures of the instruments are expected to be a few degrees higher. Before each experiment, the instruments were acclimatized to the ambient temperature.

4.3.1 Leica TS15

Results of the climate chamber experiment for the used Leica TS15 are presented in Figure 4-4 and Table 4-2. Note that the Figure 4-4, depicts only results of the experiment at 0°C ambient temperature. Results of the experiments at other ambient temperatures are presented in Appendix A.1.

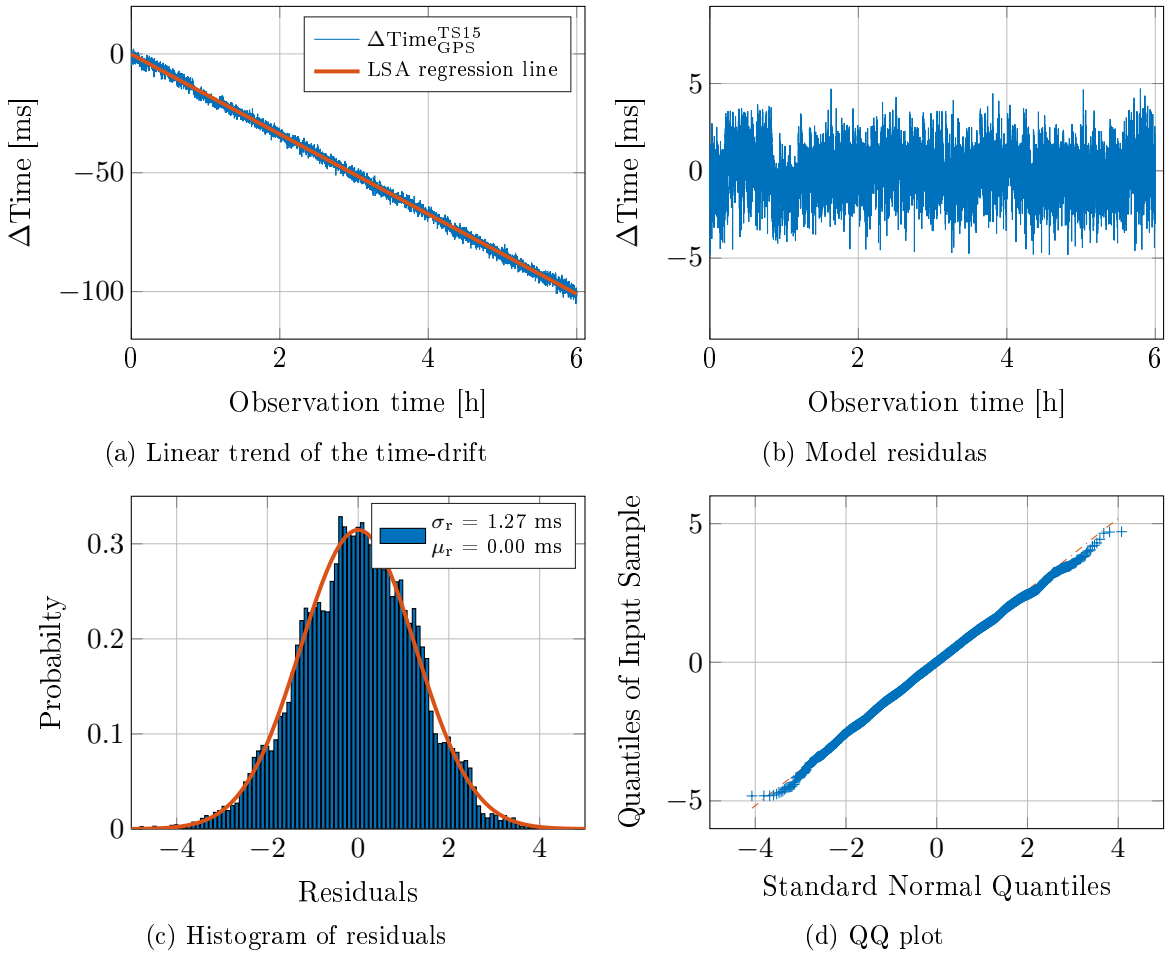

(a) Linear trend of the time-drift

(b) Model residulas

(c) Histogram of residuals

(d) QQ plot

Figure 4-4: Results of the Leica TS15 climate chamber experiment at 0°C ambient temperature

Table 4-2: Results of the climate chamber experiments for Leica TS15

Internal temperature [°C]	σ_T **[°C]**	**b [ppm]**	σ_b **[ppm]**
3.26	0.03	-4.67	0.001
13.02	0.06	-5.35	0.001
22.77	0.04	-6.38	0.001
32.32	0.06	-7.90	0.003
42.01	0.06	-8.99	0.001
51.89	0.04	-9.16	0.001

Residuals of the regression line follow the Gaussian normal distribution, as can be seen in Figures 4-4c and 4-4d, confirming the constant drift rate of the instrument's internal time, at a constant temperature. Relating to second column of Table 4-2, the used climate chamber ensures a stable temperature over time. The difference between the ambient temperature and the internal temperature of the instrument equals around 3°C and diminishes, as the temperature rises. As predicted, the drift rate of the instrument's internal time is greater at higher temperatures. High accuracy of the individual coefficients b depicts a good outlook for the cubic calibration function estimation. Similar results can be observed for other ambient temperatures in Appendix A.1.

4.3.2 Leica MS60

Results of the climate chamber experiment for the used Leica MS60 are presented in Figure 4-5 and Table 4-3. Note that the Figure 4-5, depicts only results for the experiment at 0°C ambient temperature. Results of the experiments at other ambient temperatures are depicted in Appendix A.1.

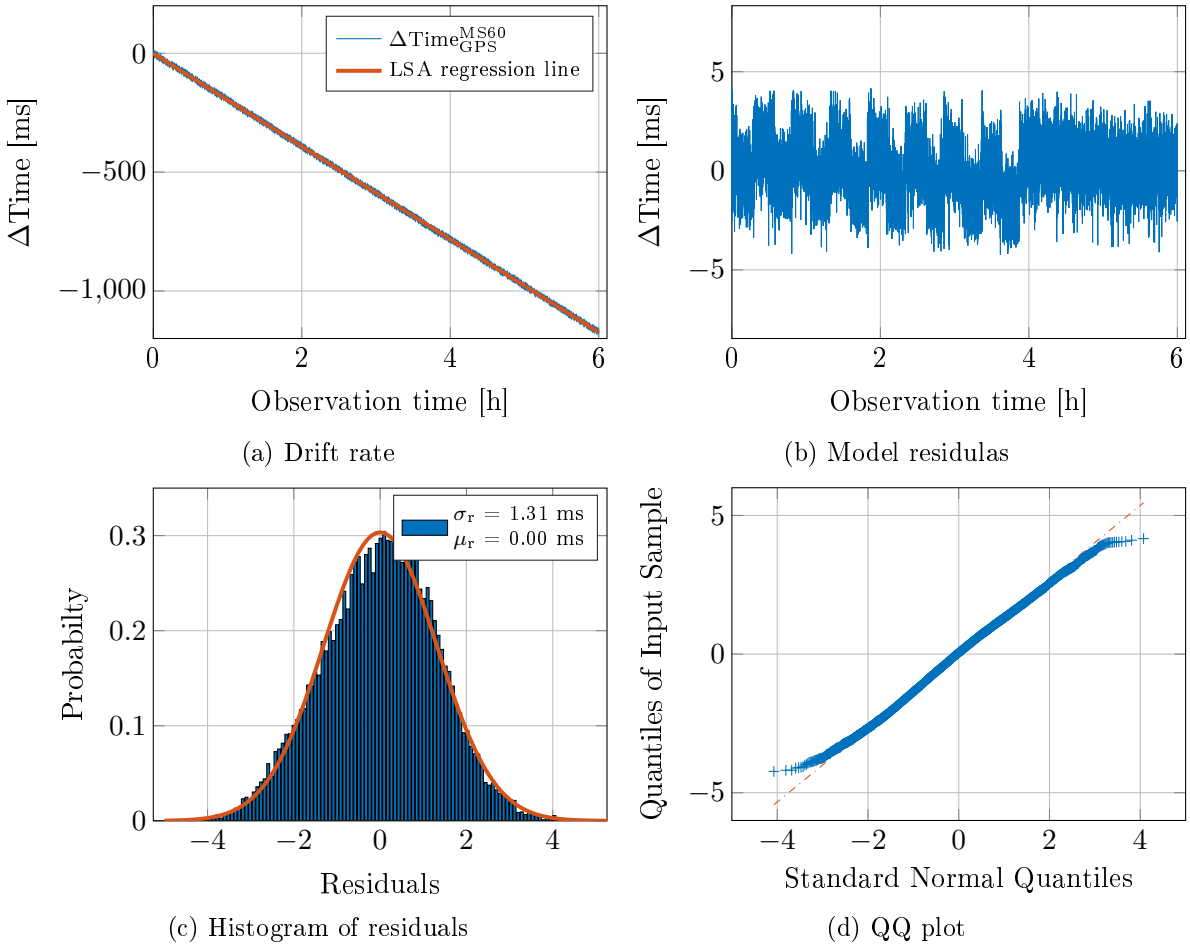

(a) Drift rate

(b) Model residulas

(c) Histogram of residuals

(d) QQ plot

Figure 4-5: Results of the Leica MS60 climate chamber experiment at 0°C ambient temperature

Table 4-3: Results, of the climate chamber experiments for Leica MS60

Temperature [°C]	$\sigma_{\mathbf{T}}$ **[°C]**	**b [ppm]**	$\sigma_{\mathbf{b}}$ **[ppm]**
5.84	0.03	-54.31	0.001
15.77	0.06	-55.14	0.003
25.46	0.07	-56.83	0.002
34.91	0.04	-58.43	0.002
44.81	0.06	-59.64	0.002
54.28	0.03	-59.68	0.002

In contrast to the linear regression residuals by the used Leica TS15, the residuals by the used Leica MS60 do not entirely follow the Gaussian normal distribution. This can be observed at higher ambient temperatures, and is especially unambiguous at 40 and 50°C ambient temperature. The remaining systematic in the residuals is of unknown source. Due to the low amplitude of the residuals, no additional attention was devoted in determining the source of the systematic (see Figure 4-5b). Similar as with the used Leica TS15, the drift rate raises with the temperature. In accordance with the results of the used Leica TS15, the difference between the highest and the lowest drift rate of the internal time equals approximately 5 ppm. Apart from the systematic in residuals at higher temperatures, the results presented in Appendix A.2 are in accordance with the Figure 4-5.

4.3.3 Comparison of the drift rates

The climate chamber experiment confirmed the higher drift rates of the used Leica MS60 internal time in comparison with the used Leica TS15. As depicted in Figure 4-6, the difference between the drift rates at the same internal temperature is approximately 50 ppm. Apart from the offset, instruments show a similar (cubic) temperature dependence.

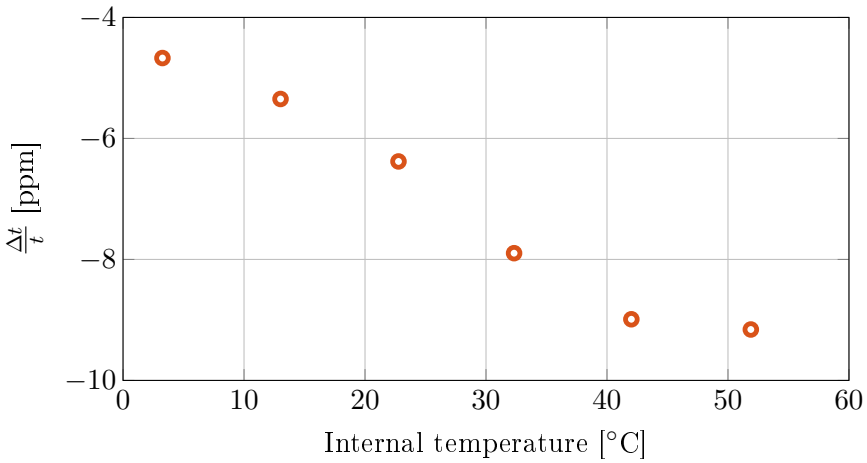

(a) Leica TS15

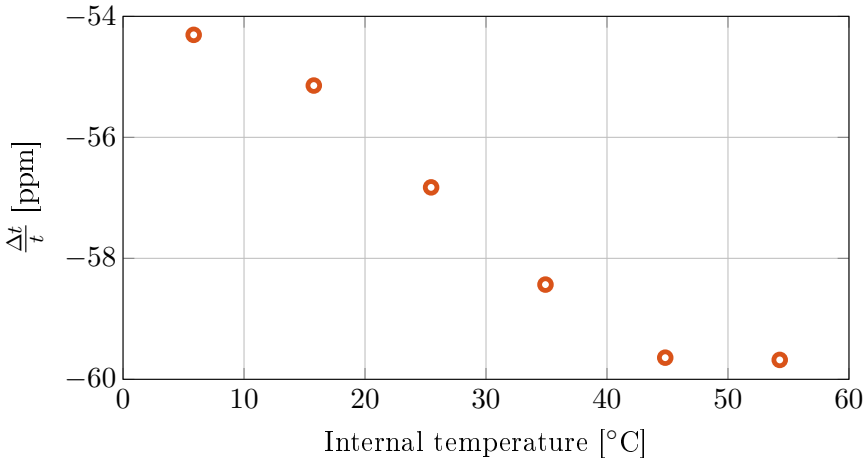

(b) Leica MS60

Figure 4-6: Drift rate of the instrument's internal time

4.4 Calibration function

Using the LSA, the calibration function was fitted to the linear regression coefficients, obtained during the climate chamber experiments. Based on the theory of crystal oscillators, a cubic calibration function was assumed. A general cubic function is of the form

$$f(x) = ax^3 + bx^2 + cx + d\,. \tag{4-1}$$

Adapting the general equation, the instrument's internal time calibration function can be expressed as

$$\frac{\Delta t}{t}(i) = a_3 T_{Int.}(i)^3 + a_2 T_{Int.}(i)^2 + a_1 T_{Int.}(i) + a_0\,, \tag{4-2}$$

where $T_{Int.}$ denotes the internal temperature of the instrument in °C, and a_3, a_2, a_1 and a_0 denote the polynomial coefficients that have to be estimated using the LSA. Please note that the following calibration functions are applicable only for the instruments used in the course of this thesis and furthermore only for the temperature range from approximately 0 to 60°C internal temperature. Using the so-defined calibration function, the calibrated time stamp of the measurement can be calculated as:

$$t_{Int.}^{calibrated}(i) = t_{Int.}^{calibrated}(i-1) + (\Delta t_{Int.}^{measured}(i) - \frac{\Delta t}{t}(i)\Delta t_{Int.}^{measured}(i))\,. \tag{4-3}$$

4.4.1 Leica TS15

The internal time calibration function for the Leica TS15 instrument is presented in Figure 4-7. As assumed, the calibration function is cubic. The 1σ prediction interval of the calibration function is the widest at the border values of the temperature range, where the function values have to be extrapolated. The largest deviations from the calibration function can be observed at 10 and 20°C. To improve the accuracy of the estimation, the climate chamber experiment at these temperatures could be repeated.

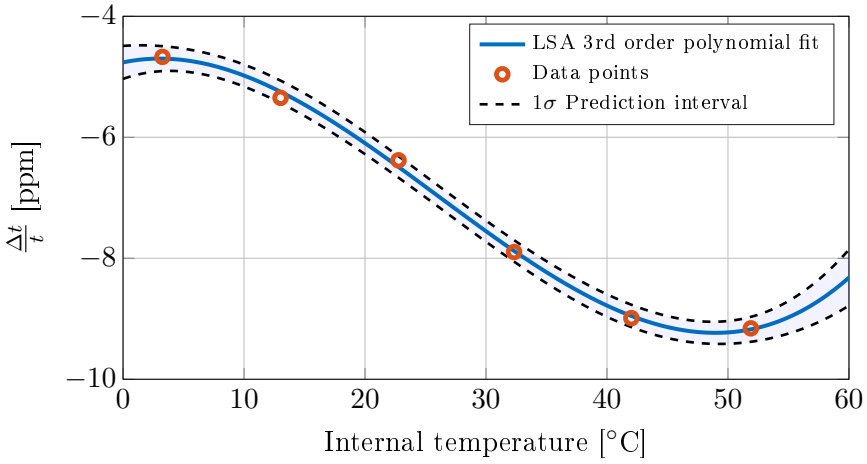

Figure 4-7: Leica TS15 internal time calibration function

Please note that the drift rate in Figure 4-7 is presented in ppm (parts per million), as it is more comprehensible. Furthermore note that using the coefficients, listed in Table 4-4 the drift rate is obtained in ppm.

Table 4-4: Coefficients of the Leica TS15 internal time calibration function

Coefficient	Value	Unit
a_0	-4.7623	1
a_1	0.0419	$^\circ\mathrm{C}^{-1}$
a_2	-0.0073	$^\circ\mathrm{C}^{-2}$
a_3	0.00009	$^\circ\mathrm{C}^{-3}$

Considering the estimated polynomial coefficients, the Leica TS15 internal time calibration function is defined as

$$\frac{\Delta t}{t} = 0.00009\, T_{Int.}^3 - 0.0073\, T_{Int.}^2 + 0.0419\, T_{Int.} - 4.7623\,. \tag{4-4}$$

4.4.2 Leica MS60

The Leica MS60 internal time calibration function is depicted in Figure 4-8. Similarly as with the Leica TS15, the 1σ prediction interval is the widest at the board values of the temperature range. In general, the prediction interval is narrower than by the Leica TS15, due to the better fit of the individual linear regression coefficients. In accordance to the theory of crystal oscillators, the Leica MS60 internal time calibration function is a cubic function.

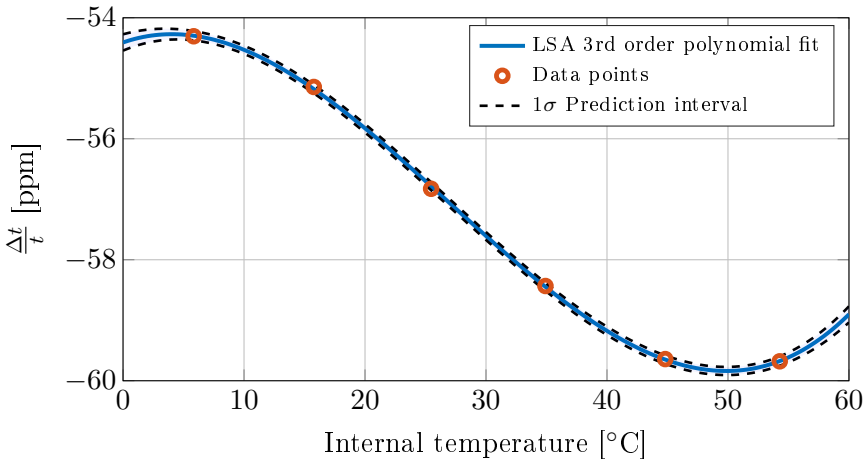

Figure 4-8: Leica MS60 internal time calibration function

Please note that the drift rate in the Figure 4-8 is again presented in ppm. Applying the coefficients listed in Table 4-5, anew leads to the drift rate in ppm.

Table 4-5: Coefficients of the Leica MS60 internal time calibration function

Coefficient	Value	Unit
a_0	-54.4086	1
a_1	0.0698	$^\circ\mathrm{C}^{-1}$
a_2	-0.0093	$^\circ\mathrm{C}^{-2}$
a_3	0.0001	$^\circ\mathrm{C}^{-3}$

Derived from Table 4-3, the Leica MS60 internal time calibration function is defined as

$$\frac{\Delta t}{t} = 0.0001\, T_{Int.}^3 - 0.0093\, T_{Int.}^2 + 0.0698\, T_{Int.} - 54.4086\,. \tag{4-5}$$

4.5 Applicability of the calibration functions at variable temperature

Instrument's internal time calibration functions, presented in Section 4.4, were obtained by fitting a cubic function to the time drift estimates at a constant temperature. In practice, the ambient temperature is variable and rapid changes can occur. Therefore the applicability of the calibration functions at variable temperature has to be investigated. As stated in Section 4.1, the used climate chamber enables programme operation mode, with programmable temperature-time ramps. Programming the temperature-time ramps, the variations of ambient temperature can be simulated. The experiments were carried out using the same hardware and software as in Section 4.3. In post-processing, the time stamps of the measurements were corrected using the corresponding internal time calibration functions (see Equations 4-4 and 4-5). The variations of the ambient temperature were selected randomly, but in a way that they cover the whole temperature range (above 0°C) of the instruments. The duration time of the experiments was selected based on the time that it takes for the climate chamber to reach individual temperatures. Previous experiments lead to an assessment that the whole temperature range can be covered in a twelve-hour experiment.

4.5.1 Leica TS15

The Leica TS15 climate chamber experiment at variable temperature was carried out on the 24.03.2016 in the office of the TU Graz geodesy building. The programmed climate chamber temperature variations are depicted in Figure 4-9a, and the results of the experiment in Figures 4-9b and 4-9c. Additionally, the results are summarized in Table 4-6.

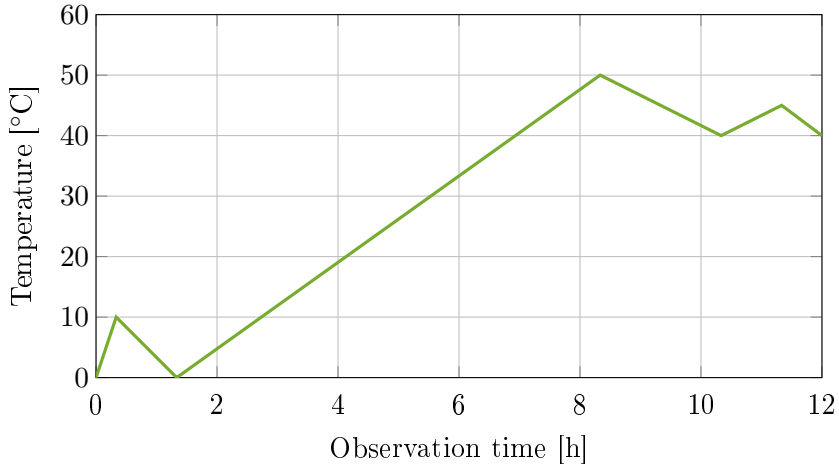

(a) Programmed climate chamber temperature-time ramp

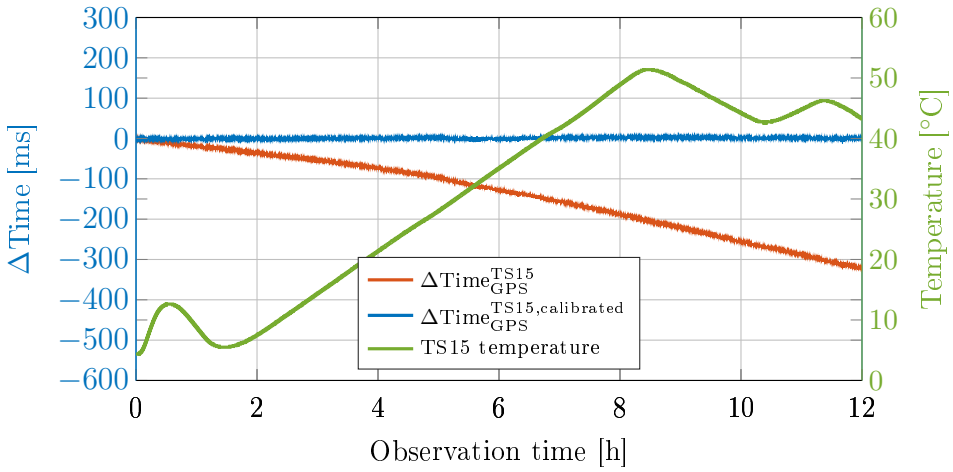

(b) Time offset of the Leica TS15 internal time and calibrated Leica TS15 internal time, to the GPS time at a variable ambient temperature

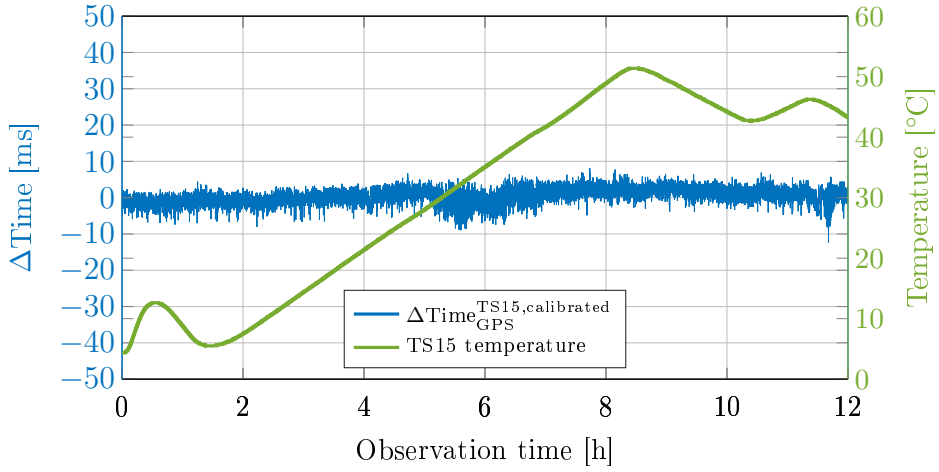

(c) Time offset of the calibrated Leica TS15 internal time, to the GPS time at a variable ambient temperature

Figure 4-9: Applicability of the Leica TS15 calibration function at a variable temperature

Figure 4-9 depicts the offsets of the instrument's internal time, before and after the application of the calibration function. The improvement of the time stability, after calibration, can be clearly seen. After the calibration, the time offset of the Leica TS15 internal time oscillates from around −5 to 5 ms (see Figure 4-9c). Even more, no remaining systematic or temperature effect can be observed.

Table 4-6: Results of the Leica TS15 climate chamber experiment at variable temperature

Source	**Duration [h]**	$\mathbf{max}(\lvert\Delta t^{GPS}_{TS15}\rvert)$ **[ms]**	$\mathbf{mean}(\lvert\Delta t^{GPS}_{TS15}\rvert)$ **[ms]**
Internal time	12	325.77	139.87
Calibrated time	12	12.33	1.61

The maximal absolute offset of the Leica TS15 calibrated internal time to GPS time during the experiment was 12.33 ms. For comparison, without the calibration the maximal absolute offset equalled 325.77 ms. Relating to Figure 4-9c, the maximal offset is represented by a single peak just before the twelve-hour mark. Otherwise, the absolute offset values lie below 10 ms and their mean value equals 1.61 ms, which is well within the aspired accuracy of the synchronization routine. Considering the duration time and the maximal absolute time offset, the time stability of the calibrated Leica TS15 equals 0.285 ppm.

4.5.2 Leica MS60

The climate chamber experiment at variable temperature was also carried out with the Leica MS60, on the 08.04.2016, again in the office of the TU Graz geodesy building. To further investigate the applicability of the calibration function at variable temperature, various experiments with different temperature-time ramps were performed. Figure 4-10 depicts the results of one of the experiments. The shape of the temperature-time ramp is depicted in Figure 4-10a, and the results of the experiment in Figures 4-10b and 4-10c. A short summary of the results is available in Table 4-7.

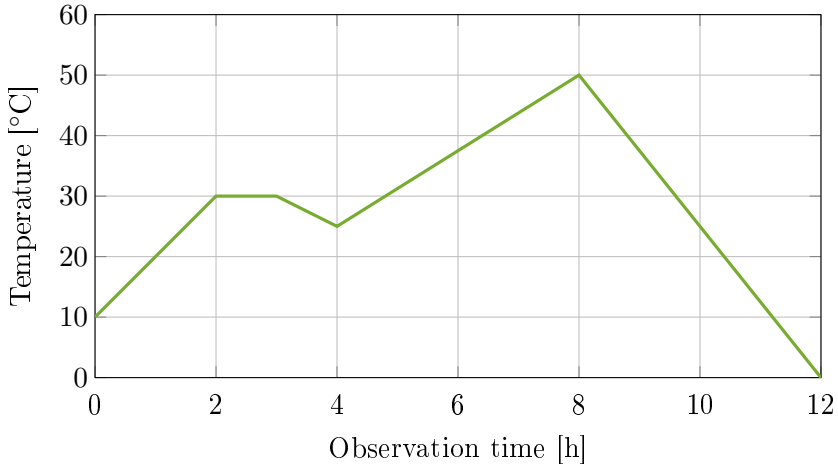

(a) Programmed climate chamber temperature-time ramp

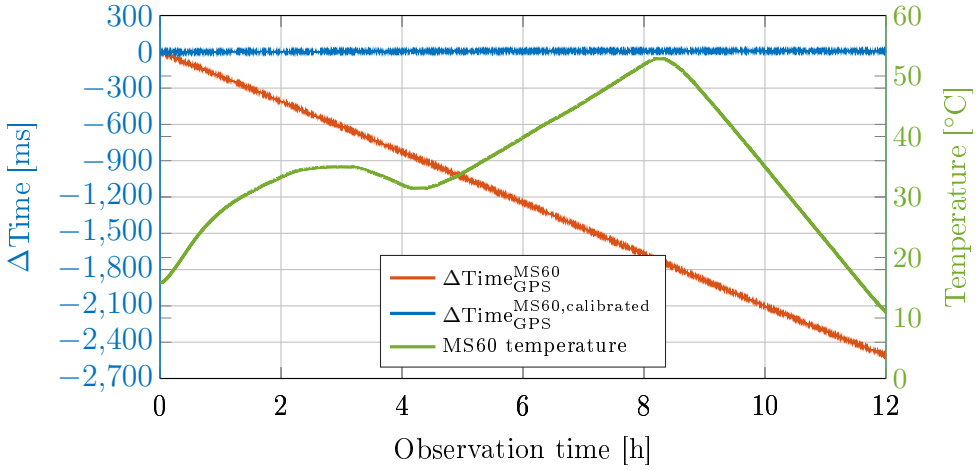

(b) Time offset of the Leica MS60 internal time and calibrated Leica MS60 internal time, to the GPS time at a variable ambient temperature

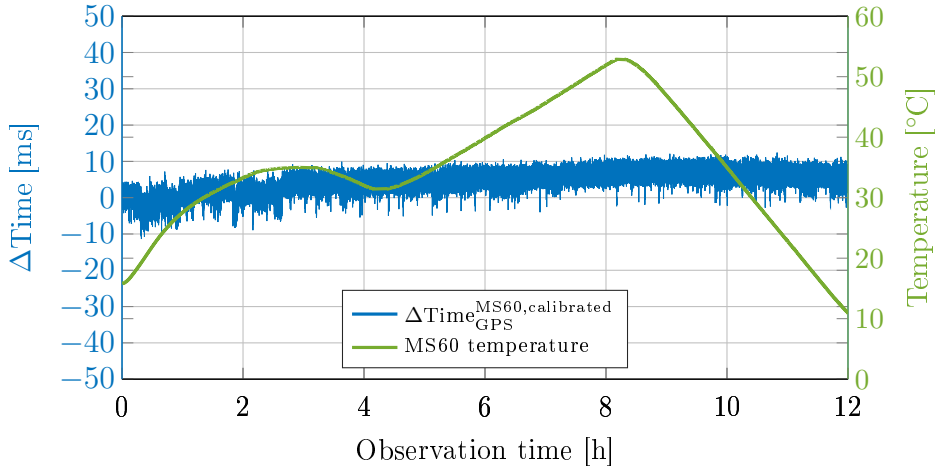

(c) Time offset of the calibrated Leica MS60 internal time, to the GPS time at a variable ambient temperature

Figure 4-10: Applicability of the Leica MS60 calibration function at a variable temperature

The experiment with the Leica MS560 offered similar results as the experiment with the Leica TS15. The drift rate of the Leica MS60 internal time is higher than the one of the Leica TS15, therefore the improvement is even more significant. Referring to Figure 4-10c, a drift can be seen in the time offset plot in the first three hours of the experiment. The exact source of the drift remains unexplained. It is unlikely to be temperature dependent, as the same temperatures occur later in the experiment, and the drift cannot be observed. Please note that in the first two hours, the temperature changes faster ($\Delta T = 10°\mathrm{C/h}$) than later in the experiment. Despite this drift, the time offset remains in the range of approximately ± 10 ms, even after twelve hour duration time.

Table 4-7: Results of the Leica MS60 climate chamber experiment at variable temperature

Source	**Duration [h]**	**max**($\left\lvert\Delta t^{\mathbf{GPS}}_{\mathbf{MS60}}\right\rvert$) **[ms]**	**mean**($\left\lvert\Delta t^{\mathbf{GPS}}_{\mathbf{MS60}}\right\rvert$) **[ms]**
Internal time	12	2512.06	1251.66
Calibrated time	12	12.43	4.64

The calibration function improves the performance of the Leica MS60 internal time from 2512.06 ms time offset, to the maximal absolute time offset of 12.43 ms, at a twelve-hour experiment at variable temperature. The mean value of the absolute time offsets after the calibration equals 4.64 ms and offers a good base to achieve the aspired accuracy of the synchronization routine. Considering the duration time and the maximal absolute time offset, the time stability of the calibrated Leica MS60 equals 0.287 ppm.

4.6 Conclusion

The proposed, four-step calibration procedure yielded applicable results for both total stations. Obtained calibration functions are applicable at a variable temperature, as can be seen in Section 4.5. The drift rate stability after calibration provides good outlook for the proposed synchronization routine. Frequency stability of both crystal oscillators, after calibration, is in accordance with the theory of the crystal oscillator temperature compensation presented in Section 3.7.1. Proposed calibration procedure can be further improved and adapted to the special use cases, as presented in Section 6. Together with the theory of cross-correlation based TDE, the calibration functions obtained during the proposed calibration procedure represent the base of the real-time synchronization routine presented in Section 5.

5 Proposed synchronization routine for real-time time synchronization of modern total stations

Referring to the total station's internal time characteristics (see Section 3) and results of the internal time calibration procedure (see Section 4) on the one hand, and considering the properties and shortcomings of the cross-correlation based TDE (see Section 2.3) on the other, a synchronization routine for real-time time synchronization of modern total stations is proposed. The proposed routine can be roughly divided into two parts:

1. TDE using cross-correlation
2. Application of the calibration function to compensate for the time drift of the instrument's internal time

In the first part of the routine, the initial time offset of the instrument's internal time is estimated and later used for correcting the time stamps of the measurements. In order to improve the correlation properties of the total station's measurements, an artificial signal (approximation of the Dirac impulse) is generated in the measurements by moving the prism, e.g. up and down. At this point, the total stations are synchronized, but they drift apart with time. To compensate for the time drift of the instrument's internal time, an internal temperature dependent calibration function is used in the second part of the routine. TDE in the first part of the routine is carried out with the internal time stamps of the measurements. Consequently, the estimation of the transfer time delay, estimation of the delay due to the internal synchronization and the estimation of the dead time of the measurements can be omitted.

To evaluate the performance of the proposed routine, the required software was developed. In the evaluation phase, the routine was carried out in post processing, but the proposal for real-time implementation is presented in Section 6. The detailed explanation of the proposed synchronization routine, and an evaluation of its performance, is available in the following sections of this thesis.

5.1 Proposed synchronization routine

Proposed synchronization routine is schematically represented in Figure 5-1.

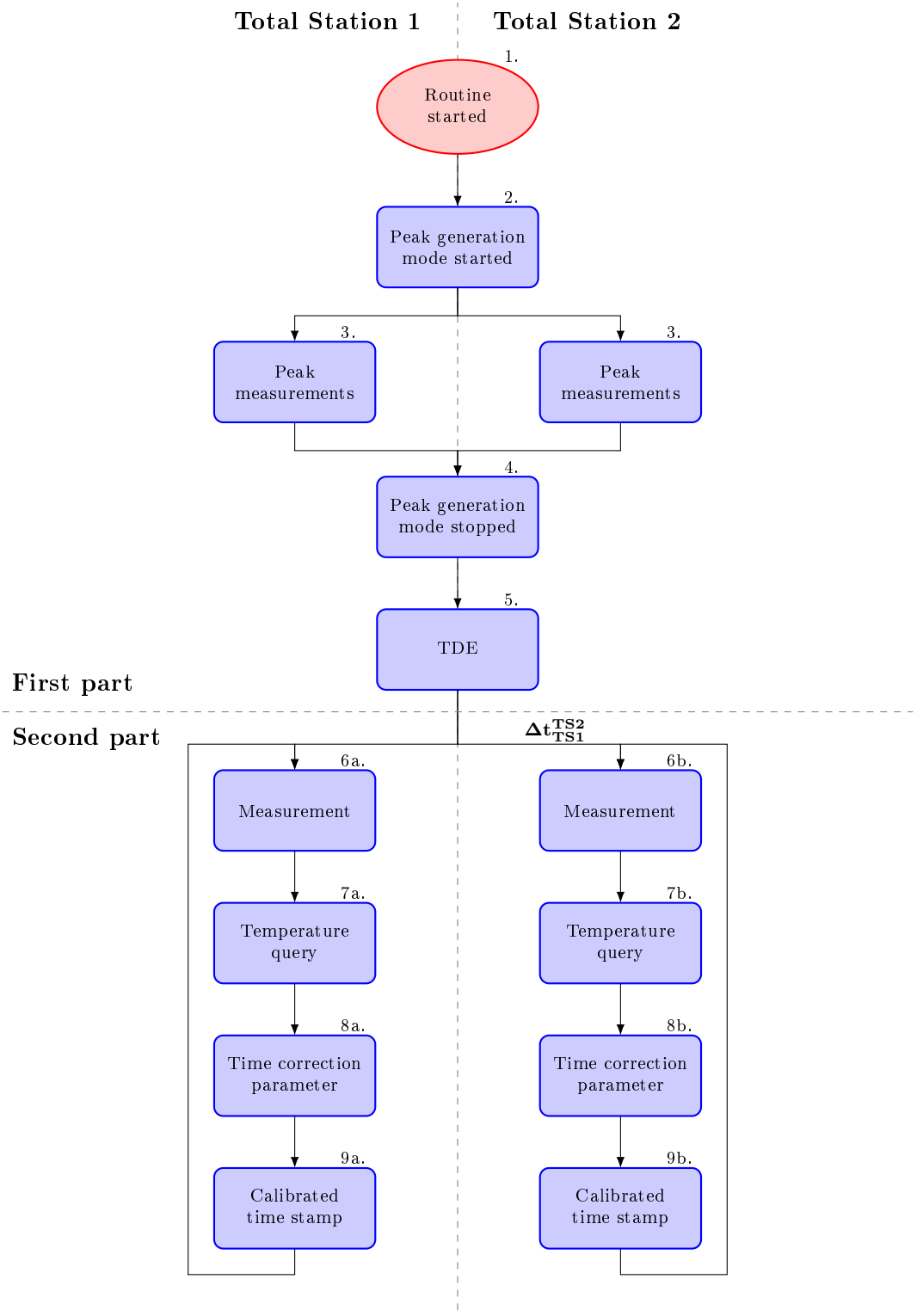

Figure 5-1: Schematic representation of the proposed synchronization routine

First part:

1. The synchronization routine is started.

2. In the peak generation mode, the total stations switch to the peak measurement mode and target the selected prism. The prism is moved, e.g. up and down in order to generate the Dirac impulse signal in the measurements. To automatize the procedure, the prism can be mounted on a linear translation stage.

3. Type of measurements performed in the peak measurement mode is instrument-dependent. The measurement type, which provides the highest sampling rate is selected, i.e. angle-only measurements (TMC_GetAngle1) by Leica TS15, and full measurements (TMC_GetFullMeas) by Leica MS60 (see Section 3.5). In the peak generation mode, the internal temperature is not queried,in order to prevent any decrease in the measurement sampling rate. Additionally, all measurements are flagged as peak measurements for later evaluation.

4. When the predefined number of measurements is reached, the peak generation mode is stopped.

5. Measurements, carried out in the peak generation mode, are resampled (based on the lower sampling rate of instruments) to satisfy the cross-correlation condition of the uniform sampling rate. Following, the time delay of the second total station to the first total station is estimated using the cross-correlation (see Section 2.3). In order to increase the resolution of the TDE, the obtained CCF is subsample interpolated using the parabola-based method (see Section 2.3.2). Obtained time offset Δt_{TS1}^{TS2}, is used to correct the following time stamps of the second total station.

Second part:

6. When the first part of the routine is completed, the normal measurement mode is started. In the normal measurement mode, the predefined type of measurement (angle-only or full measurements) is used with the individual total station.

7. Following each measurement, the internal temperature of the instrument is queried using the GeoCOM command CSV_GetIntTemp.

8. The current drift rate (time correction parameter) of the total station's internal time is obtained by inserting the internal temperature in the temperature dependent calibration function of the individual total station (see Equations 4-4 and 4-5).

9. The calibrated time stamp of the measurement performed in step 6. is calculated using Equation 4-3. The second part of the routine is repeated until either the whole routine is stopped, or another peak is generated in the data (initial time offset reset and estimated anew).

5.2 Required software and hardware

5.2.1 Multithread registration software

In order to evaluate the performance of the proposed synchronization routine, the registration software presented in Section 3.2 had to be upgraded. High sampling rate of the measurements is crucial for the accurate determination of the initial time offset. For this purpose, a multithread software in which an individual thread is allocated to each instrument (total station or GPS receiver), was developed. The multithread software enables the simultaneous communication with multiple instruments, and consequently the highest measurement sampling rates. In addition to the multithreading, a "Simulate peak for Cross-Correlation" button was introduced. Upon selecting the button, the total stations switch to peak measurement mode (no temperature queries, measurement type with highest sampling rate) and switch back to the normal mode after the predefined number of measurements, e.g. 1500 measurements are carried out. All the measurements carried out in the peak measurement mode are flagged accordingly. In the normal mode, an internal temperature is queried immediately after each measurement. The GUI of the upgraded registration software is depicted in Figure 5-2.

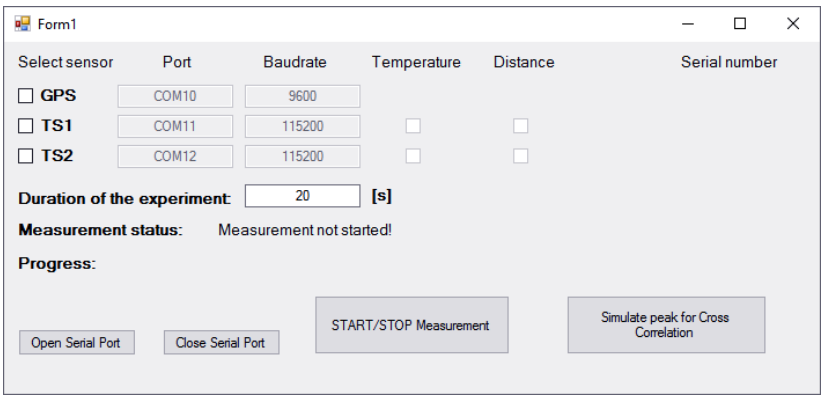

Figure 5-2: Graphical user interface of the upgraded registration software

For the initial performance investigations, the actual synchronization was done in post-processing and the registration software was only responsible for remote controlling the instruments and registration of the measurements. Upon stopping the measurements, the results were saved in a text file and prepared for later evaluation, with the synchronization software developed in MATLAB R2016a. The synchronization software follows the synchronization routine depicted in Figure 5-1.

5.2.2 Hardware

The proposed synchronization routine requires no additional hardware apart from the total stations that are to be synchronized and a computer for remote control and data processing. Even more, if done in post-processing the measurements can be recorded

directly on the total stations and the data can later be processed in the office. To fully automatize the procedure, the selected prism can be mounted on a linear translation stage. The developed software also enables the comparison of the synchronization routine with the GPS-based synchronization, for which a GPS receiver is needed. Please note that the GPS receiver is only used for comparison, and is not needed for the synchronization of the total stations, using the proposed routine.

5.3 Performance evaluation of the proposed synchronization routine

The performance of the proposed synchronization routine was evaluated in the course of two experiments carried out at the test bay on the roof of the TU Graz geodesy building. To investigate the long-term characteristics of the crystal oscillator's temperature dependency, and consequently the long-term applicability of the proposed synchronization routine, the first experiment was performed on the 10.5.2016 and the second one three months later, on the 12.8.2016. In the time, between the experiments, various other measurements were carried out with both instruments, so that the real use case from practice was simulated. In the first experiment, additionally the relation of the CPU time and the GPS time was established to ensure the independent reference for the time synchronization analysis. The duration time of the first experiment, equalled six hours, and the duration time of the second experiment was selected, based on the normal measurement duration of a one-day project (see Section 1.1), i.e. eight hours. The total stations were synchronized at the start of the experiment, using the proposed synchronization routine. Shortly before the end of the individual experiment, a second artificial peak was generated in the measurements. The performance of the synchronization routine was assessed, based on the cross-correlation based TDE at the second peak. A theoretical, error free synchronization would lead to the zero time offset. Therefore, the performance of the synchronization routine can be assessed directly, as the time offset of the total stations at the second peak. Please note that in these experiments, the actual synchronization was carried out in post-processing, but it has nevertheless followed the proposed synchronization routine. The registration of the measurements was carried out using the multithread registration software presented in Section 5.2.1. More information about the experiments is available in Sections 5.3.1 and 5.3.2.

5.3.1 First experiment

The first experiment was started on the 10.5.2016 at around 8.00 AM. The measurement configuration of the experiment is presented in Figure 5-3.

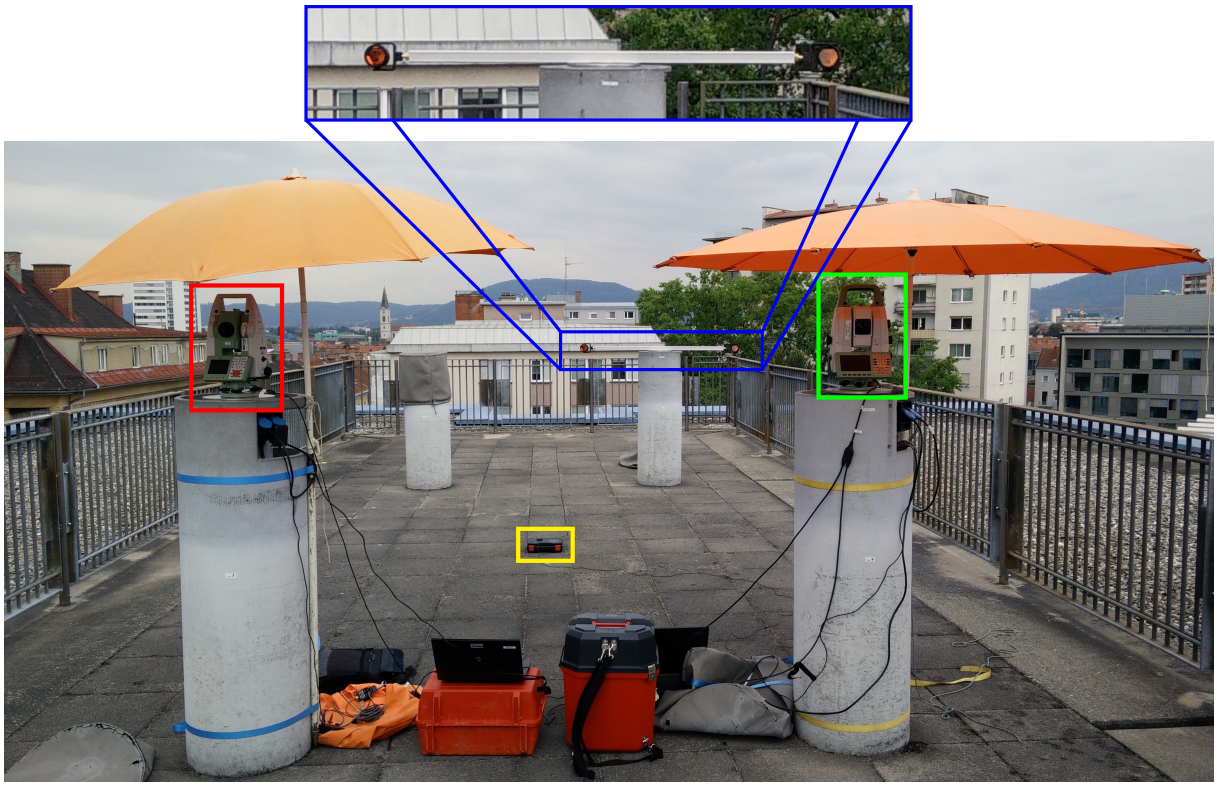

Figure 5-3: Measurement configuration of the first experiment with the proposed synchronization routine (red - Leica TS15, green - Leica MS60, blue - prisms mounted on a beam, yellow - GPS antenna)

As depicted in Figure 5-3, two prisms mounted on a beam (zoomed in, in the blue frame), were used to generate the artificial peaks in the measurements. Each instrument was locked to one of the prisms, i.e. Leica TS15 onto the left prism and Leica MS60 onto the right one. The distance between the Leica TS15 and the corresponding prism equalled 6.647 m, and the distance between the Leica MS60 and the corresponding prism equalled 6.187 m. In contrast to the previous experiments, the Leica MS60 was connected to the computer, directly, using the USB cable. The orange umbrellas, also depicted in Figure 5-3, were used to protect the instruments from rain and direct sun. In the peak generation mode, the beam with the prisms was rapidly moved up and down to generate a Dirac impulse in the vertical angle measurements (see Figure 5-4). The height difference between the start and the highest position of the prisms was approximately 55 cm.

(a) Start position of the prisms

(b) Highest position of the prisms

Figure 5-4: Generation of the artificial peak in the vertical angle measurements by moving the prisms up and down

Referring to the schematic representation of the synchronization routine in Figure 5-1, the routine consists of the normal measurement mode and the peak measurement mode. Table 5-1 depicts the GeoCOM commands, used with the individual total station in each of the modes.

Table 5-1: GeoCOM commands used by individual instrument during the experiment

Instrument	Normal measurement mode	Peak measurement mode
Leica TS15	TMC_GetFullMeas	TMC_GetAngle1
Leica MS60	TMC_GetFullMeas	TMC_GetFullMeas

In normal measurement mode both instruments performed full (angle and distance) measurements, whereas, in the peak measurement mode, Leica TS15, switched to angle-only measurements to obtain the highest possible frequency of the measurements. This is in contrast to the Leica MS60 where full measurements provide higher sampling rate than angle-only measurements (see Section 3.5). GeoCOM commands are carried out sequentially. Therefore the sampling rate of the measurements is decreased, if the temperature query is performed after each measurement (see Figure 5-5).

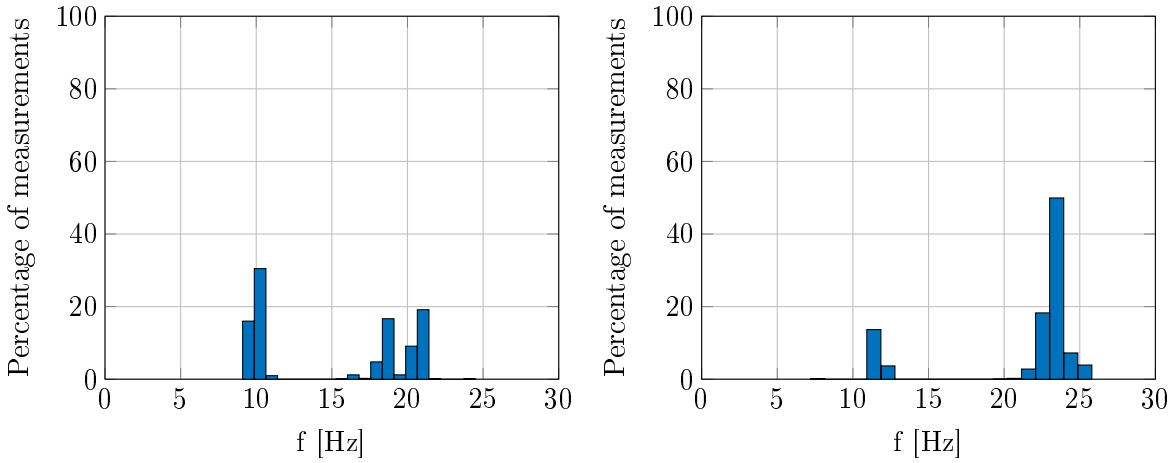

(a) Leica TS15 (b) Leica MS60

Figure 5-5: Distribution of the measurement frequency of 3000 measurements, performed using the Leica TS15 (angle only measurements) and Leica MS60 (full measurements) instruments, with temperature query after each measurement

A temperature query after each measurement is not vital for the functionality of the proposed synchronization routine. In order to obtain the highest sampling rate of the measurements, the user can reduce the rate of temperature queries, to e.g. one temperature query per minute. Temperature is than linearly interpolated for each measurement. Please note, that reducing the sampling rate of the temperature queries, can affect the performance of the proposed synchronization routine, especially if the ambient temperature is changing rapidly.

On the day of the experiment the weather was cloudy, without any major temperature changes, as can be derived from the internal temperature of the instruments, depicted in Figure 5-6. Therefore only a small part of the calibration function could be investigated.

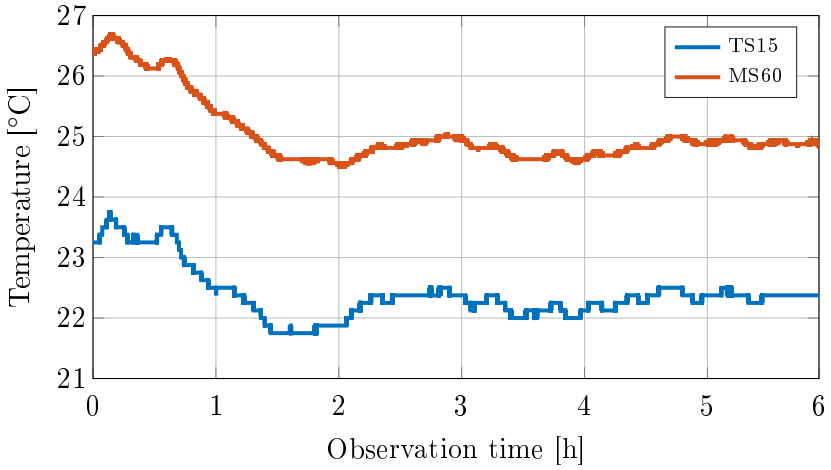

Figure 5-6: Internal temperature of the instruments, during the experiment

For the period of the peak measurement mode, in which no temperature queries are made, the internal temperature was interpolated linearly. As depicted in Figure 5-6, the internal temperature changed less than 2°C during the experiment. Vertical angle measurements performed in the peak measurement mode are depicted in Figure 5-7.

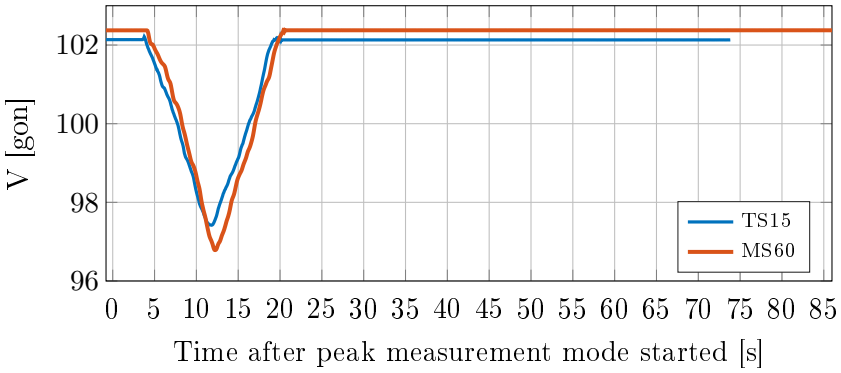

(a) First peak, generated at the start of the measurement

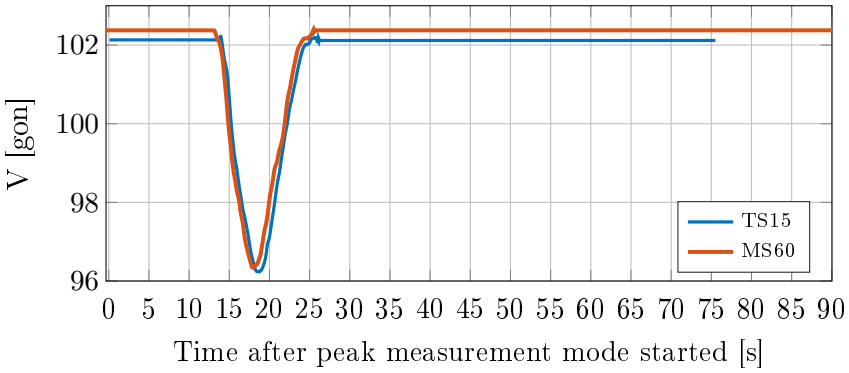

(b) Second peak, generated at the end of the measurement

Figure 5-7: Vertical angle measurements of the generated peaks, used for cross-correlation based TDE

Figure 5-7 depicts uncalibrated time stamps of the measurements. Thus it can be seen that the first peak occurs earlier in the Leica TS15 internal time than in the Leica MS60 internal time (see Figure 5-7a). Due to the higher drift rate of the Leica MS60, the exact opposite can be observed at the second peak (see Figure 5-7b). The results of the synchronization routine are depicted in Figure 5-8 and a short summary is available in Table 5-2.

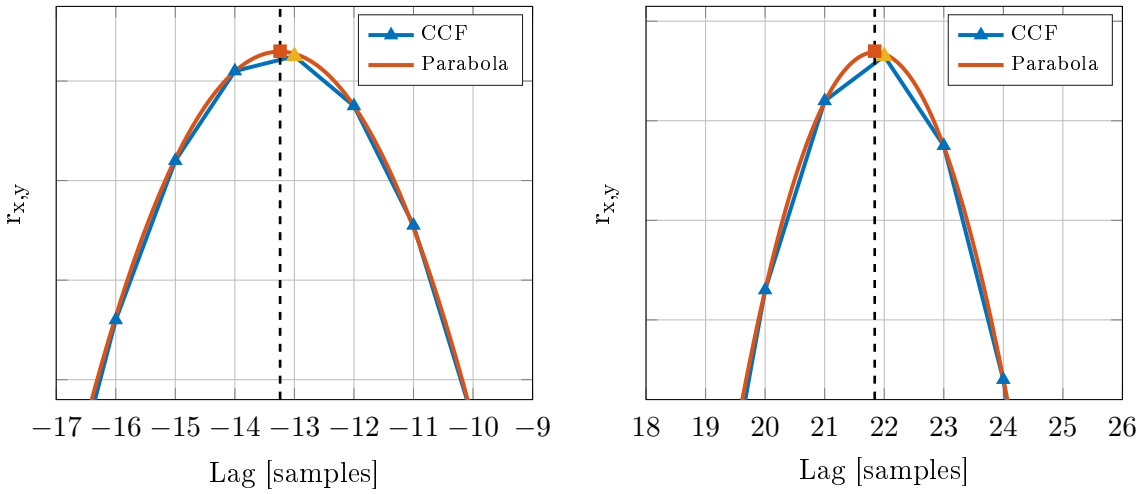

(a) Uncalibrated internal time (left - first peak, right - second peak)

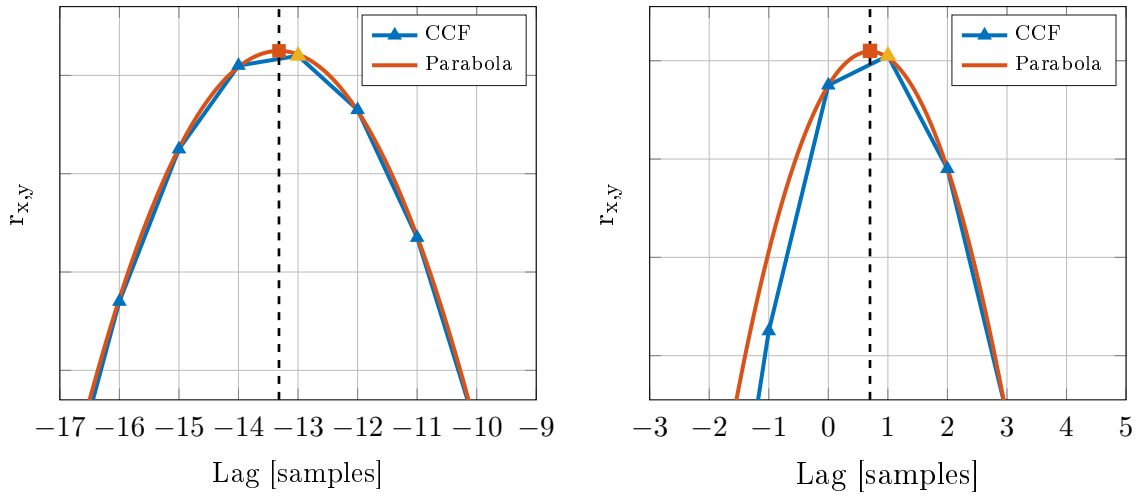

(b) Calibrated internal time (left - first peak, right - second peak)

Figure 5-8: CCF of vertical angle measurements, with the parabola-based supsample interpolation (one sample equals 50 ms). Orange triangle depicts the maximal correlation coefficient and the red square represents the maximum of the parabola function

Please note that the time lag in Figure 5-8 is given in samples. The samples can be converted to milliseconds, using the sampling rate, to which the measurements were resampled before the cross-correlation, i.e. 50 ms. Furthermore please note that in the TDE at the second peak, the time offset of the instrument at the first peak is already considered. Therefore, considering error free synchronization, the time offset at second peak should equal 0 ms.

Table 5-2: Results of the time synchronization routine for the first experiment

Source	$\Delta t^{TS2}_{TS1,\text{first peak}}$ [ms]	$\Delta t^{TS2}_{TS1,\text{second peak}}$ [ms]
Uncalibrated internal time	−662.0	1093.3
Calibrated internal time	−665.7	36.0

Table 5-2 depicts the results of the TDE obtained with the parabola-based subsample interpolation. Using the proposed synchronization routine, the time offset at the second peak equals 36 ms, which represents a big improvement in comparison with the 1093.3 ms time offset using only cross-correlation based time synchronization, without the internal time calibration function. Considering the duration time of the experiment, the synchronization error obtained, using the proposed synchronization routine equals 1.67 ppm. Results of the time synchronization can also be observed at the synchronized vertical angle measurements of the peaks, depicted in Figure 5-9.

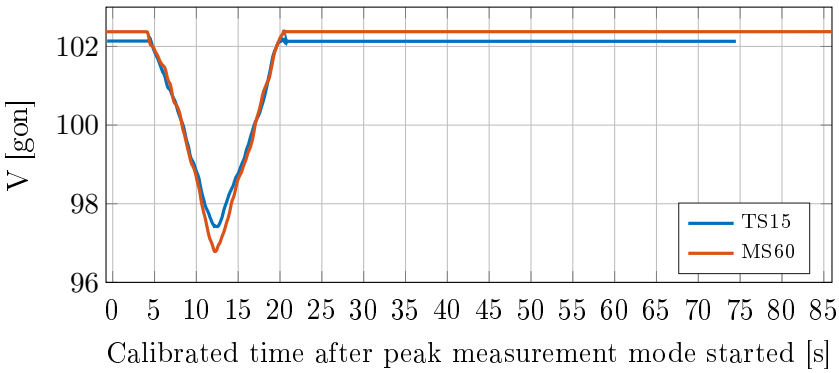

(a) First peak, generated at the start of the measurement

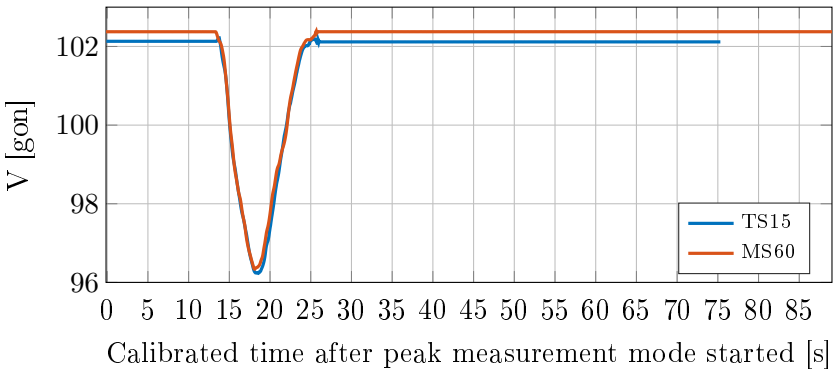

(b) Second peak, generated at the end of the measurement

Figure 5-9: Synchronized vertical angle measurements of the generated peaks

The first experiment also highlighted some areas for possible improvement. Considering Figure 5-7, the drawback of using two prisms mounted on a beam, can be seen. Not only did one prism reach its highest point slower than the other, it was also lifted higher, as a consequence of an insufficient synchronization of the movement. Additionally, considering Figures 5-8b and 5-8a, it can be observed that due to the slow velocity of the prism movement in the first peak generation mode, the peak of the CCF is flat, which hinders the peak detection and can lead to false time delay estimates.

In the first experiment, a GPS receiver was used additionally to establish an independent reference. PPS events were recorded separately in an individual thread of the multithread registration software. The GPS receiver was functioning without a problem only for the first 100 minutes of the experiment, after that point the receiver continuously lost fix, and consequently the PPS events were not sent. Therefore, the comparison of the results of the proposed synchronization routine to GPS time, was made only for the first 100 minutes in which the difference between the GPS time and the synchronized time of the total stations, equalled 1.5 ms. Based on this result, the further development of the proposed synchronization routine from the relative to the absolute synchronization is possible.

5.3.2 Second experiment

Based on the results of the first experiment, improvements were introduced for the second experiment. The experiment was started on the 12.8.2016 (approximately three months after the first experiment) at around 8.30 AM. The modified measurement configuration is depicted in Figure 5-10.

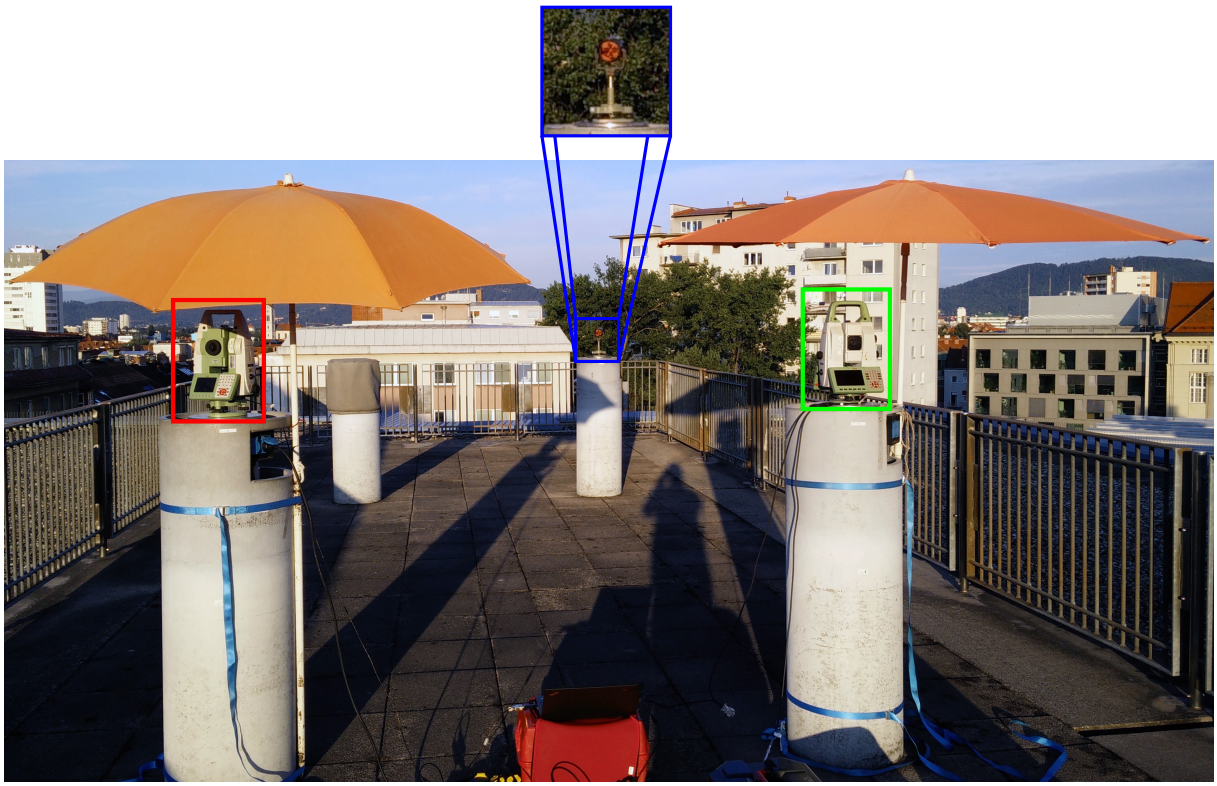

Figure 5-10: Measurement configuration of the second experiment with the proposed synchronization routine (red - Leica TS15, green - Leica MS60, blue - prism)

As depicted in Figure 5-10, in the second experiment only one prism was used for the generation of the artificial peak in the vertical angle measurements (see Figure 5-11). Both total stations were locked onto the same prism. The distance between the Leica TS15 and the prism equalled 6.727 m, and the distance between the Leica MS60 and the prism equalled 6.206 m. It should be pointed out that such configuration (with only one prism) was tested beforehand. The possibility of direct reflections of the ATR or EDM signal from the front surface of the prism has to be taken into consideration, especially at small angles of incidence. According to Lackner and Lienhart (2016, p. 5), measurements to the used circular prism Leica GPR121 are not affected by the reflections from the front surface, due to the anti-reflex coating of the prism. For more information about how the front reflections affect measurements, please refer to Lackner and Lienhart (2016).

(a) Start position of the prism (b) Highest position of the prism

Figure 5-11: Generation of the artificial peak in the vertical angle measurements, by moving the prism up and down

In the second experiment, the height difference between the start and the highest position of the prism was smaller - it equalled approximately 42 cm. The type of measurements performed in the normal and in the peak measurement mode was kept the same as during the first experiment (see Table 5-1).

On the day of the second experiment, the weather conditions were more suitable for this kind of experiment. The ambient temperature in the morning was lower (around 18°C) but it rose as the day progressed (around 26°C at 1.00 PM). The internal temperature of the total stations is depicted in Figure 5-12.

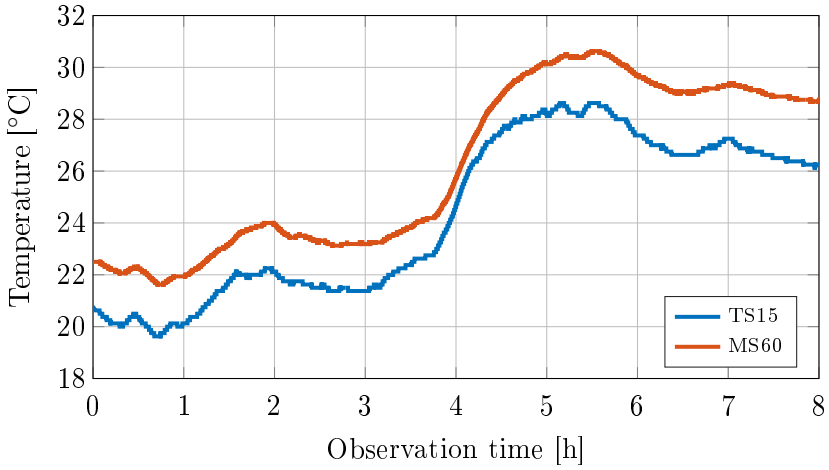

Figure 5-12: Internal temperature of the instruments, during the experiment

Apart from using only one prism, another improvement was introduced in the second experiment. Due to the flat peak of the CCF at the first peak in the first experiment, an attempt to increase the velocity of the movement, and to make the peak duration shorter, was made. Vertical angle measurements performed in the peak measurement mode of the second experiment are depicted in Figure 5-13.

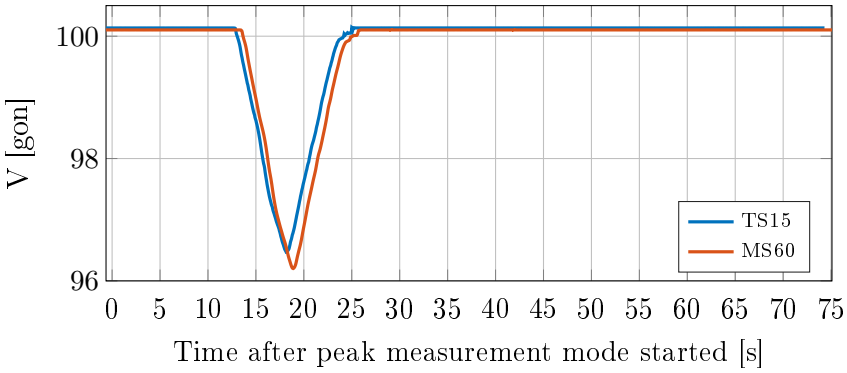

(a) First peak, generated at the start of the measurement

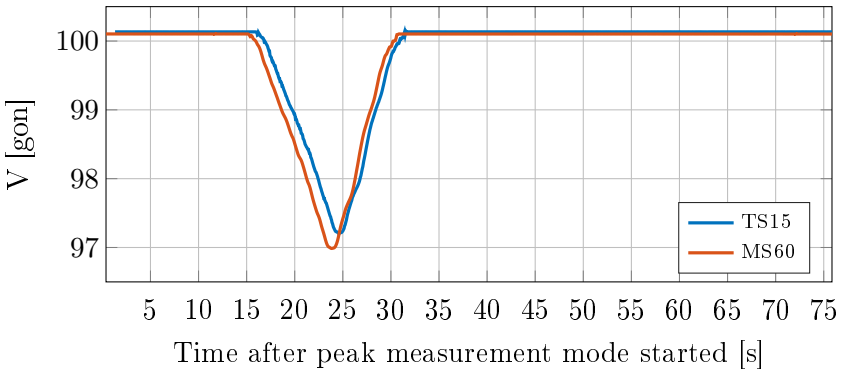

(b) Second peak, generated at the end of the measurement

Figure 5-13: Vertical angle measurements of the generated peaks, used for cross-correlation based TDE

Figure 5-13, depicts measurements with the uncalibrated time stamps. Therefore, it can again be seen that the peaks do not occur at the same time point, measured with Leica TS15 and Leica MS60 internal time. Results of the cross-correlation based TDE estimation, for the second experiment, are presented in Figure 5-14.

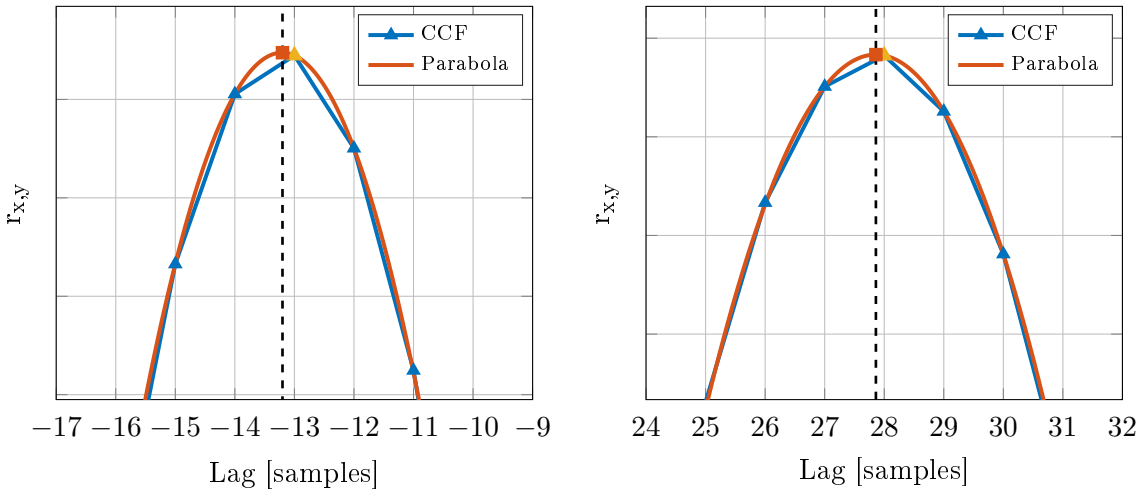

(a) Uncalibrated internal time (left - first peak, right - second peak)

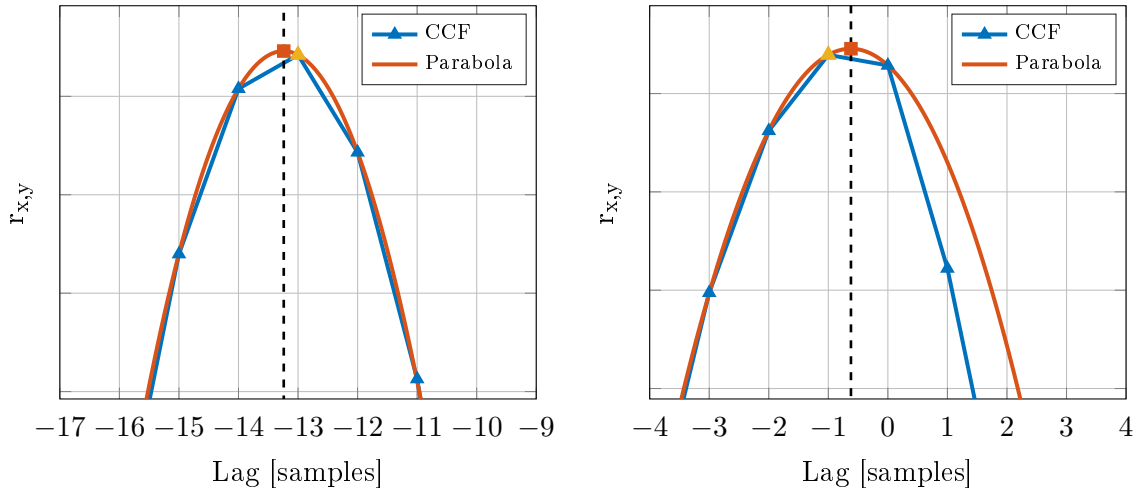

(b) Calibrated internal time (left - first peak, right - second peak)

Figure 5-14: CCF of vertical angle measurements, with the parabola-based supsample interpolation (one sample equals 50 ms). Orange triangle depicts the maximal correlation coefficient and the red square represents the maximum of the parabola function

The time lag in Figure 5-14 is again given in samples, and can be converted to milliseconds, using the sampling rate to which the measurements were respampled before the cross-correlation, i.e. 50 ms. Observing the first peak, generated in the measurements, it can be seen that the higher velocity of the movement results in a much sharper peak of the CCF. At the second peak, the movement was again too slow and as a result a flatter peak of the CCF can be observed. Please note that when determining the time lag at the second peak, the time lag at the first peak was already considered. A short summary of the results is depicted in Table 5-3.

Table 5-3: Results of the time synchronization routine for the second experiment

Source	$\Delta t^{TS2}_{TS1,\text{first peak}}$ [ms]	$\Delta t^{TS2}_{TS1,\text{second peak}}$ [ms]
Uncalibrated internal time	−660.0	1393.0
Calibrated internal time	−661.7	−30.7

Table 5-3 depicts the results of the cross-correlation based TDE obtained by the parabola-based subsample interpolation. Without using the calibration function, the time offset of the total stations internal time equalled 1393.0 ms after eight hours, whereas, using the proposed synchronization routine the time offset equalled only −30.7 ms. This represents the improvement of the synchronization error from 48.37 ppm to 1.07 ppm. The synchronized vertical angle measurements, performed in the peak measurement mode are depicted in Figure 5-15.

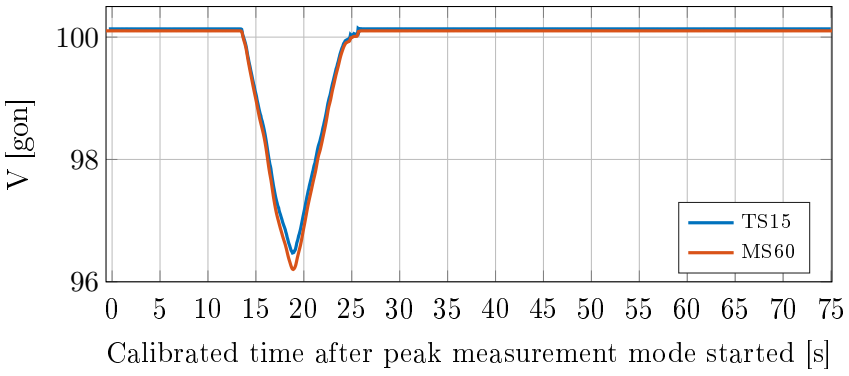

(a) First peak, generated at the start of the measurement

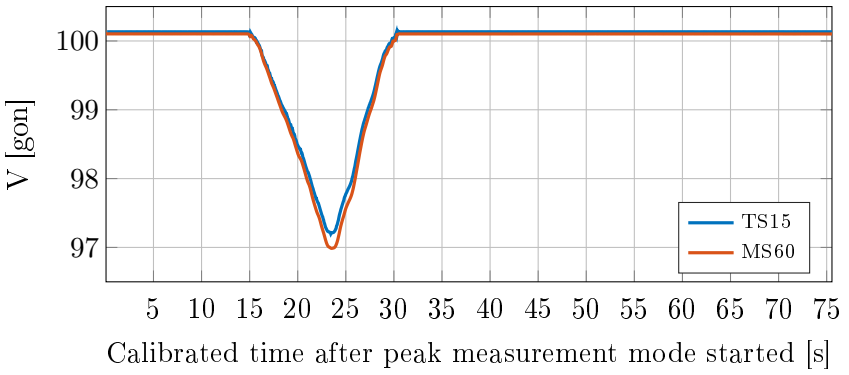

(b) Second peak, generated at the end of the measurement

Figure 5-15: Synchronized vertical angle measurements of the generated peaks

Using only one prism for the peak generation has proved to be beneficial, and the results obtained in the second experiment with the proposed synchronization routine are even superior, and well within the goals stated for this thesis. Referring to Figure 5-15b, the generated peaks are concurrent in the synchronized vertical angle measurements. Possible further improvements of the proposed synchronization routine are discussed in Section 6.

6 Conclusion and outlook

In this thesis, a synchronization routine for real-time synchronization of modern total stations is proposed (see Section 5). As an essential part of the proposed synchronization routine, also a calibration procedure for calibration of the total station's internal time is proposed (see Section 4). The proposed routine fulfils the requirements, listed in Section 1.1, i.e. synchronization using the proposed synchronization routine is independent of the ambient conditions and requires no additional hardware. As part of the development, an in-depth investigation of the total station's internal time was performed (see Section 3). The investigation highlighted some of the total station's characteristics, which need to be considered when synchronizing two total stations, e.g. dead time of the measurements, internal synchronization of the measurements and the sampling rate of different measurement types.

The proposed synchronization routine consists of a cross-correlation based TDE and a calibration function, obtained in the proposed calibration procedure, used to compensate the temperature effect on the internal time. In order to improve the correlation properties of the measurements, a Dirac impulse was generated in vertical angle measurements, by moving the dedicated prism up and down. The performance of the routine was tested in two experiments at a variable temperature. Using the proposed synchronization routine, the synchronization error in the first experiment was improved from 1093.3 ms (50.6 ppm) to 36.0 ms (1.67 ppm) after eight hours. In the second experiment, the proposed synchronization routine yielded a synchronization error of -30.7 ms after eight hours (1.07 ppm), whereas, without the proposed synchronization routine, the synchronization error equalled 1393.0 ms after eight hours (48.37 ppm). The second experiment was carried out approximately three months after the first experiment, to test the long-term applicability of the proposed synchronization routine. In both experiments, the aspired accuracy of 1.75 ppm (lower than sampling rate, after eight hours) was achieved.

In both experiments at variable temperature, the synchronization was carried out in post-processing. Nevertheless, the proposed routine can be implemented so that it enables real-time synchronization. As the calibration function is determined beforehand in a calibration procedure, the time correction parameter can be calculated in real-time, using the previous internal temperature query. Here the user can decide, how often an internal temperature is queried (trade-off between the sampling rate and the synchronization performance). Thus, only the TDE would be left at the start of the measurements, which can be carried out right after the peak measurement mode, using flagged measurements as input parameters.

Experiments, carried out with the proposed synchronization routine, highlighted some areas of possible improvement. The whole procedure could be automatized using a prism, mounted on a linear translation stage for the generation of a Dirac impulse in the measurements. This would not only automatize the procedure, it would also enable the full control of the movement (velocity), which would result in a sharper peak of the CCF, and would consequently improve the TDE. The proposed routine could also be adapted to the special use cases, in which the ambient temperature is known beforehand. The calibration procedure could than be optimized for this narrower temperature range, and consequently, smaller temperature steps could be used in the proposed calibration procedure, which would improve the calibration function estimation. Furthermore, based on the initial experiments, the performance of the proposed calibration routine could be assessed and a threshold, which would reset the synchronization, could be introduced. This would lead to a synchronization of two total stations, within the predefined threshold, over a longer period of time.

The proposed routine was developed using Leica instruments, but the basic idea could be adapted to any modern RTS, which enables remote control, returns time stamps of the measurements and allows queries of the internal temperature.

References

Amos S. W., Amos R. S. (2002): Newnes Dictionary of Electronics, Fourth edition. Newnes, Oxford, England. 389p.

Arvind K. (1994): Probabilistic Clock Synchronization in Distributed Systems. IEEE Transaction on Parallel and Distributed Systems vol. 5, no. 5. pp. 474-487.

Benesty J., Chen J. (2004): Time-Delay Estimation via Linear Interpolation and Cross Correlation. IEEE Transaction on Speech and Audio Processing vol. 12, no. 5. pp. 509-519.

Cerda R. M. (2005): Understanding TCXOs. `http://www.crystek.com/documents/appnotes/Understanding_TCXOs.pdf` [Accessed 30.5.2016].

Cristian F. (1989): Probabilistic clock synchronization. Distributed Computing vol. 3. pp. 146-158.

El-Rabbany A. (2002): Introduction to GPS: The Global Positioning System. Artech House, Boston, MA, USA. 176p.

Elson J.E. (2003): Time Synchronization in Wireless Sensor Networks. PhD thesis, Computer Science Department, University of California. 203p.

Frerking M. E. (1978): Crystal Oscillator Design and Temperature Compensation. Van Nostrand Reinhold, New York, NY, USA. 240p.

Hewlett-Packard (1997): Fundamentals of Quartz Oscillators - Application Note 200-2. Hewlett Packard Company, Palo Alto, CA, USA. 28p.

Hofmann-Wellenhof B., Lichtenegger H., Collins J. (1997): Global Positioning System: Theory and Practice, Fourth edition. Springer Verlag, Vienna, Austria. 389p.

ICD GPS (2012): Navstar GPS Space Segment/Navigation User Interfaces. IS-GPS-200G 207p.

ISA (2003): The Automation, Systems, and Instrumentation Dictionary, Fourth edition. ISA, Durham, NC, USA. 582p.

Joeckel R., Stober M., Huep W. (2008): Elektronische Entfernungs- und Richtungsmessung und ihre Integration in aktuelle Positionierungsverfahren vol. 5. Wichmann, Heidelberg, Germany. 526p.

Kirschner H., Stempfhuber W. (2008): The Kinematic Potential of Modern Tracking Total Stations - A State of the Art Report on the Leica TPS1200+. Proc. 1st International Conference on Machine Control & Guidance pp. 51-60.

Knapp C. H., Carter G. C. (1976): The Generalized Correlation Method for Estimation of Time Delay. IEEE Transaction on Acoustics, Speech and Signal Processing vol. ASSP-24, no. 4. pp. 320-327.

Kopetz H., Ochsenreiter W. (1987): Clock Synchronization in Distributed Real-Time Systems. IEEE Transaction on Computer vol. 36, no. 8. pp. 933-940.

Lackner S., Lienhart W. (2016): Impact of Prism Type and Prism Orientation on the Accuracy of Automated Total Station Measurements. Proc. Joint International Symposium on Deformation Monitoring (JISDM), Vienna, Austria. 8p.

Leica (2010): Leica TS11/TS15 GeoCOM Reference Manual ver. 2.0. Leica Geosystems, Heerbrugg, Switzerland. 223p.

Leica (2011): Leica TS11/TS15 User Manual ver. 2.0. Leica Geosystems, Heerbrugg, Switzerland. 220p.

Leica (2015): Leica MS60/TS60 User Manual ver. 1.0. Leica Geosystems, Heerbrugg, Switzerland. 90p.

Lewandowski W., Thomas C. (1991): GPS Time Transfer. Proc. IEEE vol. 79, no. 7. pp. 991-1000.

Lienhart W. (2013): Deformationsmessungen eines Erddammes mit faseroptischen Sensoren. Proc. 3. Tagung Messtechnik, Vienna, Austria. pp. 83-87.

Lienhart W. (2015): Totalstationen für Deformationsmessungen. GeoNews vol. 1. pp. 6-7.

Lienhart W., Lackner S., Moser M., Woschitz H., Supp G. (2013a): Deformation Monitoring of Flood Prevention Dams using Geodetic and Fibre Optic Measurement Techniques. Proc. 6th Int. Conference on Structural Health Monitoring of Intelligent Infrastructure (SHMII-6), Hong Kong, China. 8p.

Lienhart W., Lackner S., Supp G., Marte R. (2013b): Evaluation of State of the Art Methods for Surface Monitoring of Earth Filled Dams. Proc. 2nd Joint International Symposium on Deformation Monitoring (JISDM), Nottingham, UK. 8p.

Lienhart W., Ehrhart M., M.Grick (2016): High Frequent Total Station Measurements for the Monitoring of Bridge Vibrations. Proc. Joint International Symposium on Deformation Monitoring (JISDM), Vienna, Austria. 8p.

Memmert (2011): Operating incstructions ICP400. Memmert GmbH, Schwabach, Germany. 47p.

Montgomery D. C., Jennings C. L., Kulahci M. (2008): Introduction to Time Series Analysis and Forecasting. John Wiley & Sons. Inc., Hoboken, NJ, USA. 445p.

MSDN (2016): QueryPerformanceCounter function. https://msdn.microsoft.com/en-us/library/windows/desktop/ms644904(v=vs.85).aspx [Accessed 19.7.2016].

Mumford P.J. (2003): Relative timing characteristics of the one pulse per second (1PPS) output pulse of three GPS receivers. Paper presented at the 6th International Symposium on Satellite Navigation Technology Including Mobile Positioning & Location Services. 10p.

NMEA (2016): NMEA 0183 standard. http://www.nmea.org/ [Accessed 2.6.2016].

Pikovsky A., Rosenblum M., Kurths J. (2001): Synchronization: A Universal Concept in Nonlinear Sciences. Cambridge University Press, Cambridge, United Kingdom. 411p.

Rüeger J. M. (2006): 75 years of change in survey technology. Survey Review vol. 38, no. 300. pp. 459-473.

Stempfhuber W. (2001): System Calibration in Precise Farming. In: Grün/Kahmen (Eds), Optical 3-D Measurement Techniques V, Vienna, FIG Commission 5 and 6, IAG Special Commission 4, ISPRS Commission 5. pp. 366-376.

Stempfhuber W. (2009): Verification of the Trimble Universal Total Station (UTS) Performance for Kinematic Applications. In: Grün/Kahmen (Eds), Optical 3-D Measurement Techniques IX, Vienna, FIG Commission 5 and 6, IAG Special Commission 4, ISPRS Commission 5. pp. 211-221.

Stempfhuber W., Wunderlich T. (2004): Auf dem Weg zur Sensorsynchronisation von GPS und TPS für kinematische Messaufgaben. Allgemeine Vermessungs-Nachrichten 5/2004. pp. 175-184.

Stempfhuber W.V. (2004): Ein integritätswahrendes Messsystem für kinematische Anwendungen. PhD thesis, Institut für Geodäsie, GIS und Landmanagement, TU Munich, Germany. 131p.

u-blox (2011): GPS-based Timing: Considerations with u-blox 6 GPS receivers. u-blox AG, Thalwil, Switzerland. 14p.

u-blox (2014): LEA-6: u-blox 6 GPS Modules. u-blox AG, Thalwil, Switzerland. 26p.

U.S.C.G. Navigation Center (2016): GPS CONSTELLATION STATUS FOR 05/30/2016. http://www.navcen.uscg.gov/index.php?Do=constellationStatus&srt=PRN&dir=Desc [Accessed 30.5.2016].

Wei W. W. S. (2006): Time Series Analysis: Univariate and Multivariate Methods, Second edition. Pearson Addison Wesley, Boston, MA, USA. 613p.

Wiens T., Bradley S. (2008): A Comparison of Time Delay Estimation Methods for Periodic Signals. http://www.nutaksas.com/papers/wiens_dsp_delay.pdf [Accessed 30.5.2016].

Witchayangkoon B. (2000): Elements of GPS Precise Point Positioning. PhD thesis, Spatial Information Science and Engineering, University of Maine, USA. 265p.

Zhang L., Wu X. (2006): On the application of cross correlation function to subsample discrete time delay estimation. Digital Signal Processing vol. 16, no. 6. pp. 682-694.

Appendix A Results of the Climate chamber test

A.1 Leica TS15

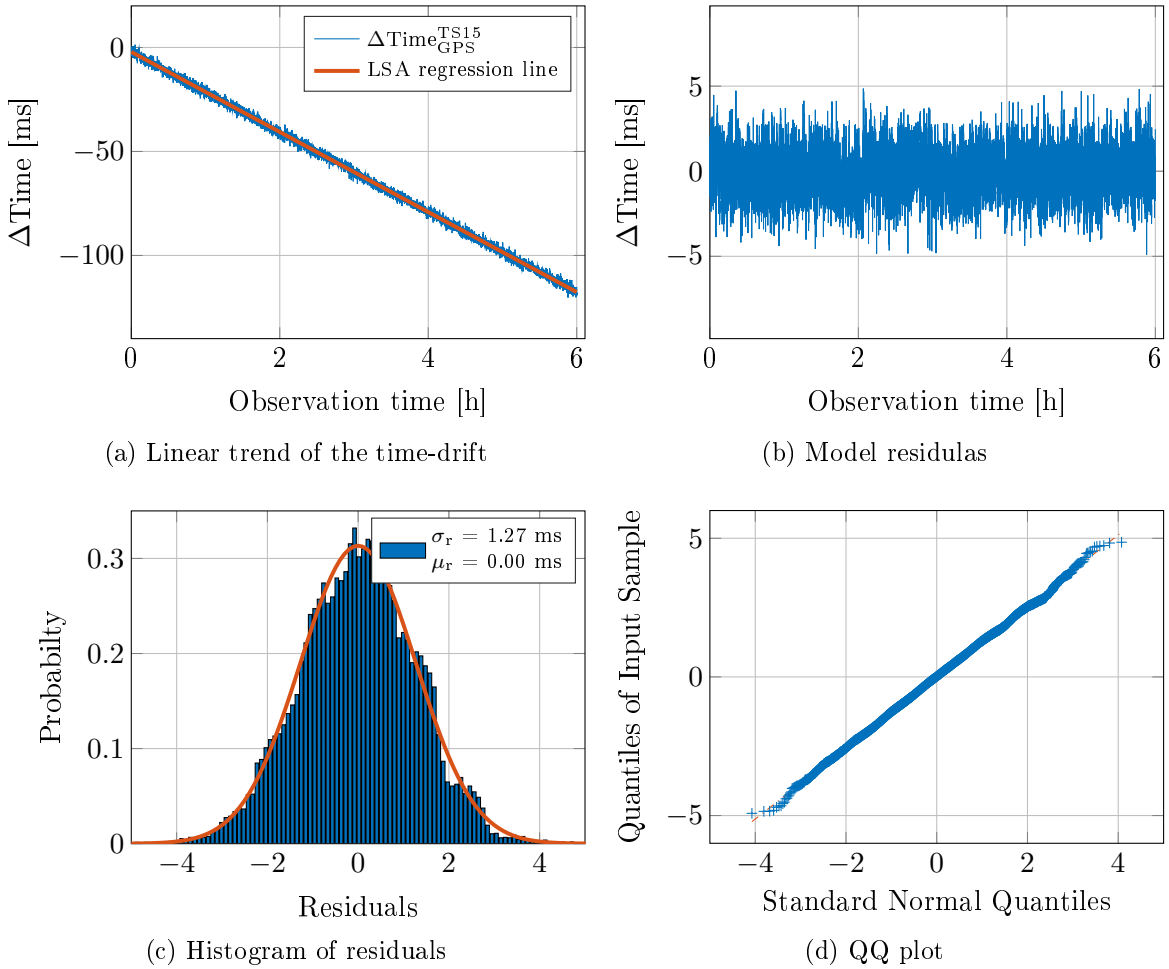

(a) Linear trend of the time-drift

(b) Model residulas

(c) Histogram of residuals

(d) QQ plot

Figure A.1: Results of the Leica TS15 climate chamber experiment at 10°C ambient temperature

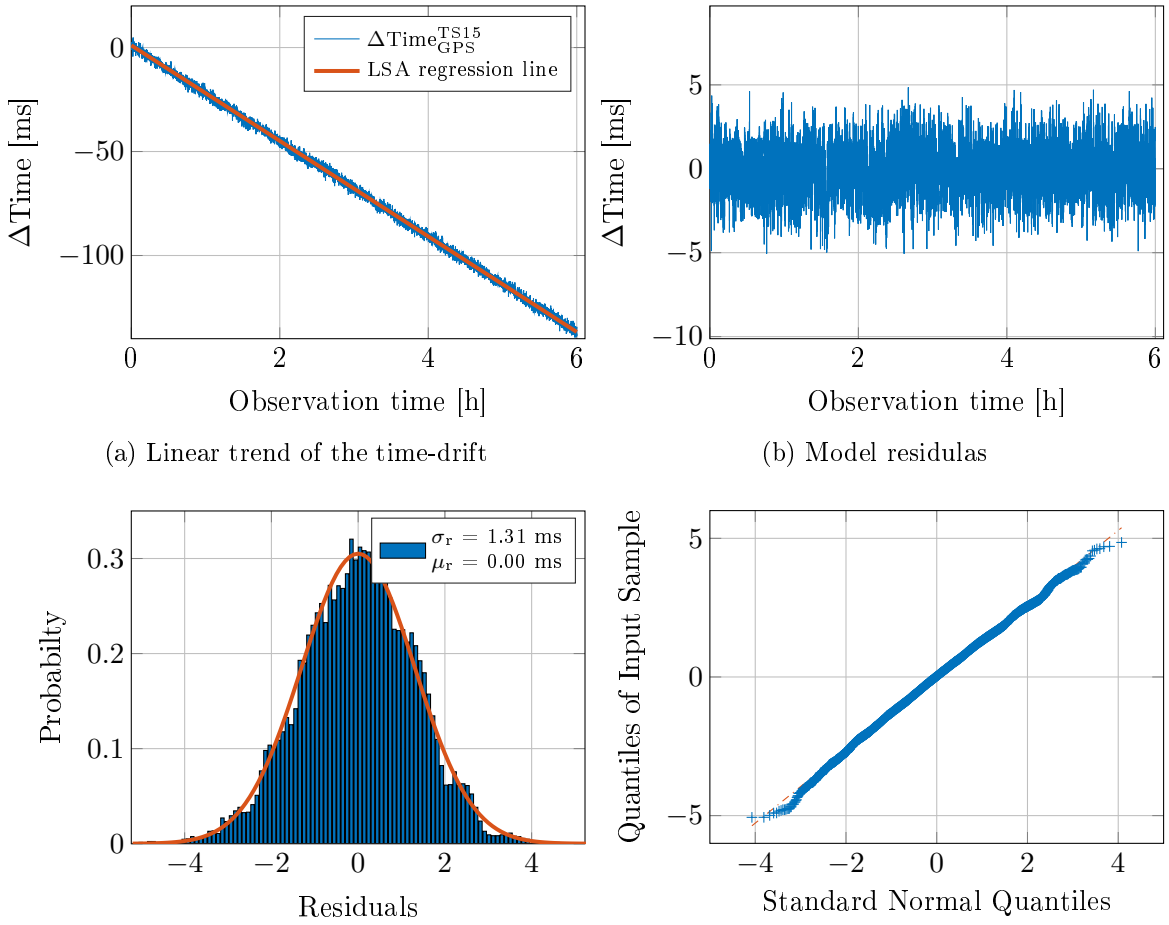

(a) Linear trend of the time-drift

(b) Model residulas

(c) Histogram of residuals

(d) QQ plot

Figure A.2: Results of the Leica TS15 climate chamber experiment at 20°C ambient temperature

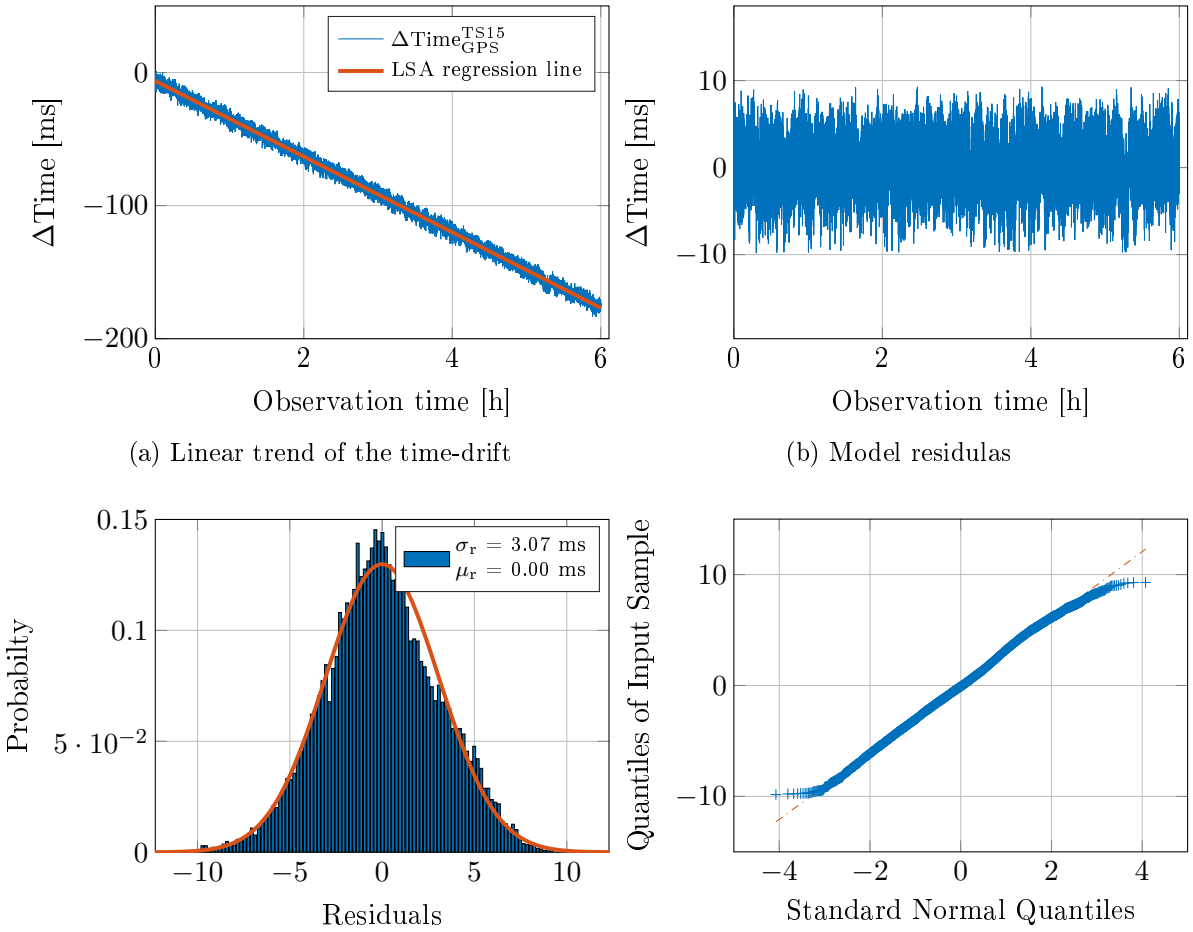

(a) Linear trend of the time-drift

(b) Model residulas

(c) Histogram of residuals

(d) QQ plot

Figure A.3: Results of the Leica TS15 climate chamber experiment at 30°C ambient temperature

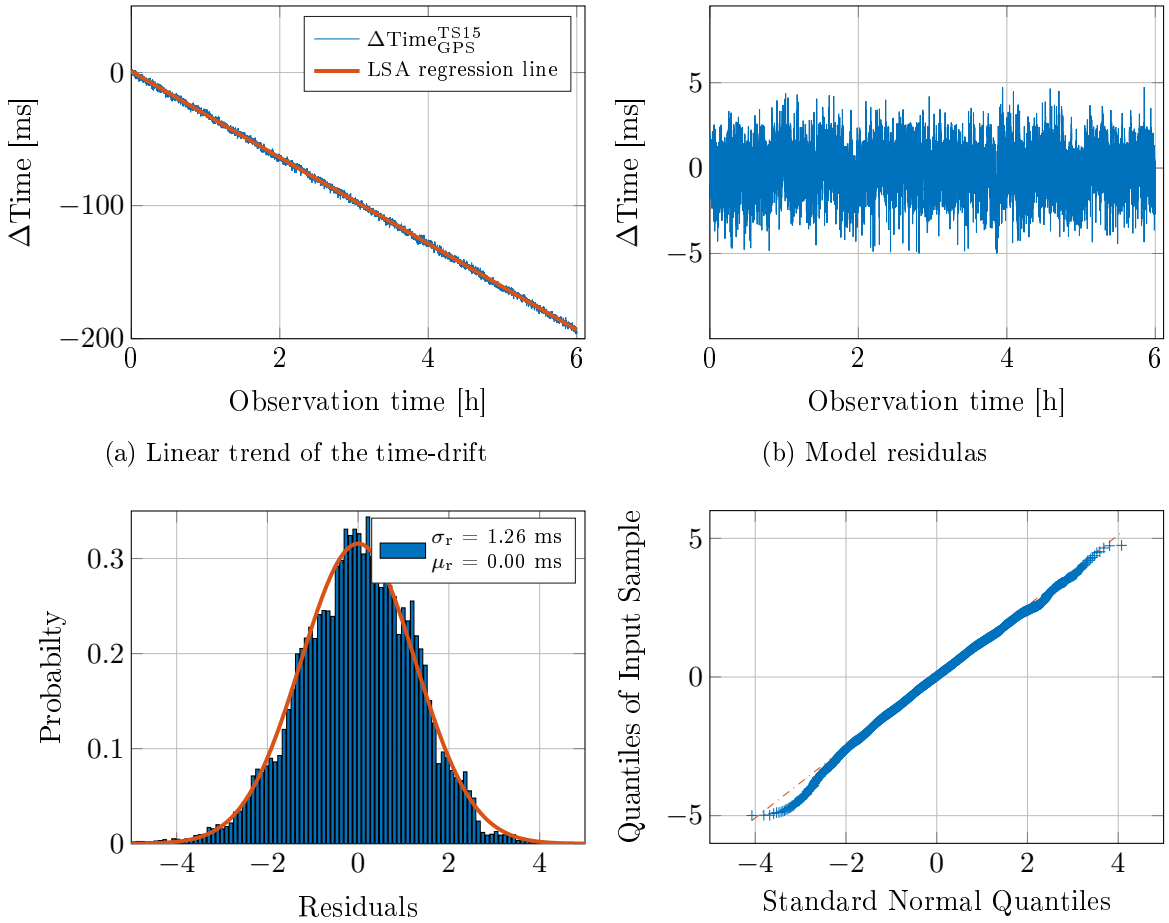

(a) Linear trend of the time-drift

(b) Model residulas

(c) Histogram of residuals

(d) QQ plot

Figure A.4: Results of the Leica TS15 climate chamber experiment at 40°C ambient temperature

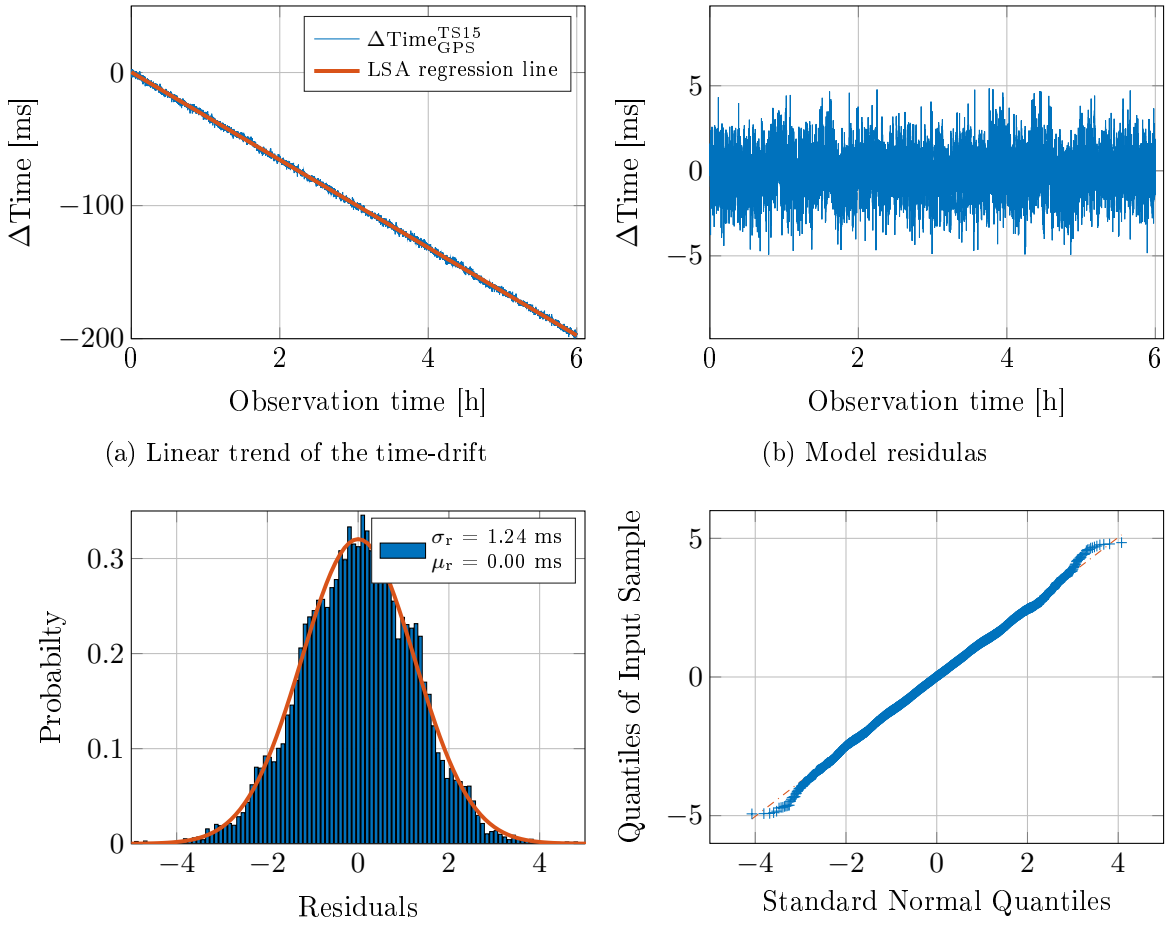

(a) Linear trend of the time-drift

(b) Model residulas

(c) Histogram of residuals

(d) QQ plot

Figure A.5: Results of the Leica TS15 climate chamber experiment at 50°C ambient temperature

A.2 Leica MS60

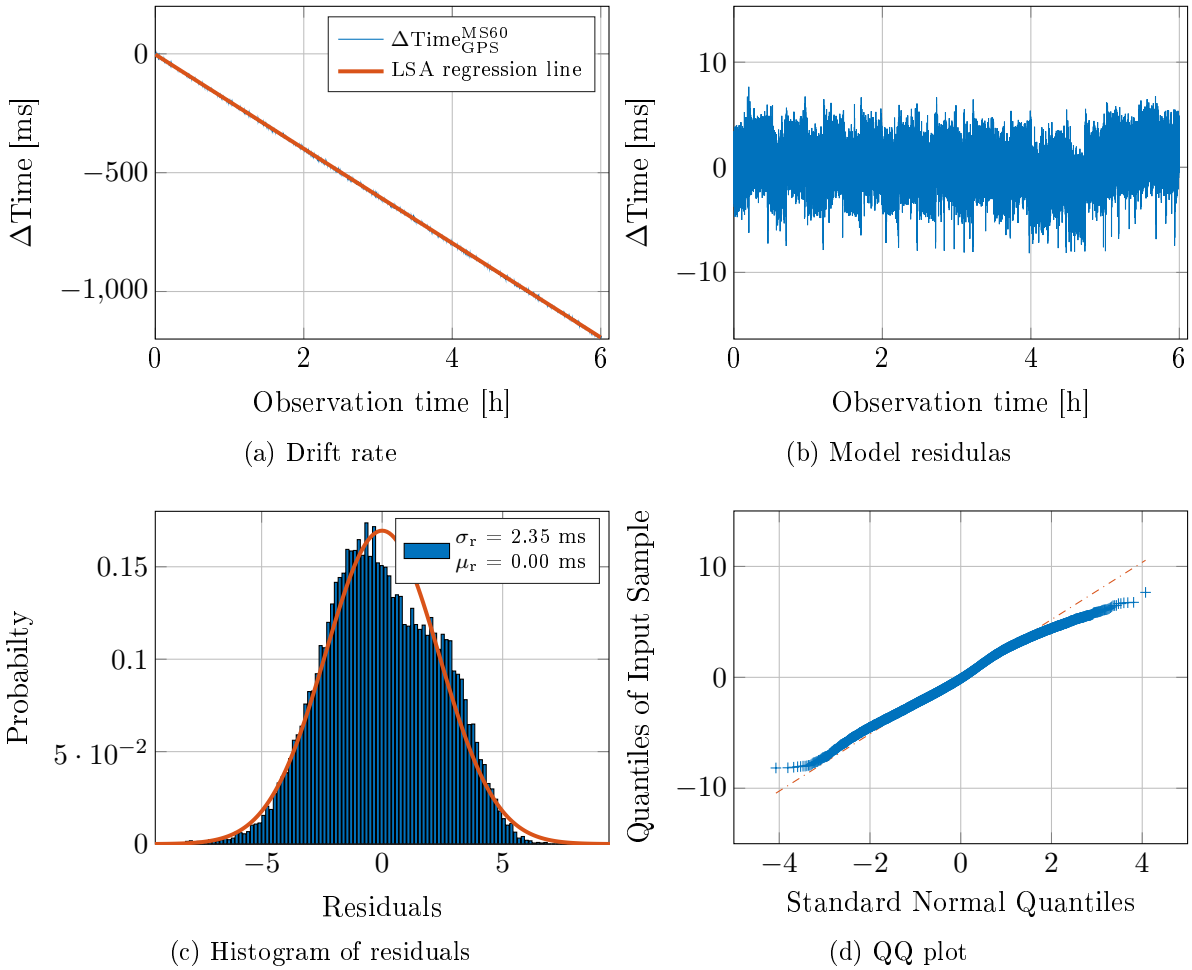

(a) Drift rate

(b) Model residulas

(c) Histogram of residuals

(d) QQ plot

Figure A.6: Results of the Leica MS60 climate chamber experiment at 10°C ambient temperature

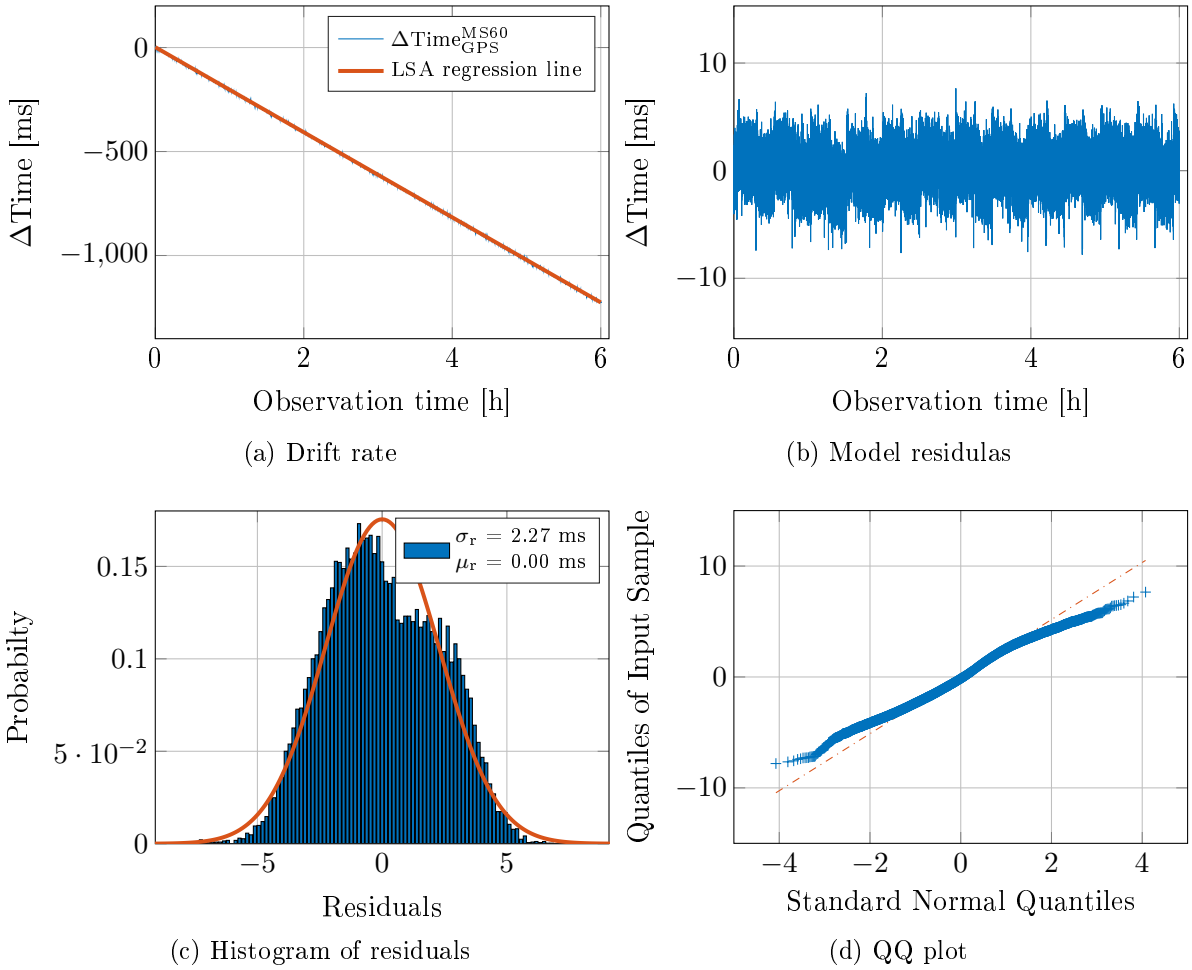

(a) Drift rate

(b) Model residulas

(c) Histogram of residuals

(d) QQ plot

Figure A.7: Results of the Leica MS60 climate chamber experiment at 20°C ambient temperature

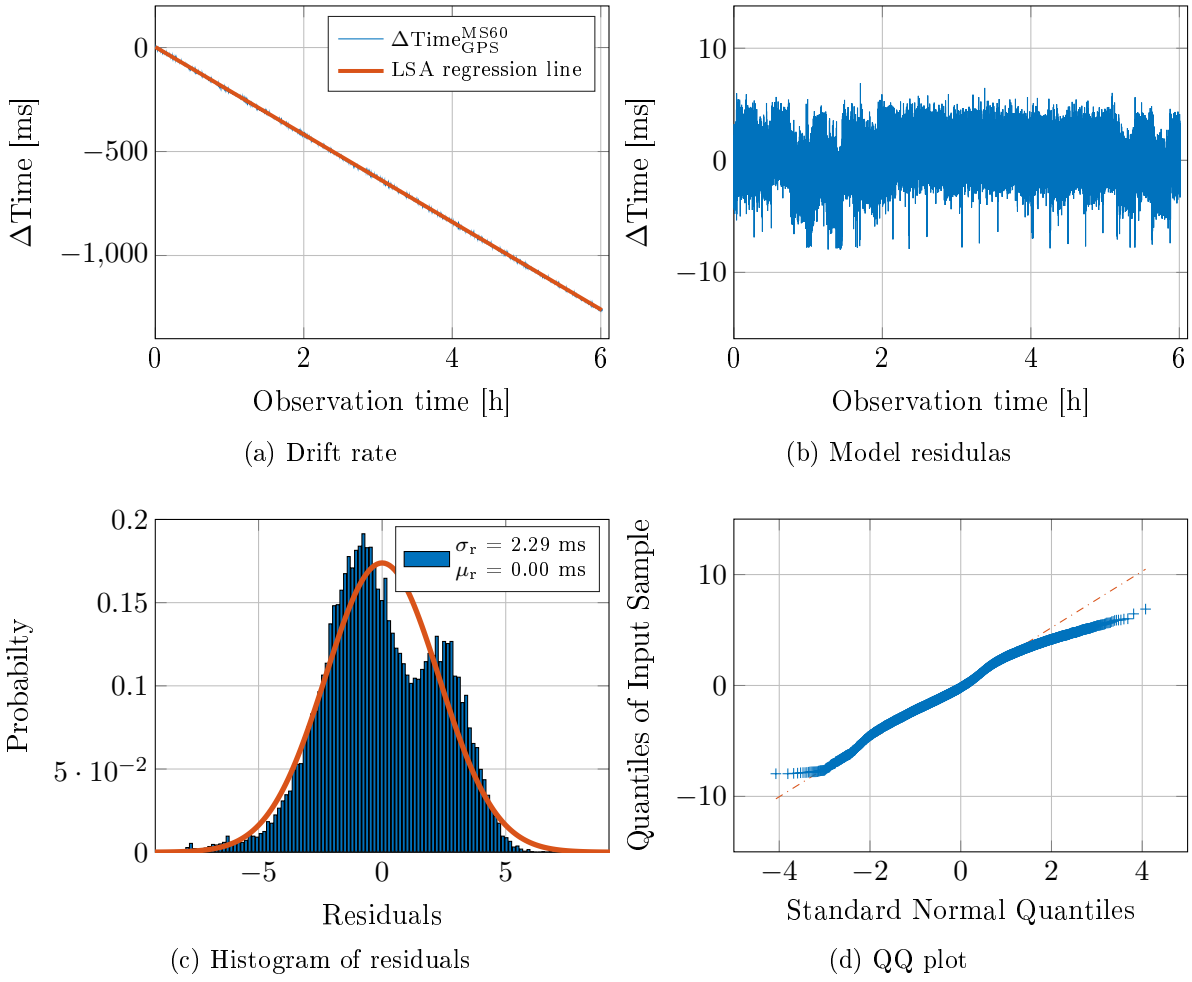

(a) Drift rate

(b) Model residulas

(c) Histogram of residuals

(d) QQ plot

Figure A.8: Results of the Leica MS60 climate chamber experiment at 30°C ambient temperature

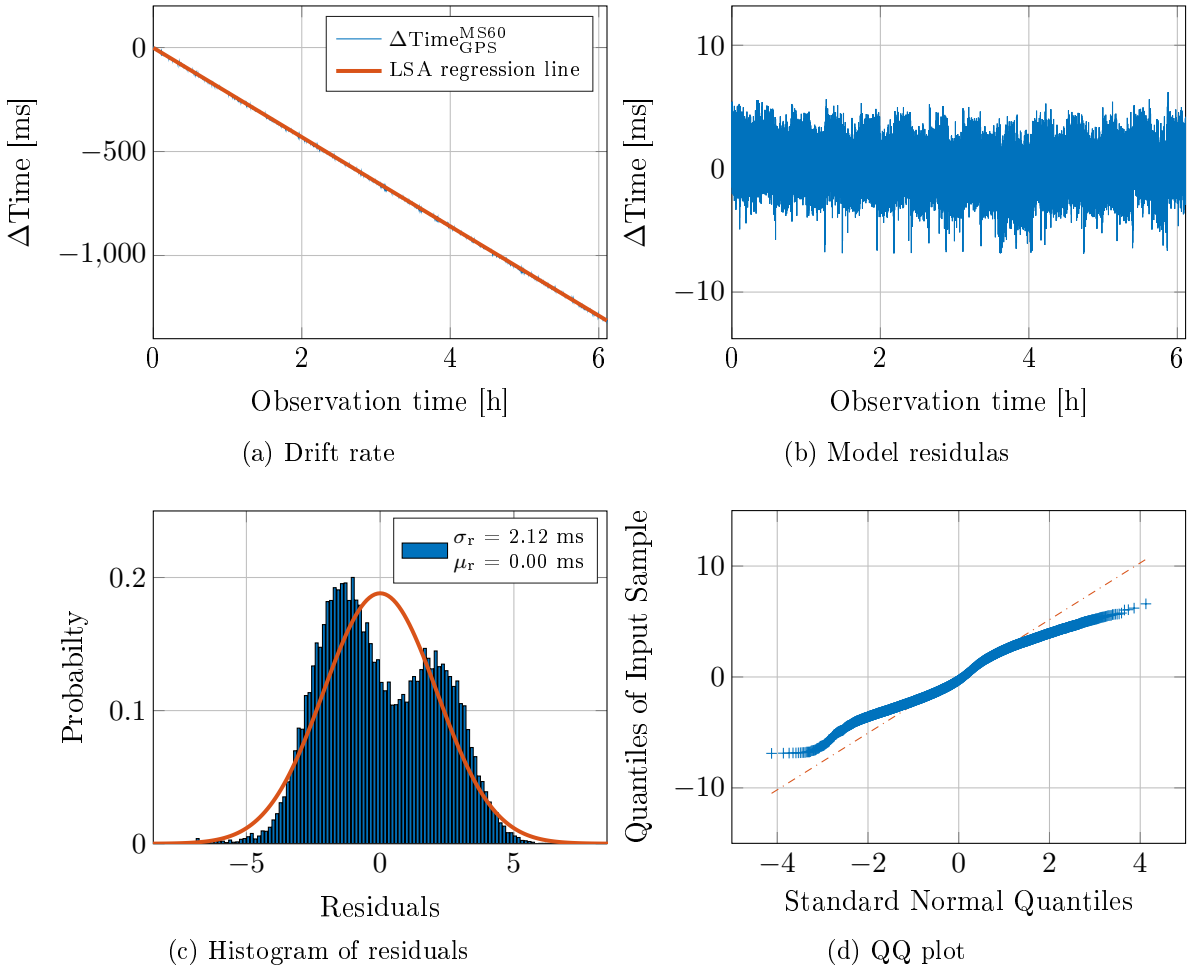

(a) Drift rate

(b) Model residulas

(c) Histogram of residuals

(d) QQ plot

Figure A.9: Results of the Leica MS60 climate chamber experiment at 40°C ambient temperature

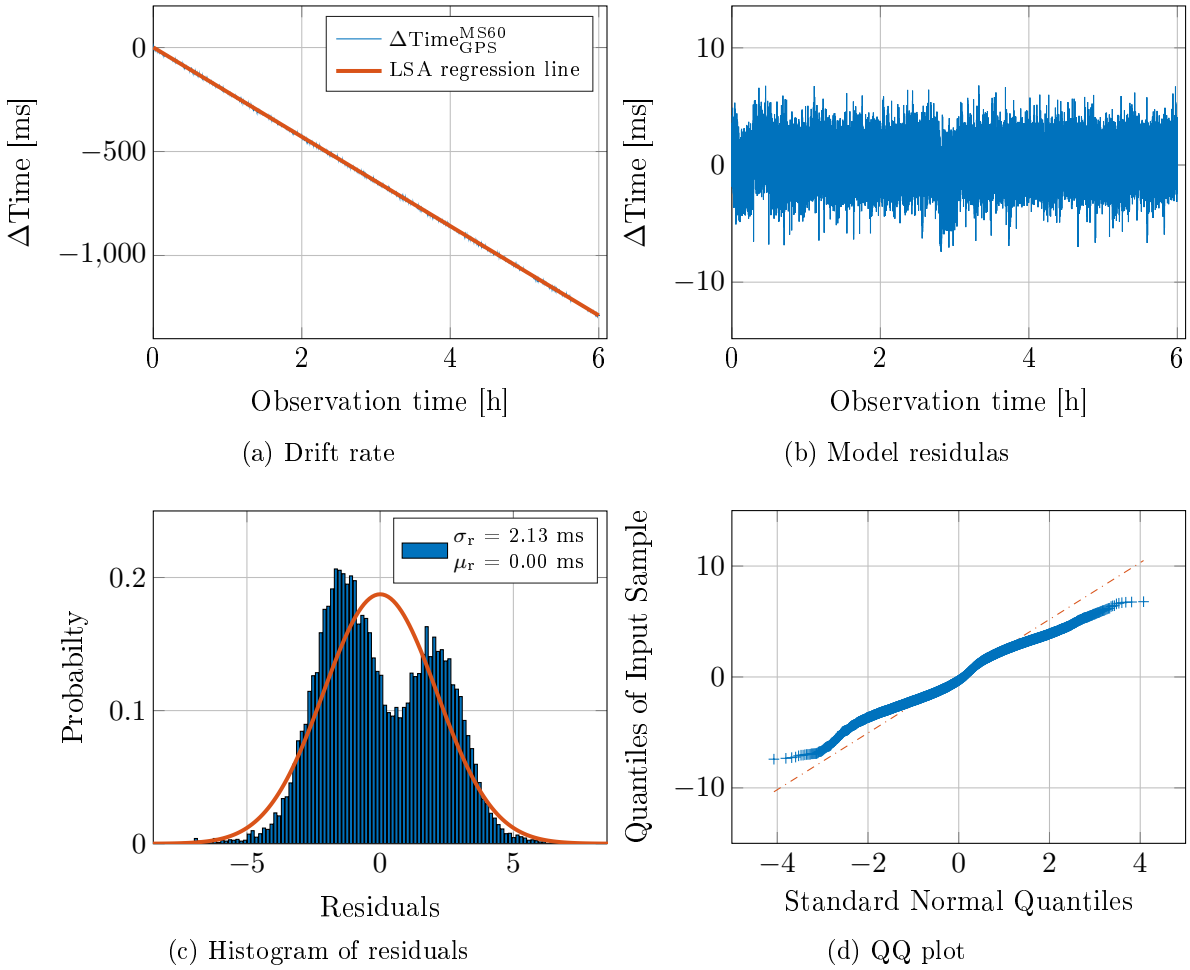

(a) Drift rate

(b) Model residulas

(c) Histogram of residuals

(d) QQ plot

Figure A.10: Results of the Leica MS60 climate chamber experiment at 50°C ambient temperature